ABSTRACT

Title of dissertation: PAIR CREATION AND PAIR ANNIHILATION IN BOSE-EINSTEIN CONDENSATES

Yi-Hsieh Wang, Doctor of Philosophy, 2017

Dissertation directed by: Professor Charles W. Clark
Department of Physics

This thesis covers three applications of Bose-Einstein condensates and related phenomena, with the theme of pair creation and pair annihilation.

First, Bose-Einstein condensates (BEC) are viewed as a candidate to implement a sonic black hole. This can lead to the observation of analog Hawking radiation, resulting from phonon pair creation at a black-hole horizon. Such implementation has been achieved in a resent experiment by J. Steinhauer, in which a black-hole/white-hole pair have been produced. He also reported the observation of self-amplifying Hawking radiation, via a lasing mechanism operating between the black and white hole horizons. Through simulations using the Gross-Pitaevskii equation, we find that the experimental observations should be attributed not to the black hole laser effect, but rather to a growing zero-frequency bow wave, generated at the white-hole horizon. The relative motion of the black-hole and white-hole horizons produces a Doppler shift of the bow wave at the black hole, where it stimulates the emission of monochromatic Hawking radiation. This mechanism is confirmed

using temporal and spatial windowed Fourier spectra of the condensate. We also find that shot-to-shot atom number variations, of the type normally realized in ultracold-atom experiments, and quantum fluctuations of condensates, computed in the Truncated Wigner approximation, give density-density correlations consistent with those reported in the experiments. In particular, atom number variations can produce a spurious correlation signal.

Secondly, a sonic black hole/white hole pair and phonon pair creation can also be realized using a ring-shaped condensate. Here we focus on the phonon spectroscopy of a ring-shaped condensate with the presence of a potential barrier. This is the configuration for an atomtronic superconducting interference device (SQUID). We probe the phonon excitation spectrum by applying a harmonically driven barrier to a ^{23}Na Bose-Einstein condensate in a ring-shaped trap. When excited resonantly, these wavepackets display a regular periodic structure. The resonant frequencies depend upon the particular configuration of the barrier, and are commensurate with the orbital frequency of a Bogoliubov sound wave traveling around the ring. Energy transfer to the condensate over many cycles of the periodic wavepacket motion causes enhanced atom loss from the trap at resonant frequencies. Solutions of the time-dependent Gross-Pitaevskii equation exhibit quantitative agreement with the experimental data.

Thirdly, positronium BECs are of experimental and theoretical interest due to their potential application as the gain medium of a gamma-ray laser. Ps BECs are intrinsically spinor due to the presence of ortho-positronium (o-Ps) and para-positronium (p-Ps), whose annihilation lifetimes differ by three orders of magnitude.

We study the spinor dynamics and annihilation processes in the p-Ps/o-Ps system using both solutions of the time-dependent Gross-Pitaevskii equations and a semi-classical rate-equation approach. The spinor interactions have an O(4) symmetry which is broken to SO(3) by an internal energy difference between o-Ps and p-Ps. For an initially unpolarized condensate, there is a threshold density of $\approx 10^{19}$ cm^{-3} at which spin mixing between o-Ps and p-Ps occurs. Beyond this threshold, there are unstable spatial modes accompanied by spin mixing. To ensure a high production yield above the critical density, a careful choice of external field must be made to avoid the spin mixing instability.

PAIR CREATION AND PAIR ANNIHILATION IN BOSE-EINSTEIN CONDENSATES

by

YI-HSIEH WANG

Dissertation submitted to the Faculty of the Graduate School of the
University of Maryland, College Park in partial fulfillment
of the requirements for the degree of
Doctor of Philosophy
2017

Advisory Committee:
Professor Theodore Jacobson, Chair
Professor Charles W. Clark
Professor Steve L. Rolston
Professor Gretchen K. Campbell
Professor Christopher Jarzynski, Dean's representative

Acknowledgments

First of all, I would like to thank my advisor, Dr. Charles Clark. Charles, thank you for introducing me to all the interesting ideas and projects, and thank you for your patience when I failed to be productive. Thank you for supporting me throughout the years.

Secondly, I would like to thank Professor Ted Jacobson. Thank you for spending so much time meeting with me, helping me solve the big and small problems in our project. I think I've learned a lot from you. Thank you very much.

I also like to thank all people that I collaborate with during the past few years. I'd like to thank Brandon Anderson for helping me with my first project of positronium BECs. I am also grateful for the people in the ring BEC lab, Dr. Gretchen Campbell, Dr. Steve Eckell, Dr. Fred Jendrzejewski, and Avinash Kumar. Thank you for being nice, helping me understand your experiment, and writing our paper. Thank you for the wonderful working experience. Also, I'd like to thank Dr. Ryan Wilson for the calculation of the BdG spectrum, and many useful discussions. Thank you Dr. Mark Edwards for showing me how to better simulate a condensate experiment.

I would like to thank the people in the chemical physics program. Thank you Dr. Michael Coplan and Dr. Chris Jarzynski for taking me to the program, guiding me academically, and being so kind to me. I truly appreciate it. And thank you, Mrs. Debbie Jenkins, for helping me with many things in the program. Thank you for showing me warmth and positivity. Lastly, thank you Dr. Garegin Papoian for

consulting me during my stage of confusion. Thank you all for your support in this program.

I am thankful for all my friends here in Maryland for the precious time you brought to me. I am grateful for my JQI friends and colleagues, Alejandra, Pablo, Carla, Xunnong, Yidan, Fangli, Chiao-Hsuan, Bin, Ranchu, Meng-Chang, Ruizhi, Zhexuan; and my other friends, Zhiyue, Huizhi, Hsiang-Ling, Yurong, Yang, Yong, Zhixin, Hao, Joel, Jonathan, Jim, and Clare. Thank you for your friendship with me.

I would like to thank my family, Mom and Dad, Song-En, Linen, and my best friend Meng-Shuan. Thank you for always being there for me, giving me a place where I can always turn to. Thank you.

Lastly, LORD, thank you for getting me this far. I could not be here without you. For that, I am truly thankful.

Table of Contents

List of Tables

List of Figures

List of Abbreviations

BEC	Bose-Einstein Condensate
GP	Gross-Pitaevskii
GPE	Gross-Pitaevskii Equation
BdG	Bogoliubov-de Gennes
BH	Black-hole Horizon
WH	White-hole Horizon
HR	Hawking Radiation
BCR	Bogoliubov-Čerenkov Radiation
TWA	Truncated-Wigner Approximation
SQUID	Superconducting Quantum Interference Device
rf	radio frequency

Chapter 1: Introduction

Bose Einstein condensation was first predicted by Einstein in 1925. He considered that a gas of non-interacting bosons at a given temperature would undergo a phase transition, characterized by a critical phase-space density, above which the excess density would consist of particles all occupying the lowest energy state [3]. At this critical density, the de Broglie wavelength of the gas becomes comparable to the mean distance between atoms, and particles behave like waves, overlapping with each other. In particular, concerning the macroscopic fraction of bosons in the lowest energy state, they behave collectively as a single matter wave. This is a Bose-Einstein condensate (BEC).

The first BEC was produced in 1995 in a laboratory using a dilute gas of ^{87}Rb, trapped and laser-cooled to the temperature on the order of 10^{-8} K [4]. Later in the same year, BEC was also attained in ultracold gases of ^{7}Li and ^{23}Na atoms [5, 6]. This was made possible by advances in atom trapping and cooling techniques [7]. The method of lasing cooling was developed in the 1980s to lower the temperature of a gas to the order of microkelvin [7]. Furthermore, a gas of trapped atoms can be further cooled down to the order of nanokelvins by releasing energetic "hot" atoms through the lowering of the trap depth. This is a technique called evaporative

cooling [8], which can cool a gas of alkali atoms below the critical temperature (on the order of tens of nanokelvin), and lead to the formation of a BEC.

A trapped BEC has a finite size, determined by the scale of its trapping potential, the number of atoms, and repulsive interaction between atoms. It can contain atoms in the range of $N = 10^3 - 10^7$, and the length of a condensate can be up to the order of millimeters [9], which is considered "macroscopic", compared to objects in the atomic scale. Regarding the macroscopic and coherence properties of a BEC, quantum phenomena, expected in the single atom regime, can be enhanced and observed in laboratories. For instance, two expanding BEC clouds can overlap, and result in an interference pattern measurable in the lab [9]. This creates opportunities to investigate the quantum nature of matter, and furthermore, to control and engineer quantum many-body systems [10].

On the theory side, using the mean field approximation for weakly interacting Bose gases, a BEC can be described by a macroscopic wavefunction, satisfying a nonlinear different equation called Gross-Pitaevskii (GP) equation [11, 12]. The GP equation has been proved successful in predicting many behaviors of BECs observed in experiments, such as stationary configuration, interference, formation of vortices, etc. Beyond the GPE, excitations can be treated by the Bogoliubov approximation [13]. In this approximation, the excitations are viewed as quasiparticle operators, whose amplitudes satisfy the Bogoliubov-de Gennes (BdG) equations. With the BdG theory, one can estimate quantum depletion in a BEC, and predict properties for the noncondensate fraction, like excitation spectrum, speed of sound, etc.

1.1 In this thesis

In this thesis, with the GPE and BdG equations as the basic theoretical tools, we investigate three different applications of BECs and related phenomena, in the theme of the creation and annihilation of a particle-antiparticle pair.

1.1.1 Analog black hole and Hawking radiation in BECs

The first application focuses on the ideas of analog black hole and Hawking radiation in BECs. Quasiparticle pair creation can occur at the event horizon of an analog black hole formed in a BEC, emitting analog Hawking radiation and its partner [14, 15]. In the context of analog systems, a phonon propagating in a hydrodynamic flow is analogous to a light trajectory in a curved spacetime, where the speed of sound plays the role as the speed of light [16]. In BECs, low energy excitations behave as phonons, propagating at the speed of sound on a condensate flow. Critical behaviors of phonons occur at a point where the flow velocity transitions from subsonic to supersonic. This critical point is the black-hole event horizon (BH), at which the flow speed is equal to the speed of sound. Behind the horizon is an analog black hole, where no phonon can escape from the supersonic flow to the upstream region. One exception is the pair creation occurring at the horizon, emitting a phonon to the upstream, and its partner to the downstream. The phonon escaping from the black hole is viewed as the analog Hawking radiation (HR).

In recent years, a series of groundbreaking experiments have been performed at Technion [1, 17, 18]. A sonic black-hole horizon was created in an elongated

BEC using a "waterfall-like" potential [17]. Later, using a similar experimental procedure [1], the observation of self-amplifying Hawking radiation was reported. The latest achievement is the correlated signal of spontaneous pair creation from a black-hole horizon [18].

In the first part of this thesis (Chapters 3 and 4), we study the experiment in [1]. In this experiment, the BEC contains a supersonic cavity, a region of supersonic flow bounded by a black-hole and a white-hole horizon (where the supersonic flow transitions back to subsonic). Treating this supersonic region as a lasing cavity, it was suggested in [1] that HR and its partner are created from the vacuum state at the black-hole horizon, and then self-amplify through a "black-hole laser" [19]. Observation of a growing standing wave inside the cavity was associated with the HR partner mode, and was treated as evidence of self-amplification of HR. With thorough analysis and simulations, we find a standing wave pattern similar to that in the experiment, and a signal of Hawking radiation, but attribute the observations to a mechanism different from the lasing interpretation. We find that the standing wave is due to an instability at the white-hole horizon, which grows with the increasing background density. As the standing wave reaches the black-hole horizon, it stimulates the pair creation.

In Chapter 3, we present our simulated results and the mechanism of stimulated Hawking effect. The experimental procedure is simulated using the GP equation, followed by a spectral analysis of the excitation modes. We also identify different regimes of experimental parameters, from which a sharper signal of Hawking radiation can be obtained. Chapter 4 takes into account quantum fluctuation, with

a method using Truncated-Wigner approximation (TWA) [20]. This allows us to calculate the density-density correlation function reported in [1]. We also consider the shot-to-shot variation in the condensate atom number. With the presence of both types of fluctuations, we reproduce a checkerboard pattern in the simulated correlation, similar to the experimental observation. This pattern has the same origin as the standing wave, which is brought to the correlation through the variation of atom number, and the long-wavelength components in the quantum fluctuation.

1.1.2 Ring-shaped BECs and phonon wavepackets

The second application focuses on a ring-shaped condensate and the behavior of phonon wavepackets. A toroidal-shaped BEC has been realized in a laboratory using a gas of ^{23}Na, confined in a optical dipole trap [21, 22]. It is used in the laboratory to develop the atom analog of a superconducting quantum interference device (SQUID). Applying a repulsive potential barrier on the BEC can create a constricted, low-density region, which can be viewed as a weak link. By rotating the weak link at various rates, quantized circulations have been observed, associated with a drastic phase change in the weak link region. This generates a current-phase relation analogous to that of Josephson-like Junction in a superconducting SQUID [22].

Another potential application for a ring BEC is to implement an analog black-hole. A ring-shaped configuration with a pair of black-hole and white-hole horizons has been considered theoretically for the observation of Hawking phenomenon [15,

23, 24]. With a prepared persistent current in the ring, the two horizons can be created with constrictions, such as a weak link of the SQUID, upon which the flow velocity may change. The flow velocity can be modulated to create a region of supersonic flow, bounded by two horizons, similar to that of black-hole laser. Under such configuration, instability of certain phonon modes was predicted. This is associated with the amplification of black-hole radiation [23, 24].

In Chapter 5, we study the phonon excitations on a ring-shaped condensate, in collaboration with experimentalists. We apply a potential barrier, modulating the position and amplitude sinusoidally to create phonon wavepackets with various frequencies. At resonant frequencies, the wavepackets display distinct periodic structures, depending on the modulating schemes. We study the behaviors of the phonon wavepackets using the GP equation, and find a good agreement with the experimental results. This study exhibits the spectrum of phonon excitations of a ring-shaped condensate. It can be useful for the investigation of phonon pair creation with a sonic horizon created in the ring condensate.

1.1.3 Positronium BECs, self-annihilation, and γ-ray laser

The last topic focuses on a condensate made of positronium atoms. Positronium (Ps) is the simplest atom composed of a particle and its anti-particle, an electron and a positron. Both electron and position are spin-1/2 fermions, so a Ps atom in the electronic ground state can have total spin $S = 0, 1$. Regarding the matter-antimatter constituents, a Ps atom has the tendency to self-annihilate and

decay into γ-rays. For a spin-0 Ps (para-positronium or p-Ps), the lifetime is ~ 0.1 ns, and a spin-1 Ps (ortho-positronium or o-Ps) has a longer lifetime, which is about ~ 0.1 μs [25].

In 1994, Platzman and Mills proposed a scheme of making a condensate of o-Ps atoms, by impinging a positron pulse on a cavity made of silicon materials [26]. When a positron passes through the silicon wall, it can capture an electron from the material and turn into a positronium, trapped inside the cavity. After collecting enough Ps atoms, and cooling the cavity below the critical temperature ($T_c = 15$ K for Ps density $n = 10^{18}$ cm^{-3}), a Ps condensate can form [27]. Recent experiments in Ps research have achieved a gas of spin-polarized Ps atoms with density about two orders of magnitude smaller than the condensation requirement [28], which makes the formation of Ps BECs more likely in future laboratories [28–30].

One important aspect of Ps condensates is the implementation of a γ-ray laser [27, 31]. A Ps condensate can be viewed as a source which can coherently self-annihilate, and generate a beam of high-coherence γ-rays. This can be achieved by applying a rf pulse to convert a o-Ps condensate to the short-lived p-Ps [31]. Once a γ photon is created from a self-annihilating p-Ps, it would further stimulate the annihilation process of other p-Ps atoms in the condensate, generating coherent γ rays. This can be viewed as the lasing action of a γ-ray laser.

In Chapter 6, we derive a theoretical formalism for a spinor condensate of positronium, as a coherent mixture of o-Ps and p-Ps. We find a critical density, beyond which spin-mixing can occur through inelastic collision between atoms and destroy the coherence of the condensate. We also propose two schemes of applying

the rf pulse to convert o-Ps to p-Ps, such that the coherence of the system would be preserved during the annihilation/lasing process.

1.1.4 Overview

The structure of this thesis is as follows.

Chapter 2 introduces the background theoretical tool, a basic formalism in the mean-field theory, describing a Bose-Einstein condensate and its elementary excitations.

Chapters 3 and 4 are based on the work done with Ted Jacobson, Mark Edwards, and Charles Clark. In the two chapters, we study an analog black hole and its Hawking radiation in a laboratory condensate. Chapter 3 focuses on the simulation using the 1D GPE, followed by a spectral analysis using windowed Fourier transforms. Chapter 4 takes into effects of quantum fluctuation and atom number variation to reproduce an important checkerboard pattern observed in the experimental density-density correlation function.

Chapter 5 is a project in collaboration with Ryan Wilson, Mark Edwards, Charles Clark, and the ring-BEC laboratory led by Dr. Gretchen Campbell. We present a study of a ring-shaped condensate and its phonon spectroscopy.

In Chapter 6, we develop a theoretical model for a spinor condensate of positronium, which gives rise of a condition to the occurrence of spin-mixing. Based on this condition, we propose a scheme to suppress the spin mixing, and maintain the condensate coherence for the implementation of a γ-ray laser. This work was done

with Brandon Anderson and Charles Clark.

Appendix A gives the detailed simulation procedures for Chapter 3. It also introduces the details of the windowed Fourier Transform used in the same chapter. Appendix B introduces the numerical procedures for Chapter 4.

Related research papers in this thesis:

- Chapter 3

Mechanism of stimulated Hawking radiation in a laboratory Bose-Einstein condensate, Yi-Hsieh Wang, Ted Jacobson, Mark Edwards, and Charles W. Clark, arXiv: 1605.01027 (2016).

- Chapter 4

Atom number variations and density correlations in sonic black hole condensates, Yi-Hsieh Wang, Ted Jacobson, Mark Edwards, and Charles W. Clark (to be submitted).

- Chapter 5

Resonant wavepackets and shock waves in an atomtronic SQUID, Yi-Hsieh Wang, A. Kumar, F. Jendrzejewski, Ryan M. Wilson, Mark Edwards, S. Eckel, G. K. Campbell, and Charles W. Clark, New J. Phys. **17**, 125012 (2015).

- Chapter 6

Spinor Bose-Einstein condensates of positronium, Yi-Hsieh Wang, Brandon M. Anderson, and Charles W. Clark, Phys. Rev. A **89**, 043624 (2014).

Chapter 2: Theoretical methods for BECs and elementary excitations

In this thesis, we are interested in the several phenomena associated with both the condensates mode and the elementary excitations. The behaviors of a condensate can be modeled by the Gross-Pitaevskii theory, and the excitations can be analyzed by Bogoliubov-de Gennes theory. Here we introduce these basic theoretical tools which are used extensively in the thesis.

In a many-body system, where a single-particle state is macroscopically occupied, the field operator of the system, $\hat{\Psi}$, can be expressed as a mean field of the single-particle state plus a quantum field of fluctuations. That is,

$$\hat{\Psi} = \Psi_0 + \delta\hat{\Psi} \tag{2.1}$$

where Ψ_0 denotes the mean field, i.e. the wavefunction of the BEC, and $\delta\hat{\Psi}$ is the field operator of the quantum fluctuations. The equation of motion for the condensate wavefunction is the time-dependent Gross-Pitaevskii equation (TDGPE),

$$i\hbar\frac{\partial}{\partial t}\Psi_0(\mathbf{r},t) = \left[-\frac{\hbar^2}{2M}\nabla^2 + V(\mathbf{r}) + g\left|\Psi_0(\mathbf{r})\right|^2\right]\Psi_0(\mathbf{r}). \tag{2.2}$$

where V is the external potential, and g is a coefficient describing the mean-field interaction between atoms, and M is the atomic mass. The interaction coefficient

is given by $g = 4\pi\hbar^2 a/m$, where a is the scattering length associated with binary atomic collisions. The stationary solution of the GP equation can be expressed as

$$\Psi_0(\mathbf{r}, t) = \sqrt{n(\mathbf{r})} e^{-i\mu t/\hbar} \tag{2.3}$$

where $n(\mathbf{r})$ is the condensate density, and μ the chemical potential.

The elementary excitations of the system can be viewed as the deviation from the mean field, and can be described by the operator $\delta\hat{\Psi}$, which satisfies the equation of motion

$$i\hbar\frac{\partial}{\partial t}\delta\hat{\Psi}(\mathbf{r}, t) = \left[-\frac{\hbar^2}{2m}\nabla^2 + V(\mathbf{r}) + 2gn(\mathbf{r}) - \mu\right]\delta\hat{\Psi}(\mathbf{r}, t) + g\Psi_0^2\delta\hat{\Psi}^\dagger \tag{2.4}$$

We treat $\delta\hat{\Psi}$ to first order in atomic number fluctuations,

$$\delta\hat{\Psi} = \sum_i \left(u_i e^{-i\omega_i t} a_i + v_i^* e^{i\omega_i t} a_i^\dagger\right), \tag{2.5}$$

to obtain the Bogoliubov-de Gennes (BdG) equations:

$$\begin{aligned}\left[\hbar\omega_i + \frac{\hbar^2}{2M}\nabla^2 - V(\mathbf{r}) - 2gn(\mathbf{r}) + \mu\right] u_i(\mathbf{r}) &= gn(\mathbf{r})v_i(\mathbf{r}) \\ \left[-\hbar\omega_i + \frac{\hbar^2}{2M}\nabla^2 - V(\mathbf{r}) - 2gn(\mathbf{r}) + \mu\right] v_i(\mathbf{r}) &= gn(\mathbf{r})u_i(\mathbf{r}).\end{aligned} \tag{2.6}$$

If the system is homogeneous in space ($V(\mathbf{r}) = 0$), we have the plane-wave solution for Eq. 2.6 [32], $u_\mathbf{k}(\mathbf{r}) = u_\mathbf{k} e^{i\mathbf{k}\cdot\mathbf{r}}$ and $v_\mathbf{k}(\mathbf{r}) = v_\mathbf{k} e^{i\mathbf{k}\cdot\mathbf{r}}$, where $\mathbf{k} = k\hat{k}$ denotes the wave vector. This leads to the dispersion relation

$$\omega(k) = \pm\sqrt{\xi_k^2 - (gn)^2}. \tag{2.7}$$

where $\xi_k = \hbar^2 k^2/2M + gn$. For small k, the frequency $\omega(k)$ is linear in k, i.e. $\omega_k \sim \pm(\sqrt{gn/M})k$. Since this dispersion relation is the same as that for a sound

wave, $\omega = ck$, the quasiparticles in this regime can be viewed as phonons, and the proportionality constant determines the speed of sound, $c = \sqrt{gn/M}$.

The Bogoliubov theory of excitations is extensively used in this thesis. In Chapter 3, we use the BdG theory to identify the modes created at the sonic horizons and determine the associated mechanism. We observe a zero-frequency BdG mode created at the white hole horizon, which later reaches the black-hole horizon to stimulate a Hawking mode and its partner. The frequencies and the wavevectors of the observed modes are consistent with the prediction from the BdG dispersion relations and our proposed mechanism. In Chapter 4, we use the Truncated Wigner method, incorporating the Bogoliubov modes of excitations, to simulate quantum fluctuations in the condensate. This allows us to evaluate the density-density correlation for regions inside/outside the analog black hole. In Chapter 5, we numerically solve the BdG spectrum of a 3D ring-shaped condensate, and use it to identify the speed of sound for the phonon wavepackets generated in the ring system. In Chapter 6, we examine the dynamical instability of a spinor condensate by analyzing the complex frequency modes from the BdG equations. The details of these applications are given in each chapter.

Chapter 3: Analog black hole and Hawking radiation in a laboratory Bose-Einstein condensates

In this chapter, we study the effects of an analog black hole and Hawking radiation in a laboratory condensate [1]. As introduced in Chapter 1, elementary excitations in a BEC are quasiparticles that satisfy the Bogoliubov-de Gennes (BdG) equations, with low energy eigenmodes that behave like phonons, propagating with the speed of sound. This black hole analogy holds for a BEC since the BdG equations can be expressed in the form of the relativistic wave equation, and the behavior of quasiparticles in the condensate flow can be viewed as an analog of light traveling in the flow of curved spacetime [15, 33].

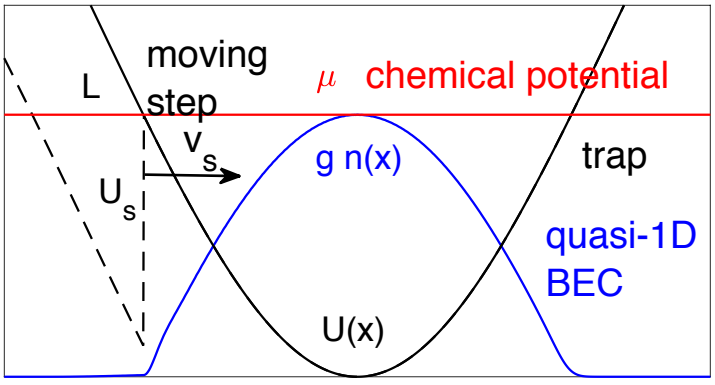

Figure 3.1: Potential-step structure at the start of its sweep through the BEC with number density $n(x)$, chemical potential μ and confining potential $U(x)$.

Recently, a black-hole/white-hole pair has been achieved experimentally by J. Steinhauer, using an elongated, quasi-1D condensate of ^{87}Rb [1]. In this experiment, the BEC is swept by a negative step potential of depth U_s at uniform speed v_s, as illustrated in Fig. 3.1 (U_s is on the order of 10^{-9} K, and v_s is 0.21 mm/s). Atoms are accelerated in the direction opposite to the step motion due to the precipitous drop in the potential. This creates a left-moving, supersonic flow behind the step, and a black-hole horizon (BH) is formed at the step edge, $x_{\rm BH}$. The accelerated atoms gradually slow as they recede from the step, due to the rising potential. This causes the flow to become subsonic at a critical distance L behind the step, forming a white-hole horizon (WH), $x_{\rm WH}$. The flow structure is shown in Fig. 3.5(b), where a BH and a WH enclose a region of supersonic flow, which can be viewed as a supersonic cavity. The velocity profile of the background flow is denoted by $-v(x)$; the profile of the speed of sound is denoted by $c(x)$. With a flow moving to the left, the BH is formed at the point where $-v(x) = c(x)$, when the flow goes from subsonic to supersonic. Similarly, the WH is the point that also satisfies $-v(x) = c(x)$, but the flow transitions from supersonic to subsonic.

Figure 3.2(a) shows an experimental density profile at a time after the sweep. A low-density region can be seen in the interior of the BEC, and identified as a supersonic cavity, bounded by BH and WH horizons. At later times, there is a standing wave developed inside the cavity, as shown Fig. 3.2(b). The growth of the standing wave amplitude is measured through a density-density correlation function, $G^{(2)}(x, x')$, shown in Fig. 3.2(c). This $G^{(2)}$ function displays correlations between points within the cavity, as well as between a point in the cavity and a point outside

the BH. Specifically, in the cavity region ($-25 < x < 0$), a checkerboard pattern can be seen, and associated with the standing wave pattern.

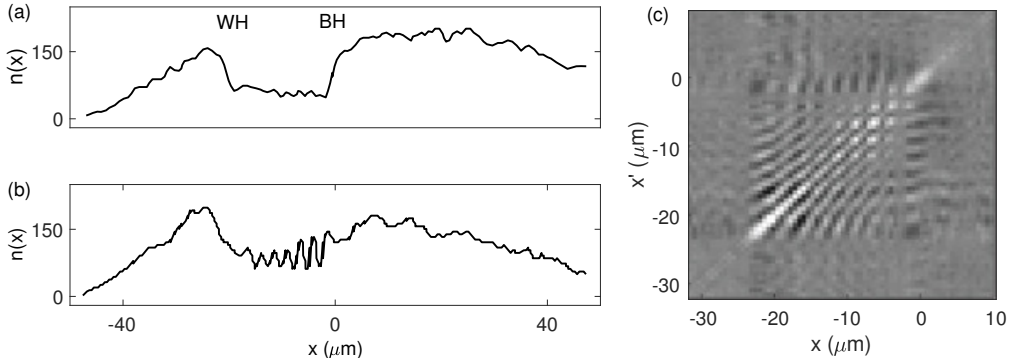

Figure 3.2: Experimental observations taken from [1]. Panel (a) density profile of an elongated condensate at the early stage of the sweep; the region of low density corresponds to a supersonic cavity, bounded by a BH on the right and a WH on the left. Note that the origin is shifted to match the position of the step. Panel (b) density profile at later time, with a standing wave inside the cavity. Panel (c) density-density correlation function, $G^{(2)}(x, x')$.

In this chapter, we will focus on the simulation and the mechanism of the standing wave pattern, using the Gross-Pitaevskii (GP) equation and windowed Fourier transforms (WFTs). The correlation function will be discussed in the next chapter, where we incorporate the effects of quantum fluctuations and atom-number variation in our simulations. This work was done in collaboration with Ted Jacobson, Mark Edwards and Charles Clark, which can be found in [34].

In the original paper [1], the growing standing wave in Fig. 3.2 was interpreted as resulting from a self-amplifying Hawking radiation from a 'black-hole laser', a theoretical construct proposed by Jacobson and Corley in 1999 [19]. This black-hole laser is based on the presence of a supersonic 'lasing' cavity, bounded by a BH and a WH, which is similar to the flow structure shown in Fig. 3.5(b). The laser generates a self-amplifying HR, and makes the detection of the HR signal possible

in the analog-black-hole systems.

The scheme of a black-hole laser is illustrated in Fig. 3.3(a). Four BdG modes are present in the laser: a Hawking radiation (HR, labelled by $\psi_{\rm HR}$), HR partner (p-mode, $\psi_{\rm p}$) are generated at the BH; two opposite-energy modes ($\psi_{\pm}$) are generated at the WH. When the opposite-energy modes ($\psi_{\pm}$) impinge the BH from the cavity, a positive-energy HR ($\psi_{\rm HR}$) is emitted to the exterior, with its negative-energy partner ($\psi_{\rm p}$) back to the cavity. The p-mode then propagates to the left, impinges the WH, and bounces back in the form of opposite-energy modes ($\psi_{\pm}$). They travel back to the BH to emit a second HR, leaving more negative energy inside the cavity, with the p-mode amplified. The repetition of this process leads to exponential growth of the negative energy mode and the associated Hawking emission. This is called the black hole laser mechanism [14,19]. In Ref. [1], J. Steinhauer reported an exponential growth of the oscillatory density pattern in the BH-WH cavity. He suggested that the growth is resulting from from the black-hole-laser effect, and interpreted the standing wave as the interference of the counter-propagating modes ($\psi_{\rm p}$ and $\psi_{\pm}$) in the cavity.

Our simulation exhibits a similar growth of the standing wave, but leads to a different mechanism, as illustrated in 3.3(b). We find that the standing wave in the cavity emerges upon the formation of the WH, with its wavefront parallel to the WH, and is a form of instability at the WH [35]. This wave can also be identified as the Bogoliubov–Čerenkov radiation (BCR) [36], similar to a ship's bow wave on water. We examine the growth of the standing wave, and find that it is due to the increasing density towards the center of the atom trap during the

sweep. Its amplitude satisfies a specific growth relation with the background density, consistent with the BCR mechanism. In addition, regarding the inhomogeneity of the condensate, the cavity size L increases slightly as it approaches the center center, giving rise to a receding WH as indicated in 3.3(b). We find that this receding WH causes a Doppler shift on the standing wave frequency as it reaches the BH. At the shifted frequency, the BCR mode stimulates a pair creation of HR and p-mode. We argue that the black-hole lasing effect would be suppressed by the WH recession. Overall, the black hole laser mechanism plays no role in our simulation.

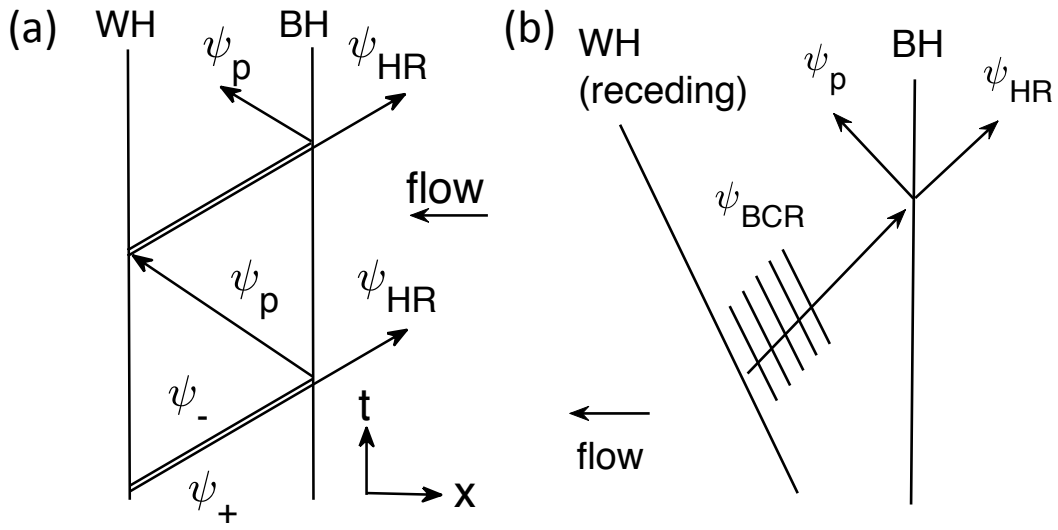

Figure 3.3: Black-hole-laser mechanism vs. BCR-stimulated Hawking radiation (HR). Panel (a): scattering scheme of quasiparticle modes in a black-hole laser. At the BH, $\psi_\pm$ modes scatter into a positive-energy HR and its negative-energy partner (p-mode) under energy conservation. The p-mode propagates to the WH, at which it is reflected back into the $\psi_\pm$ modes. Panel (b): mechanism of stimulated HR pair by a BCR mode ($\psi_{\rm BCR}$) generated at the WH as a standing wave.

3.1 Simple model of Bogoliubov modes at sonic horizons

The wavefunction in the GP equation, $\Psi(x,t)$, can be factored into a condensate component and a deviation in the form of linearized modes, representing quasiparticle excitations:

$$\Psi(x,t) = \Psi_{\rm bf}(x,t) + \sum_j \psi_j(x,t), \tag{3.1}$$

where $\Psi_{\rm bf}$ indicates the background confensate component, and ψ_j is an excited mode which satisfies the Bogoliubov-de Gennes (BdG) equation [32]. As indicated in Fig. 3.3(b), There are three modes observed in our simulation: the BCR mode, the HR mode, and the HR partner (labeled by j = BCR, HR, and p, respectively). In the following, we will explain the role of each mode in the presence of a sonic horizon, based on the BdG theory of linearized modes [32]. Here we introduce the BdG theory of linearized modes, and consider two scenarios, as shown in Fig. 3.4(a-b), regarding certain excited modes in the presence of sonic horizons, which are crucial in the system we investigate.

For a homogeneous flow of constant density $n_{\rm bf}$, the background component can be described by $\Psi_{\rm bf}(x,t) = \sqrt{n_{\rm bf}} e^{-i\omega_{\rm bf}t + ik_{\rm bf}x}$, where $\omega_{\rm bf}$ and $k_{\rm bf}$ represent the frequency and wavevector of the flow. This component determines the flow velocity, $v_{\rm bf} = \hbar k_{\rm bf}/m$, and the speed of sound, $c = \sqrt{g n_{\rm bf}/m}$, where m is the atomic mass and g is the mean-field interaction coefficient. And it gives rise to an excitation mode ψ_j which takes the form

$$\psi_j = \left(u_j e^{-i\Delta\omega_j t + i\Delta k_j x} + v_j^* e^{+i\Delta\omega_j t - i\Delta k_j x}\right) e^{-i\omega_{\rm bf}t + ik_{\rm bf}x}. \tag{3.2}$$

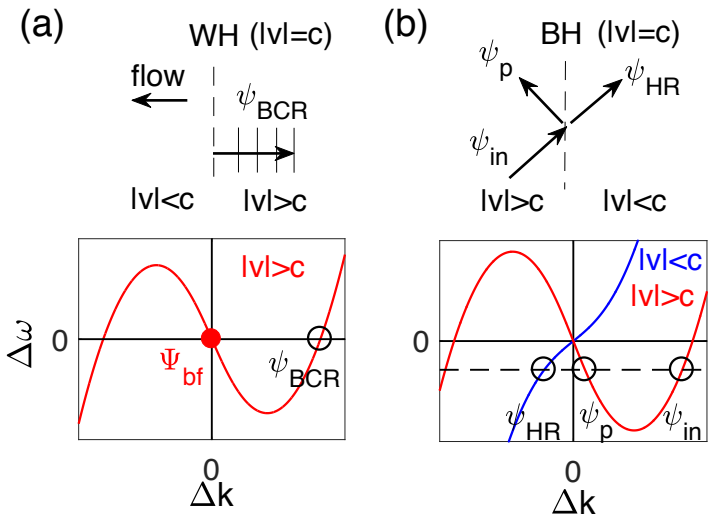

Figure 3.4: Bogoliubov modes at sonic horizons. (a) Illustration of BCR ($\psi_{\rm BCR}$) at the WH and its dispersion; (b) creation of HR ($\psi_{\rm HR}$) and its partner ($\psi_{\rm p}$) by an incoming mode ($\psi_{\rm in}$) at the BH.

Each BdG mode is composed of two components (u_j, v_j), with opposite frequency and wavevector, $\pm(\Delta\omega_j, \Delta k_j)$, relative to those of the background flow, $(\omega_{\rm bf}, k_{\rm bf})$. Solving the BdG equation determines the dispersion relation

$$\Delta\omega \;=\; \sqrt{(\hbar\Delta k^2/2m)^2 + c^2\Delta k^2} + v\Delta k, \tag{3.3}$$

where v is the velocity of the condensate with respect to the "observer" frame in which the frequency is defined; in the lab frame where Eq. 3.2 is defined, $v = v_{\rm bf}$. The square root term gives the frequency in the rest(comoving) frame of the condensate, $\Delta\omega_{\rm cm}$. And the amplitudes of two components of ψ_j are

$$(u_j, v_j) = \frac{1}{2\pi}\sqrt{\left|\frac{d\Delta k}{d\Delta\omega}\right|}\left(\frac{1}{\sqrt{1-D^2}}, \frac{D}{\sqrt{1-D^2}}\right), \tag{3.4}$$

where $D = [\hbar\Delta\omega_{\rm cm} - \hbar^2\Delta k^2/2m - mc^2]/mc^2$ [14]. Note that u_j corresponds to the branch of the dispersion with $\Delta k > 0$, and $v*_j$ the branch with $\Delta k < 0$.

In the regime of low energy excitations ($\Delta\omega_{\rm cm} \sim c\Delta k$), quasiparticles are

phonons, propagating with the group velocity, $c+v$. Suppose the flow is left-moving, with negative v. When $|v|/c > 1$, the flow is supersonic; when $|v|/c < 1$, the flow is subsonic. A sonic horizon is defined at the critical position between the regions of subsonic/supersonic flow, where $c = -v$.

Now we consider two scenarios of mode mixing occurring at a sonic horizon as shown in Fig. 3.4(a-b). Here we suppose the horizon has a step-like structure, in which the flow is uniform on either side of the horizon, one side being supersonic ($v > c$), the other being subsonic ($v < c$).

The first case is the Čerenkov effect at a stationary WH, as illustrated in Fig. 3.4(a). It involves a zero-frequency WH undulation in the supersonic region. In Ref. [35], it was reported that a perturbation which disturbs the flow at the WH from the stationary condition can cause such undulation. This instability can also be viewed as the Bogoliubov–Čerenkov radiation (BCR), $\psi_{\rm BCR}$, as indicated in the dispersion curve in the lower panel of Fig. 3.4(a). It corresponds to a zero-frequency mode in the dispersion relation, coupled with the supersonic flow through a perturbation [36]. Especially, as the $|v/c|$ ratio becomes large, the point at which $\Delta\omega = 0$ will move toward the single-particle regime (i.e. $\Delta\omega_{\rm cm} \sim \hbar\Delta k^2/2m$), such that $\Delta k_{\rm BCR} \sim -2k_{\rm bf}$, and the overall wavevector of $\psi_{\rm BCR}$ in Eq. 3.2 becomes $k_{\rm bf} + \Delta k_{\rm BCR} \sim -k_{\rm bf}$. This feature is observed in our simulation, which will be discussed later.

The second scenario in Fig. 3.4(b) illustrates a pair creation process at a stationary BH, stimulated by an incident mode on the left, $\psi_{\rm in}$, with nonzero frequency, $\Delta\omega_{\rm in}$. The right-propagating, incident mode produces a Hawking radiation, $\psi_{\rm HR}$, on

the supersonic side, and its partner mode, $\psi_{\rm p}$, on the subsonic side, all at the same frequency. The lower panel of Fig. 3.4(b) shows the dispersion in the supersonic region (red curve) and that in the subsonic region (blue curve). Given the dispersion relations and the incident mode frequency (denoted by the horizontal dashed line), the HR and p modes are determined. The HR is the right-propagating mode on the subsonic dispersion curve, and its partner is the left-propagating mode on the supersonic one. Matching the modes at the BH (for the components with $\Delta\omega < 0$) gives

$$u_{\rm in} e^{-i\Delta\omega_{\rm in} t} e^{i\Delta k_{\rm in} x}|_{\rm BH} = \alpha u_{\rm p} e^{-i\Delta\omega_{\rm p} t} e^{i\Delta k_{\rm p} x}|_{\rm BH} + \beta v^*_{\rm HR} e^{i\Delta\omega_{\rm HR} t} e^{-i\Delta k_{\rm HR} x}|_{\rm BH}, \qquad (3.5)$$

where α and β are the coefficients for the p-mode and the HR, respectively. Like a scattering process, this mode relation implies that the HR pair should have the same frequency as the incoming mode, $\Delta\omega_{\rm p} = -\Delta\omega_{\rm HR} = \Delta\omega_{\rm in}$. This is indicated by the dashed horizontal line in the lower panel of Fig. 3.4(b).

When the background flow is smooth in the transonic region, a similar mode relation can be derived [37], and the ratio of coefficients α and β can be estimated using the thermal prediction, $|\beta/\alpha| = \exp(\hbar\Delta\omega_{\rm in}/2kT_{\rm H})$. The Hawking termperature $T_{\rm H}$ is related to the surface gravity κ by $T_{\rm H} = \hbar\kappa/2\pi k$, and in the sonic analog, the surface gravity is given by the slope of the velocity profile at the horizon, $\kappa = d(v+c)/dx$ [16]. A more detailed mode analysis regarding the Hawking effect can be found in [37].

In our simulations, we study a system which involves both the BH and the WH, forming a supersonic cavity in an inhomogeneous, elongated condensate, as

shown in Fig. 3.5(b). Both scenarios are encountered in our simulations. In fact, we will argue that the BCR from the WH plays the role of the incident mode $\psi_{\rm in}$, whose frequency is Doppler-shifted as it propagates at the BH, as illustrated in Fig. 3.3(b). Note that, although the system is inhomogeneous, when the background flow varies slowly compared to the BdG modes, the description in Eqs. 3.2,3.3 can be used to understand the local behavior of the modes.

3.2 Methods

We model the step-sweeping experiment in [1] by solving the time–dependent one-dimensional GP equation, using parameters similar to those in the experiment (details in Appendix A.1.1). For comparison, we perform a 3D simulation using the GPE in cylindrical coordinates (imposing symmetry in azimuthal direction, ϕ), which is given in Appendix A.1.2.

As pointed out by Eq. 3.1, the GP wavefunction Ψ in our simulation is composed of a background condensate flow $\Psi_{\rm bf}$ and its excitations ψ_j. In regions where the flow is slowly varying, each component in Eq. 3.1 behaves locally as a WKB plane wave with a characteristic frequency and wavevector. In this chapter, we implement two techniques to resolve locally individual components and their spectral properties.

3.2.1 Windowed Fourier transform

A windowed Fourier transform (WFT) [38] is a method that brings out the "local" spectral elements of a function in the neighborhood of a given position or time. It differs from the normal Fourier transform by including a Gaussian function certered at the position (x) or time (t) of interest. The spatial WFT $F(k,x)$ of a function $f(x)$ is defined as:

$$F(k,x) = \int_{-\infty}^{\infty} dy\, f(y) w(y-x;D) e^{-iky}, \tag{3.6}$$

where $w(y-x;D) = \exp(-(y-x)^2/D^2)/\left(\sqrt{\pi}D\right)$ is a Gaussian window function of width D. With the filtering of the window, the transformed function $F(k,x)$ constitutes a local Fourier transform of $f(x)$, capturing features that vary on length scales much smaller than D. For instance, given a function, $f(x) = f_q(x)\exp(iqx)$, with wavevector q and slowly varying amplitude $f_q(x)$, the transformed function is $F(k,x) \approx f_q(x)\exp(-(k-q)^2(D/2)^2)$: a Gaussian in k-space, centered at $k = q$ with width $2/D$, and the peak height is the local amplitude, $f_q(x)$.

The WFT is able to resolve locally (at a given x or t) the Fourier components in Eq. 3.1 as peaks in the resulting wavevector (or frequency) spectrum, in which peak position and height indicate the wavevector and amplitude of each component. Specifically, for a background condensate flow, $\Psi_{\rm bf} \sim |\Psi_{\rm bf}(x)|e^{ik_{\rm bf}(x)x}$, its spatial WFT exhibits the local wavevector $k_{\rm bf}(x)$ for each x, which determines the local flow velocity in the lab frame, $\hbar k_{\rm bf}(x)/m$. This is shown as the main streak in Fig. 3.5(a). Similarly, the spatial WFT of the density, $n(x) = |\Psi(x)|^2$, can separate

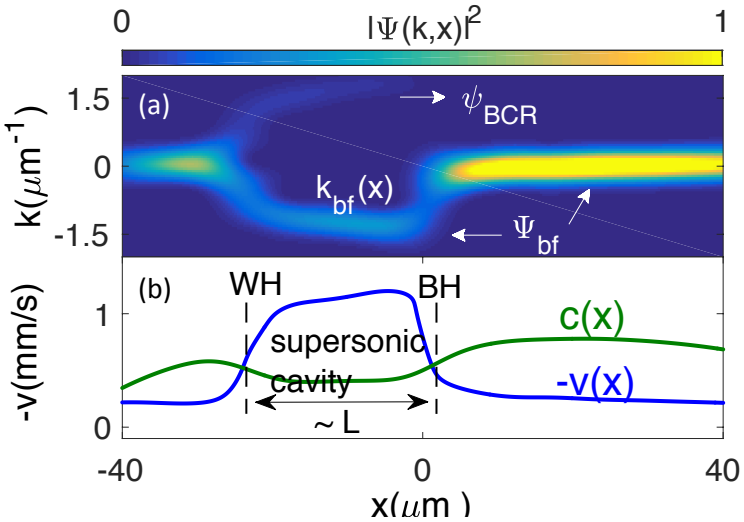

Figure 3.5: The velocity profile, the speed of sound, and the windowed wavevector spectrum. Panel (a) windowed wavevector spectrum of a BEC during the sweep, showing an accelerated flow generated by the moving step, edge at $x = 0$; the peak location is denoted by $k_{\rm bf}(x)$; panel (b) flow speed in the step frame $-v(x)$ and speed of sound $c(x)$, which (in a globally stationary flow) are equal at the horizons, WH and BH.

the background condensate density $n_{\rm bf}(x)$ ($k = 0$) from a superimposed spatial oscillations (with nonzero k). An example is shown in Fig. 3.8(b), which is the spatial WFT of density profile in Fig. 3.6(g), evaluated at the center of the oscillatory region. The spectrum has a central peak $n_{\rm bf}$ as the background density, and two side peaks n_k, indicating the oscillatory component.

3.2.2 Moving average of the GP wavefunction

To separate fast-oscillating components in Eq. 3.1 from the slowly-varying parts, we implement a smoothing procedure on the GP wavefunction. The procedure is equivalent to calculating the moving average of a discrete data set, which smooths out short-range fluctuations. Here the moving average of wavefunction $\Psi(x)$ is

defined as

$$\bar{\Psi}(x) = \frac{1}{2D_s} \int_{x-D_s}^{x+D_s} dy\, \Psi(y), \tag{3.7}$$

where the integral serves as a square window of width $2D_s$ centered at x, over which $\Psi(x)$ is being averaged. For components in $\Psi(x)$ with wavelength shorter than D_s (i.e. $D_s > \pi/k$), the integral would give rise to an average of zero, leaving those that are slowly varying in space (i.e. $\pi/k > D_s$) in $\bar{\Psi}(x)$, and the difference $\delta\Psi \equiv \Psi - \bar{\Psi}$ characterizes the part of Ψ composed roughly of wavevectors $k \gtrsim \pi/D_s$. Later in Sec. 3.4.2, we use the above procedure at each time and exhibit a spacetime diagram of $|\delta\Psi(x,t)|$, in which the slowly-varying part of the background flow ($\Psi_{\rm bf}$ with $k \sim 0$) is removed to bring out $\psi_{\rm HR}$.

3.3 Simulation for the experimental regime

3.3.1 Formation of the BH-WH cavity

Earlier in the introduction, we exhibit a simulated flow structure, shown in Fig. 3.5(b), which is produced following the step-sweeping procedure descriped in [1]. To determine such flow structure, we implement the spatial WFT described in Sec. 3.2.1. Figure 3.5(a) is a local wavevector spectrum $|\Psi(k,x)|^2$ with $D = 5$ μm, defined in the lab frame at a moment during the sweep (Fig. 3.6(e)). There is a dominant streak, indicating the background condensate flow, $\Psi_{\rm bf}$, for which the peak position at each x defines the background wavevector, $k_{\rm bf}(x)$. The regions with zero wavevector, $k_{\rm bf} \sim 0$, correspond to the non-accelerated, subsonic BEC;

the region behind the step with $k_{\rm bf} \sim -1.4\ \mu{\rm m}^{-1}$ corresponds to the accelerated, supersonic flow. The blue curve in Fig. 3.5(b) is the flow speed in the rest frame of the step, $-v(x) = v_{\rm s} - v_{\rm bf}(x)$, where $v_{\rm bf}(x) = \hbar k_{\rm bf}(x)/m$ is the background flow velocity. The green curve is the local speed of sound $c(x) = \sqrt{g n_{\rm bf}(x)/m}$, where $n_{\rm bf}(x)$ is the local density of the background flow, which we identify here using a WFT of the density $n(x)$.

3.3.2 Density profile and the cavity standing wave

Figures 3.6 show comparisons of the simulated density profile with experiment. Panels (a-g) show the BEC density for $U_s = k \times 6$ nK after the launch of a sweep at 20 ms intervals, where k is the Boltzmann constant. Panel (h) corresponds to the density profile at $t = 120$ ms for $U_s = k \times 3$ nK. The coordinate origin in each panel has been displaced to coincide with $x_{\rm BH}$. In this section, we report the results of

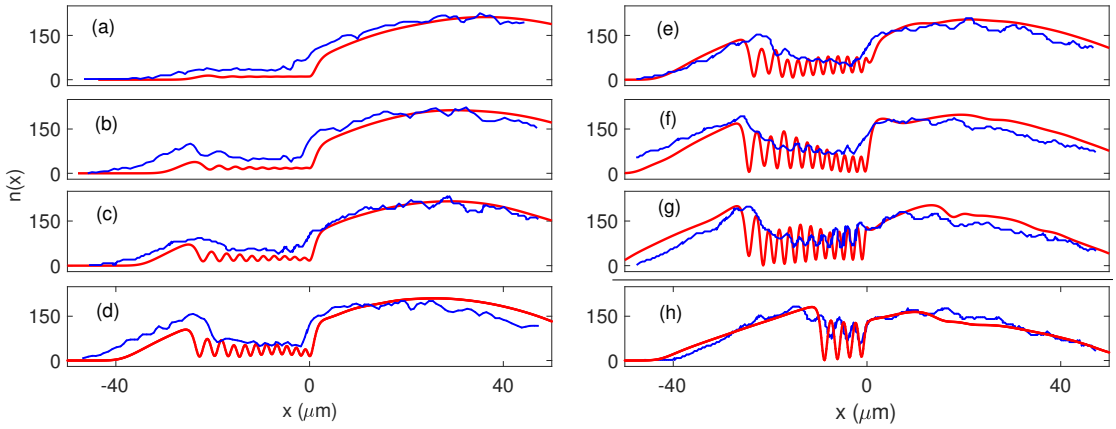

Figure 3.6: Evolution of the 1D condensate and a growing standing wave. Panel (a-g) Density vs. time of a swept BEC at 20 ms intervals with step $U_s/k =$ 6 nK, scaled by a common factor to match experiment, and viewed in the moving frame where $x = 0$ defines the step edge; panel (h): $U_s/k =$ 3 nK at 120 ms. Blue: experiment [1]; Red: present simulation.

1DGPE based on the procedure and parameter reported in the experiment [1].

The density exhibits a standing-wave pattern behind the step, with amplitude growing in time. Considering that the experimental observations involve an average over any quantities that fluctuate from one run to another, the GP simulation qualitatively matches the overall evolution seen in the experiment. In particular, the growth, wavelength, and phase of the wave pattern are similar to each other.

3.4 BCR mechanism and Stimulated Hawking radiation

We find that the growing standing wave observed in our simulation should be attributed to the BCR effect from the WH, as illustrated in Fig. 3.7(a). In the WFT spectrum in Fig. 3.5(a), we observe in the cavity region an excitation mode at $k \sim 1.4\ \mu\mathrm{m}^{-1}$ coming from the WH, which is roughly the reflection of the supersonic flow Ψ_{bf} with $k \sim -1.4\ \mu\mathrm{m}^{-1}$. The interference of the two results in the standing wave in the density profile shown in Fig. 3.6(e) , which has a wavevector with twice the above value, $k \sim 3\ \mu\mathrm{m}^{-1}$. This pattern is consistent with the observation in [36] for the case of large v/c ratio, as discussed in Sec. 3.1, and the excited mode should be identified as ψ_{BCR}.

In the following, we will show additional evidence from various approaches to support this BCR mechanism, its growth due to increasing BEC density, and the HR pair it stimulates at the BH. First, we analyze the growth relation of the standing wave in comparison with that of the background flow density. Second, we present a spacetime portrait for the evolving BEC, showing that the standing wave is

generated from the WH, and that its frequency is Doppler-shifted in the step frame due to the fact the WH recedes from the BH as the system evolves. This Doppler effect is verified quantitatively through a windowed frequency spectrum evaluated inside the cavity. Lastly, we find a signal of Hawking radiation from the spacetime portrait, which is stimulated by the BCR as it propagates at the BH.

3.4.1 Growth of the standing wave

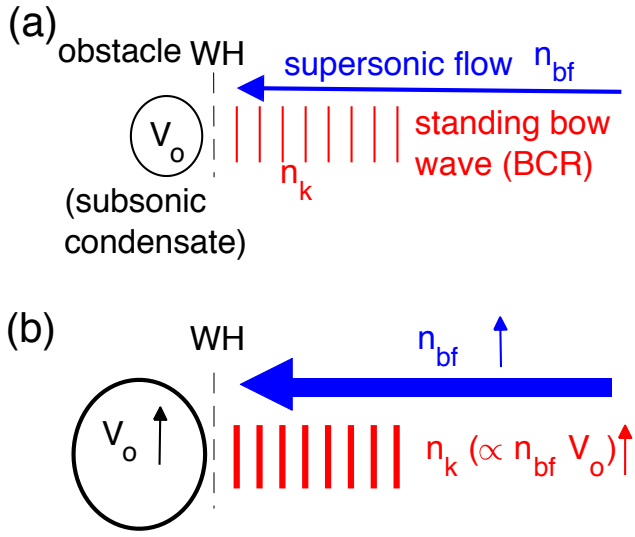

Figure 3.7: Bogoliubov-Čerenkov mechanism. (a) Illustration of a standing wave (BCR) against an obstacle (subsonic BEC) near the WH; (b) growth of the standing wave amplitude (n_k) resulting from the increase of background density ($n_{\rm bf}$) and obstacle strength ($V_{\rm o}$).

Reference [1] reported exponential growth of the oscillatory density pattern in the BH-WH cavity, and suggested that it results from the black hole laser effect. Our simulations exhibit similar growth, but lead us to attribute it to a different mechanism. Fig. 3.8 displays the growths of the background flow density $n_{\rm bf}$ and of a standing wave, n_k, that is defined by the peaks of the WFT of the density at

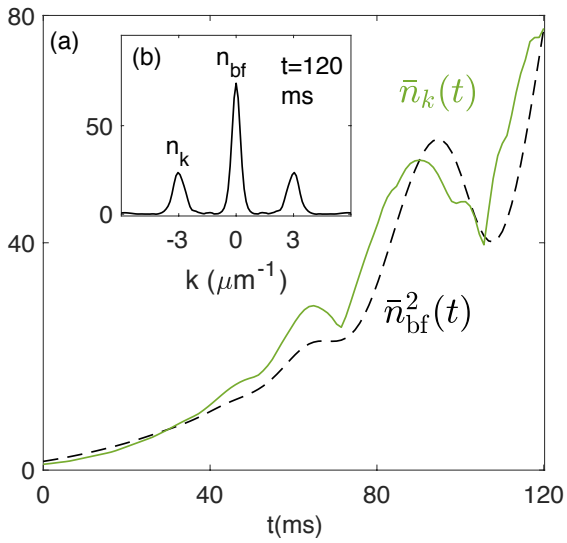

Figure 3.8: Growths of the cavity standing wave and the background density. (a) Simulated growth of the standing-wave pattern in the supersonic region for $U_s/k = 6$ nK. Green: normalized standing-wave amplitude $\bar{n}_k(t)$, $\bar{n}_k(t) = n_k(t)/n_k(0)$, for which $\ln[\bar{n}_k(120)] \sim 4.4$. Dashed black: the square of background density, $\bar{n}_{\rm bf}(t)$, scaled to match the final standing-wave amplitude, $\bar{n}^2_{\rm bf}(t) = n^2_{\rm bf}(t)[\bar{n}_k(120)/n^2_{\rm bf}(120)]$. The growth of $n_{\rm bf}$ and n_k is determined from a spatial WFT of $n(x)$ at $x = -12$ μm with window width $D = 6.5$ μm. Inset (b) shows the windowed wavevector spectrum at t=120 ms.

$x_{\rm BH} - 12\mu$m, as shown in the inset. Over 120 ms the standing wave density grows by $\sim \exp(4.4)$.

Regarding the mechanism, note that the step moves toward the region of higher BEC density (see Fig. 3.1), so the background density $n_{\rm bf}$ also grows. Fig. 3.8(a) shows that n_k grows in proportion to $n^2_{\rm bf}$. This relation can be explained as resulting from the Čerenkov effect. As illustrated in Fig.3.7(a), an obstacle in a stationary supersonic flow produces an upstream, Bogoliubov-Čerenkov standing wave [36, 39], analogous to a bow wave on water [40]. It was observed in Ref. [35] that such a standing wave is generated at a WH, triggered by an incident wavepacket on the stationary flow. In our case, the subsonic component on the LHS of the WH serves

as an obstacle in the supersonic flow, generating a Bogoliubov-Čerenkov wave whose amplitude (n_k) should be proportional to the strength of the obstacle ($V_{\rm ob}$) times the density of the background flow ($n_{\rm bf}$) [32, 36] (see Fig.3.7(b)). Since the "obstacle" itself has a strength proportional to the BEC density to the left of the WH, which grows similarly to that on the right, the saturated wave amplitude n_k grows as $n_{\rm bf}^2$.

The very close agreement between the standing wave amplitude and the background density is a strong evidence for the BCR mechanism. This is in contrast with the interpretation in [1] that quantum fluctuations in the BEC get amplified through the laser mechanism, resulting in the standing wave and its growth.

In addition, the growing standing wave is also associated with a checkerboard pattern the density-density correlation function shown in Fig. 3.2(c), regarding that the two show very similar periodic features. The growth of the checkerboard is numerically measured through the Fourier spectrum of the correlation, which grows by $\sim \exp(3.3)$. In Chapter 4, we will present the calculation of the correlation function, by introducing quantum fluctuation and atom-number fluctuation. Incorporating these fluctuations produces a correlaiton function with very similar checkerboard features as in [1]. There we will show that the checkerboard is simply the result of the standing wave, which grows as the standing wave grows.

3.4.2 Spacetime portrait of BCR and stimulated Hawking pair

In the following, we focus on the stimulated mechanism of the HR pair due to the standing wave, BCR. Fig. 3.9 shows the stimulated mechanism, which is viewed

in the lab frame where the BH moves at the step velocity, $v^0_{\rm BH} = v_s$, and the WH with a slightly smaller velocity, $v^0_{\rm WH} = v_s - \Delta v$, as indicated by the red dashed line and triangle. The BCR (or the standing wave) has zero phase velocity with respect to the WH, which correspond to zero frequency in the WH frame. Since the WH velocity is less than the BH velocity (as shown in Fig.3.10(a)), this gives rise to a nonzero frequency in the BH frame. As the BCR mode propagates to the BH, it will stimulate the emission of HR and the p-mode at the latter frequency, with the associated wavevectors determined by the Bogoliubov-de Gennes (BdG) spectrum.

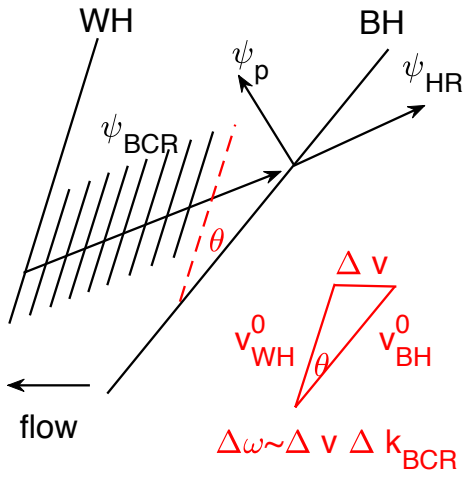

Figure 3.9: Pair production, stimulated by a Doppler-shifted BCR mode. Spacetime portrait of HR (ψ_{HR}) and its partner ($\psi_{\rm p}$) created at the BH by right-propagating BCR ($\psi_{\rm BCR}$) generated at the WH as a standing wave. Due to the recession of WH, indicated by the dashed red line and angle θ, the BCR (which has zero frequency in the WH frame) stimulates the Hawking pair at a nonzero frequency, $\Delta\omega_{\rm pair} \sim \Delta v \Delta k_{\rm BCR}$, where Δv is the velocity difference between the two horizons, as indicated by the red triangle.

The mechanism illustrated in Fig. 3.9 can be seen in the simulated spacetime portrait for the experiment, Fig. 3.10(a), in which $|\delta\Psi| = |\Psi - \bar{\Psi}|$ is calculated at each t using the procedure described in Sec. 3.2.2. To resolve the HR outside the cavity, we subtract the moving average $\bar{\Psi}$, which approximates the dominant,

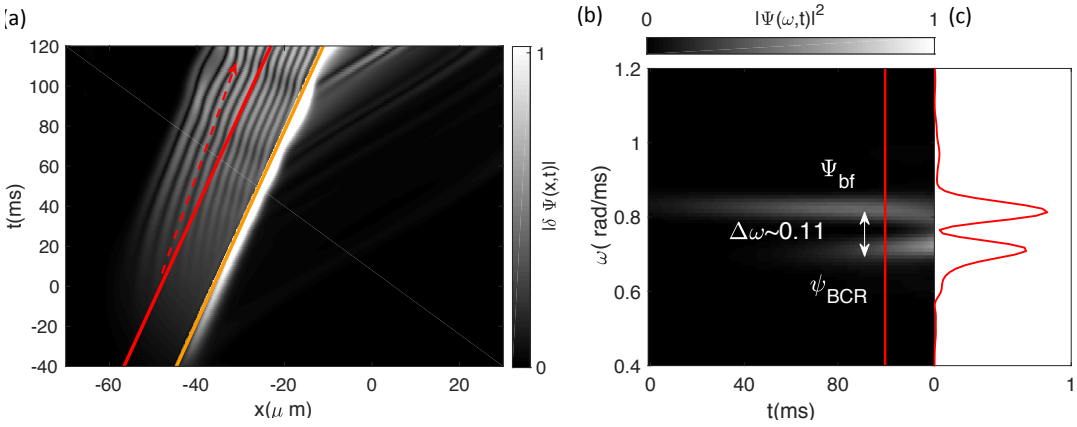

Figure 3.10: The spacetime portrait and the windowed frequency spectrum. Panels (a): time evolution of $|\delta\Psi(x,t)|$ in the experimental regime [1], multiplied by 10 for $x > x_{\rm BH}$, where $x_{\rm BH}$ is shown by the solid orange lines. The Doppler shift is outlined by the dash red line (parallel to WH) and solid red line (parallel to BH). Note that the spacetime portrait is viewed in the lab frame, where $x = 0$ at the center of the original trap. Note the p-mode/HR pair creation event at $t \sim 100$ ms. Panel (b): windowed frequency spectrum evaluated along the solid red line in (a); panel (c) is the cut-through of the spectrum at t= 100 ms.

slowly-varying background (with $k \sim 0$ as in Fig. 3.5(a)), from GP wavefunction Ψ. We choose the smoothing window $D_s = 5.4$ μm, such that it is large enough so that $\bar{\Psi} \approx 0$ between the horizons, yet small enough to capture the slow variations of the background outside the horizon.

The portrait displays an interference pattern between the background supersonic flow and excited modes of $\delta\Psi$. The evolution of the BH is indicated by the orange diagonal line. To clearly display HR upstream of the horizon, we have multiplied $|\delta\Psi|$ there by a factor of ten. At the beginning of the evolution, as the condensate spills over the step, a left-moving flow develops, indicated by the growing light gray area. When this flow reaches the WH, at $t \approx 10$ ms, a standing wave (BCR) is generated, and grows independently before reaching the BH. In Fig. 3.10(a), it is clear by inspection of the dashed red line and solid red line (which is parallel to

orange line) that the standing wave has zero frequency in the WH rest frame, but nonzero frequency in the BH rest frame.

Another crucial feature in the spacetime portrait is the stimulated HR. The BCR first reaches the BH at $t \approx 50$ ms, stimulating emission of HR with the BCR frequency in the rest frame of the BH. The left–moving partner radiation (p-mode) resulting from the "pair creation" forms a "V"-shape with the HR, and makes an interference pattern with the BCR. Note that in Fig. 3.10(a) the standing wave has grown substantially prior to the pair creation. Moreover, the p-mode that is created at the BH at $t \sim 50$ ms (Fig. 3.10(a)) only reaches the WH late in the evolution, at $t \sim 90$ ms, so there is insufficient time for multiple lasing cycles (round trip bounces) to account for the standing wave in our simulation.

3.4.3 Windowed frequency spectrum and the Doppler effect

The Doppler effect due to the receding WH can be estimated by the velocity difference between the two horizons, Δv, as illustrated by the red triangle in Fig. 3.9(a). The shifted frequency is the product of Δv and the BCR wavevector, Δk_{BCR}.

In Fig. 3.10(b-c), we show the windowed frequency spectrum in the experimental regime in the supersonic region (along the red line in Fig. 3.10(a)). The long streak, which starts from the beginning of the evolution, correspond to the background flow, Ψ_{bf}. The short streak, which is separated from the long streak by $\Delta\omega \sim 0.11(3)$ rad/ms, corresponds to the BCR (and the p-mode).

We can estimate this frequency shift independently using Eq. 3.2 and the BCR wavevector observed in 3.5(a)

$$\Delta\omega = \pm\Delta k_{\mathrm{BCR}}(v_{\mathrm{BH}} - v_{\mathrm{WH}}) = \pm 0.09 \text{ rad/ms}, \tag{3.8}$$

where v_{BH} and v_{WH} are the flow velocities measured in the BH and WH reference frames, respectively; the difference of the two is equivalent to Δv. Although the relative velocity between the BH and WH is small, Δk_{BCR} is nevertheless large enough that the BCR has a definite nonzero frequency in the BH frame, as is also evident by inspection of Fig. 3.10(a). We find that the WFT frequency agrees with the prediction using Eq. 3.2 to within the uncertainty. The quantitative agreement of the Doppler-shifted frequency supports the stimulated mechanism proposed here.

3.5 Enhanced parameter regime

To enhance the signal of stimulated HR, we vary the parameters of the external potential given in [1]: axial trap frequency ω_x, step strength U_{s}, and step speed v_{s}. We find parameter regimes in which clear feature of stimulated pair production can be observed. This investigation can help understand the stimulated Hawking effect in a trapped condensate, and detect it in laboratories.

In the experimental regime in Sec. 3.3, the signal of HR is weak to be directly observed from the density profile in Fig.3.6. With the spacetime portrait in Fig. 3.10(a), we capture signal from the BH that resembles the HR but with irregular wavelength. This irregularity may be due to the long wavelength of the p-mode, λ_{p}, relative to the cavity size, L, as shown in Fig. 3.10(a). Since $\lambda_{\mathrm{p}} \sim L$, the p-mode

does not behave as a WKB mode on a slowly-varying background, and may cause the irregular emission of the HR mode. Taking this into account, we lower the $\lambda_{\rm p}/L$ ratio by modifying the parameters of the trapping potential (axial trap frequency ω_x) and the step potentials (U_s , v_s). Fig. 3.11(a) show the density profile in one such modified regime (case M2), from which sharper signals of HR and p-mode have been observed, with suppresed $\lambda_{\rm p}/L$ ratio. In this case, the BEC is twice as long as in the experiment of [1], the step size is halved, and the step speed is about the same. The details of the investigation of parameter regimes are summarized in Appendix 3.

The spacetime portrait of the modified regime is shown in Fig. 3.11(b). The BCR-stimulated pair production illustrated in Fig. 3.9 can be seen very clearly with more distinct features than the experiment regime (Fig. 3.10(a)): (i) the BCR parallel to the WH, which grows substantially prior to the pair creation, (ii) the "V"-shaped HR pair, stimulated by the BCR. The frequency of $|\delta\Psi|$ appears doubled outside the BH compared to that inside. This is because $\delta\Psi$ contains very little background flow component with which to interfere outside the BH, so the visible interference is between the positive and negative frequency parts of the HR.

Furthermore, since the HR and the p-mode have enhanced signals and sharper wavelengths here, we can can capture their spectral properties using WFT, and analyze them using the models in Sec. 3.1.

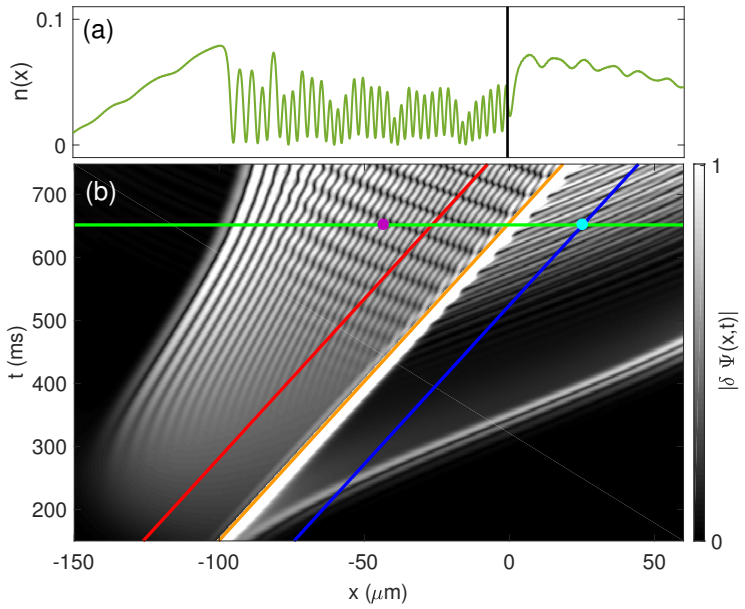

Figure 3.11: Stimulated pair production in the enhanced regime, M2. Panel (a): density $n(x)$ at $t = 650$ ms, along the green line in (b); panel (b): spacetime portrait. The red and blue lines indicate the paths on which the windowed frequency spectra of Fig. 3.13(a) are calculated. The wavevector spectrum along the green line is shown in Fig. 3.13(b). The magenta dot and cyan dot correspond to a correlated Hawking pair, for which the thermal prediction is being tested.

3.5.1 BdG mode analysis

The BdG theory of linearized modes [32] (Sec. 3.1) can be used to predict the temporal and spatial WFT spectra of the BEC, starting from only one input assumption: that the standing wave has zero frequency in the WH frame. This will further verify the mechanism we have proposed for the excitations of the BEC. In addition, it will demonstrate the remarkable accuracy of BdG analysis when combined with WFT in an inhomogeneous setting.

In the enhanced regime, the dispersion relations evaluated inside and outside the BH at $t = 650$ ms are shown in Fig. 3.12. The red and blue solid curves indicate the dispersion relation in the BH frame ($v = v_{\rm BH}$), at $x_{\rm I} = x_{\rm BH} - 26$ μm and $x_{\rm O} =$

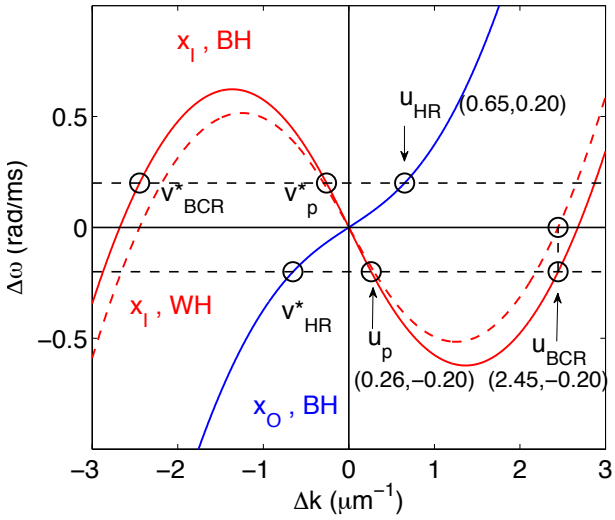

Figure 3.12: Dispersion relations of $\Psi(x,t)$ ($\delta\Psi(x,t)$ for $x > x_{\rm BH}$) along the lines indicated in Fig. 3.11(b). Dispersion relations at $x_{\rm I}$ in the WH (dashed red) and BH (solid red) reference frames, and at $x_{\rm O}$ in the BH reference frame (solid blue), evaluated at $t = 650$ ms. $\Delta\omega$ and Δk are the frequency and wavevector relative to those of the background flow.

$x_{\rm BH}$+26 μm, respectively. The dashed red curve also indicates the dispersion relation at $x_{\rm I}$, but referred to the WH frame ($v = v_{\rm WH}$). We use the numerically measured values of the local flow velocity and sound speed, determined from the background flow $\Psi_{\rm bf}$, which can be identified by a spatial WFT (despite the appearance of additional excitations). The WH velocity is approximated by the speed of the left edge of $|\delta\Psi(x,t)|$ (see Fig. 3.11), while the BH velocity is that of the step.

According to the mechanism illustrated in Fig. 3.9, the BCR has zero frequency in the WH frame, and the HR and the partner share its frequency in the BH frame. The BCR wavevector in the WH frame should therefore satisfy $\Delta\omega(\Delta k_{\rm BCR}) = 0$. This is indicated graphically by the intersection of the dashed red curve in Fig. 3.12 with the Δk axis, showing that $\Delta k_{\rm BCR} \sim 2.5\,\mu{\rm m}^{-1}$. Due to the recession of WH relative to the BH, the frequency of BCR in the BH frame corresponds to $\Delta\omega =$

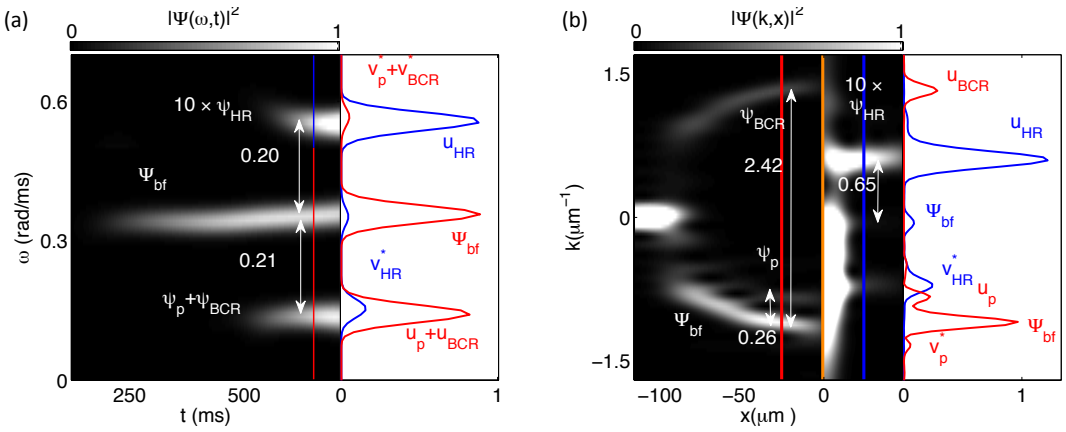

Figure 3.13: WFTs of $\Psi(x,t)$ ($\delta\Psi(x,t)$ for $x > x_{\rm BH}$) along the lines indicated in Fig. 3.11(b). (a) frequency spectrum along the diagonal red ($x_{\rm I}$) and blue lines ($x_{\rm O}$); (b) wavevector spectrum along the horizontal green line ($t = 650$ ms).

$\pm\Delta k_{\rm BCR}\Delta v = \pm 0.2$rad/ms, which is indicated by the horizontal, dashed black lines, which intersect the solid red curve at the vertical lines, $\pm\Delta k_{\rm BCR}$. If the HR and partner modes are indeed stimulated by the BCR, they should fall on the intersection of these zero WH frequency lines with the solid blue and red curves respectively. The modes are labeled by "u" or "v^*", according to the corresponding component of the BdG mode. Modes whose u-component has negative (positive) relative frequency in the step frame have negative (positive) energy relative to the condensate [37]. The BCR and partner modes thus have negative energy, while the Hawking mode has positive energy.

3.5.2 Spectral comparison with BdG prediction

To capture the spectral properties of the modes observed in Fig. 3.11, and compare with the prediction in Fig. 3.12, we apply the spatial and temporal WFTs on $\Psi(x,t)$ and $\delta\Psi(x,t)$. On the LHS of the BH ($x < x_{\rm BH}$), we calculate the

WFTs of $\Psi(x,t)$; on the RHS of the BH ($x > x_{\rm BH}$), we take $\delta\Psi(x,t)$ and multiply it by 10 to subtract the background and bring out the HR. The left panel of Fig. 3.13(a) shows the windowed frequency spectra of $\Psi(x_{\rm I}(t),t)$ (ω = 0-0.5 rad/ms) and $\delta\Psi(x_{\rm O}(t),t)$ (ω = 0.5-0.7 rad/ms), in the BH frame, along the red and blue lines in Fig. 3.11(b) with Gaussian width T = 55 ms. The streak in the center corresponds to the background flow $\Psi_{\rm bf}$, and indicates the frequency $\omega_{\rm bf} \sim 0.36$ rad/ms. The two other streaks located symmetrically about the center correspond to HR ($\omega \sim 0.56$ rad/ms), and the BCR and the p-mode ($\omega \sim 0.15$ rad/ms). The full frequency spectra at t = 650 ms for $x_{\rm I}$(red) and $x_{\rm O}$(blue) are shown on the right panel.

The left panel of Fig. 3.13(b) shows the windowed wavevector spectrum as a function of position, in the laboratory frame. It is defined by WFTs of $\Psi(x,t_0)$ ($x < x_{\rm BH}$) and $\delta\Psi(x,t_0)$ ($x > x_{\rm BH}$) at t_0 = 650 ms, along the green line in Fig. 3.11(b), with width D = 21 μm for Ψ, and 12 μm for $\delta\Psi$. The background flow spectrum between the horizons is centered on a large negative wavevector at each x, and extends from the BH to the WH. Similar to the wavevector spectrum for the experimental regime 3.5(a), the BCR spectrum is roughly the reflection of the background flow, $\Psi_{\rm bf}$. The HR and p-mode spectra extend outward and inward from the BH, with positive and negative wavevectors, respectively. The wavevector spectra at $x_{\rm I}$(red) and $x_{\rm O}$(blue) are shown on the right panel, with the modes labelled (except for $v^*_{\rm BCR}$) in the figure.

We compare the WFT spectra (Fig. 3.13(a-b)) with the BdG dispersion relations (Fig. 3.12) at $x_{\rm I}$ and $x_{\rm O}$, corresponding to the intersections of the red and

blue lines with the green line in Fig. 3.11(b). The numerical values of $\Delta\omega$ and Δk obtained from the WFT spectra of the GP solution are displayed in Table 3.1, along with those predicted from the BdG dispersion relations. The inputs to the BdG prediction are just (i) the assumption of zero frequency in the WH frame, and (ii) the velocity of the BH frame relative to the WH frame. The GP spectra and BdG predictions agree to within 5%. Note that the flow is not perfectly stationary, so that the zero frequency of the initial BCR is not perfectly conserved. Also, the speed of the WH changes slightly over time, which gives rise to the uncertainty in $\Delta\omega_{\rm BdG}$ and $\Delta k_{\rm BdG}$.

Table 3.1: Numerical values of relative mode frequency $\Delta\omega$(rad/ms) and wavevector $\Delta k(\mu{\rm m}^{-1})$ from the GP Fourier spectra (FT) and from the WH-zero-frequency BdG dispersion relation (BdG). The uncertainty for the former is estimated by the widths of the Gaussians fitting the spectral peaks in Fig. 3.13(a-b), and the uncertainty for the latter is due to the variation of the speed of WH.

Modes	$\Delta\omega_{\rm FT}$	$\Delta\omega_{\rm BdG}$	$\Delta k_{\rm FT}$	$\Delta k_{\rm BdG}$
$u_{\rm BCR}$	-0.21(3)	-0.20±0.01	2.42(8)	2.45±0.02
$u_{\rm p}$	-0.21(3)	-0.20±0.01	0.26(8)	0.26±0.01
$u_{\rm HR}$	0.20(3)	0.20±0.01	0.65(12)	0.65±0.02

3.5.3 Hawking temperature

Regarding the amplitudes of the BdG modes, we can apply the thermal prediction to determine individual coefficients for the mode-mixing process at the BH [41, 42]. For the opposite-norm coefficients in Eq. 3.5, the thermal prediction for a mode of frequency $\Delta\omega$ is $|\beta/\alpha| = \exp(-\pi\Delta\omega/\kappa)$. In terms of the amplitudes extracted from the GP wavefunction, the ratio becomes $|\beta/\alpha| = |V_{\rm HR}/v_{\rm HR}|/|U_{\rm p}/u_{\rm p}|$, where (U, V) are the full mode amplitudes which can be captured from the WFT

spectra, and (u, v) are the normalized BdG amplitudes defined in Eq. 3.4.

To test the thermal prediction we evaluate the mode amplitudes at a pair of points $x_{\rm p}$ and $x_{\rm HR}$ with a common retarded time, defined by phase velocity, at the BH. These points are denoted by the magenta and cyan dots on the horizontal green line in Fig. 3.11(b). The common retarded time on the horizon is $t = 588$ ms, for which we find the surface gravity $\kappa \sim 350$ s^{-1} (using v and c computed directly from the GP wavefunction, see Appendix 2). The thermal prediction for $\omega = 200$ rad/s is $|\beta/\alpha| = 0.17^{+.05}_{-.04}$, allowing for a 5% uncertainty in ω and a 10% uncertainty in κ. This agrees reasonably well with the ratio 0.21 computed directly from the amplitudes according to the thermal prediction. The Hawking temperature for the case M2 depicted in Fig. 3.11 is $T_{\rm H} = 0.43$ nK. The temperature equivalent of the chemical potential, μ, in that case is $\mu/k = 2.5$ nK.

3.6 Conclusion

To conclude, we summarize the evidence that the black hole laser effect plays no role in our GP simulations. First, we observe a growing standing wave in our simulaion similar to the observation in [1], and identifies is resulting from an instability at the WH, also called BCR. We resolve the spectral content of the GP wavefunction using the WFT procedure, and find that the standing wave pattern is an interference between the background condensate and a mode originated from the WH. We also find a growth relation between the amplitude of this mode and the background density. Both observations are consistent with the BCR effect.

Second, we present a space-time portrait, which shows (i) an independent growth of the standing wave (i.e. BCR), (ii) the signal of Hawking radiation, and (iii) a receding WH. Due to this recession, the frequency of the BCR mode is Doppler-shifted as it reaches the BH. Due to the large BCR wavevector, this frequency shift is visible, and is captured in a local frequency spectrum, which implies the suppression of black-hole lasing effect.

Lastly, we investigate over various regimes of experimental parameters, and find a regime where a sharper signal of HR can be obtained. This can be useful for investigating and observing stimulated HR in the future.

Chapter 4: Atom number variations and density correlations in sonic black hole condensates

In Chapter 3, we present the simulated results for the experiment [1], using a 1DGPE without introducing any fluctuations. In this chapter, we focus on the roles of quantum fluctuation and atom-number fluctuation and the resulting effects. With the presence of fluctuations in a simulated condensate of density $n(x)$, we calculate a density-density correlation, defined as $\langle \delta n(x) \delta n(x') \rangle$, where $\delta n(x) = n(x) - \langle n(x) \rangle$ is the deviation from the mean value. This chapter is based on an unpublished paper in collaboration with Ted Jacobson, Mark Edwards and Charles Clark.

Quantum fluctuation is presumably present in a BEC. However, in practice, the measured correlation function is not merely the quantum expectation value, because it inevitably includes an average over other aspects of an experiment that vary, such as the number of atoms in the system. In the following, we will show that this variation of atom number can have important consequences for the correlation function, affecting its physical interpretation.

In [1], a density-density correlation function is reported (see Fig. 3.2(c)). It was evaluated by repeating the measurement 80 times, with the condensate prepared under the same conditions each time. Based on the interpretation in [1], quantum

fluctuations can grow exponentially under a flow structure with a black-hole horizon (BH) and a white-hole horizon (WH), viewed as a "black-hole laser". This interpretation is associated with the growth of a checkerboard in the experimental correlation function, which is treated as evidence of black-hole lasing.

Earlier, we present the growth of a standing-wave mode in the density profile without incorporating quantum fluctuation, and attribute it as the BCR effect occurring at the WH. To clarify the underlying mechanism, we take into account quantum fluctuations as an initial spatial noise in the GP simulations, and test if any mode in the noise can grow significantly over the timescale of the experiment, generating a pattern similar to the checkerboard. On the other hand, we consider the possibility that a large standing wave may appear in the correlation and form the checkerboard. While the trap and step potentials are controlled with high precision, in typical BEC experiments the number of atoms in the trap varies from one sample to another. Such variation can modulate the background standing-wave present in all realizations, bring it out to the correlation in the form of a checkerboard.

Here we present the results with these two types of fluctuations. We show that much better agreement with the experimentally measured correlation function is achieved when variations in the atom number are included. In fact, the correlation function is quite well matched when the *only* variations are due to atom number. This somewhat surprising result is a consequence of the presence of the large standing wave, and the fact that the amplitude and phase of the standing wave are sensitive to the number of atoms, as explained in detail below. We also investigate the effect of quantum fluctuations, using the truncated Wigner (TW)

method [20,40,43–45]. With atom number variations included, the correlation function is in good qualitative agreement with the observed one in all respects. This result further verifies the stimulated mechanism proposed in Chapter 3.

4.1 Methods

The condensate in this chapter is simulated by the one dimensional Gross-Pitaevskii equation (1DGPE) as in Chapter 3. In order to optimize the fit to the experiment, we modify the experimental parameters for the trapping potential and the sweeping step. Details are given in Appendix B.1.

To simulate the variation of atom number N from shot to shot under experimental conditions, we calculate the condensate properties using a normal distribution of N with mean $\bar{N} = 6000$, and standard deviation ΔN. We consider three different values, $\Delta N = (0.05, 0.1, 0.15)\bar{N}$. For each value of ΔN, we ran 200 simulations of the experiment reported in [1], each with a random choice of N, and computed the average density and the density correlation function at one particular time.

To simulate the effects of quantum fluctuations in the condensate, we use the truncated Wigner approximation (TWA) [20, 40, 43–45]. In this method, the linearized perturbations of the GP wave function for the initial, stationary condensate, i.e. the Bogoliubov-de Gennes (BdG) modes, are populated with random phases, and with amplitudes according to the probability distribution defined by their quantum state. Because of the adiabatic theorem, the modes with frequencies

much higher than those that are dynamically relevant in the system should not affect the evolution. In our system, the dynamics of interest are: (i) the black hole lasing effect, which is bounded by the maximal frequency $\omega_{\rm max}$ in the dispersion relation of the supersonic flow, as mentioned in [1], (ii) the background standing wave, which has nonzero frequency in the BH frame but much smaller than $\omega_{\rm max}$ [34]. We select the number of BdG modes to $K = 200$, so that the frequency of the last mode is much greater than $\omega_{\rm max}$. We also test the simulation by increasing the number of modes, and the main features in the resulting correlation does not change.

When investigating the effect of the quantum fluctuations alone, we adjust the amplitude of the unperturbed part of the GP wave function for each realization so that the total N, after including the fluctuations, is the same for all realizations. Details are given in the following subsection.

4.1.1 Truncated-Wigner method

In the TWA method [43, 45] adopted in the simulation, one includes a fluctuation term in the GP field, $\delta\psi(x)$, which models small excitations on a given stationary condensate, $\Psi_0(x)$:

$$\delta\psi(x,t) \;=\; \sum_j e^{-i\mu t}\left(\beta_j u_j(x)e^{-i\omega_j t} + \beta_j^* v_j^*(x)e^{i\omega_j t}\right). \tag{4.1}$$

Here the functions u_j and v_j satisfy the coupled BdG mode equations, and are normalized by $\int dx\,(|u_j(x)|^2 - |v_j(x)|^2) = 1$, and β_j is a complex random number which at zero temperature is given by the probability distribution

$$P(\beta_j) \;=\; \frac{2}{\pi}\exp(-2|\beta_j|^2). \tag{4.2}$$

We solve the BdG equation numerically, at time $t = 0$ before the step potential is swept, for the first 200 modes. The modes above this cutoff do not have an important dynamical effect on the condensate, and are omitted. This gives rise to the total number of excited atoms

$$\begin{aligned} N_{\rm ex} &= \sum_j (|\beta_j|^2 - \tfrac{1}{2}) \int dx \left(|u_j(x)|^2 + |v_j(x)|^2 \right) \\ &+ \sum_j \int dx |v_j(x)|^2. \end{aligned} \tag{4.3}$$

Keeping the total atom number N fixed, the population in the condensate is given by $N_c = N - N_{\rm ex}$. Since $N_{\rm ex}$ fluctuates over individual realizations, N_c also fluctuates. The resulting stochastic wavefunction at time $t = 0$ is given by

$$\Psi(x) = \sqrt{N_c}\Psi_0(x) + \sum_j \left(\beta_j u_j(x) + \beta_j^* v_j^*(x) \right). \tag{4.4}$$

The expectation value implied by (4.2) is $\langle |\beta_j|^2 \rangle = 1/2$, so $\langle N_{\rm ex} \rangle$ is just the last term in (4.3), the quantum depletion of the condensate. The integral in the last term goes to zero as the wavelength drops below the healing length; here we find that it goes to zero for $j > 60$, and the quantum depletion converges to ≈ 34. In the TWA simulation, the mean value of the excited atom number is $\langle N_{\rm ex} \rangle \approx 33$, which is consistent with the quantum depletion, and its standard deviation is $\Delta N_{\rm ex} \approx 13$.

4.2 Results

4.2.1 Experimental density-density correlation

In the experiment of [1], a BH/WH cavity was generated by sweeping a step potential through an initially stationary condensate, and the density-density corre-

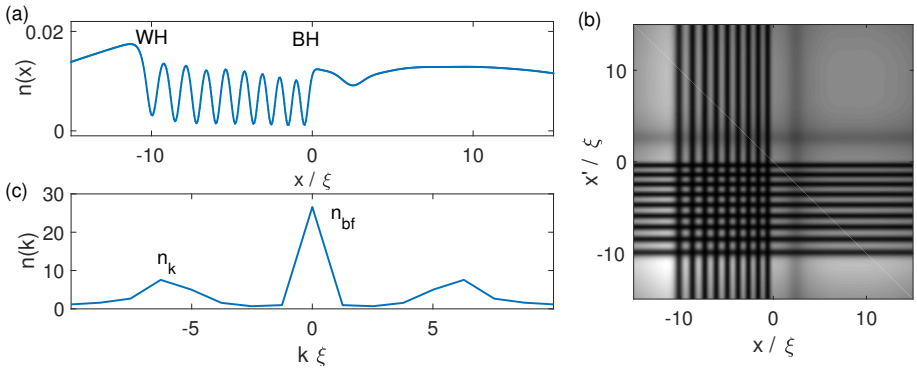

Figure 4.1: GP simulation and its wavevector spectrum. (a) density plot $n(x)$; (b) density-density plot, $n(x)n(x')$; (c) wavevector spectrum for $n(x)$ inside the cavity. Note that all the plots are based on the length unit ξ of the system, $\xi = 2$ μm.

lation function at a given time was measured by repeating the experiment 80 runs for each time. The correlation function discussed here is defined as

$$G^{(2)}(x,x') = \langle n(x)n(x')\rangle - \langle n(x)\rangle\langle n(x')\rangle \tag{4.5}$$

$$= \langle \delta n(x)\delta n(x')\rangle, \tag{4.6}$$

where $n(x)$ is the condensate density, the brackets correspond to the ensemble average over individual realizations, and $\delta n(x) = n(x) - \langle n(x)\rangle$. (The correlation function defined in Ref. [1] included the subtraction of a term $\langle n(x)\rangle\delta(x-x')$. We do not know whether this term was included in the spectrum presented in Ref. [2].)

Fig 4.2(h) [1] shows the experimentally measured ensemble average of the individual density profiles, featuring a standing wave behind the BH horizon (at $x = 0$), and Fig 4.2(d) [1] is the corresponding correlation function, which features a square array pattern in the upper right quadrant. This was called a "checkerboard" pattern in [1]. Figure 4.3(d) [2] shows the 2D wavevector spectrum, computed by Fourier transform with a square window, for this checkerboard. The top panel is the cut-through at $k'\xi = 5$, which exhibits three peaks, at $k\xi = 0, \pm 5$ (ξ denotes the

healing length in the cavity region estimated in the experiment [1], $\xi = 2\ \mu$m). The periodic features of the correlation match those of the density profile very well, as indicated by the magenta lines, suggesting that the two features may have the same origin. In the following, we investigate the roles of atom-number variations and quantum fluctuations in producing the correlation, and analyze how the standing wave is related to the observed correlation function.

4.2.2 Simulations with atom number fluctuations and quantum fluctuations

Fig. 4.1(a) displays the result of a single GP simulation, with a fix atom number and no quantum noise. A standing wave is seen inside the supersonic cavity, extending from the BH horizon at $x = 0$ to the WH horizon at $x \sim -10\xi$. The Fourier transform of $n(x)$ over a square window behind the BH horizon ($-5.5\xi < x < -0.5\xi$) gives rise to the wavevector spectrum shown in Fig. 4.1(c), with two side peaks corresponding to the standing wave, n_k, and a central peak coming from the background flow, $n_{\rm bf}$. The correlation function vanishes identically for a single deterministic simulation, but we show in Fig. 4.1(b) the density-density function $n(x)n(x')$, for the purpose of comparison with what is to come.

Figure 4.2 shows the results of simulations incorporating atom-number fluctuations (NF), quantum fluctuations (QF), and both types of fluctuations, as well as the experimental results. The bottom panels show the correlation functions. The top panels show the ensemble average of density $\langle n(x)\rangle$ (black curve) and, in (e-g),

a single random realization of the simulations, $n_i(x)$ (red curve). Fig. 4.3 shows 2D wavevector spectra of the correlation functions in Fig. 4.2, performed over the quadrant $-5.5\xi < x, x' < -0.5\xi$ in (a-c), and the top panels show the cut-through at $k'\xi = -6$. Panel (d) shows the experimental wavevector spectrum as given in [2].

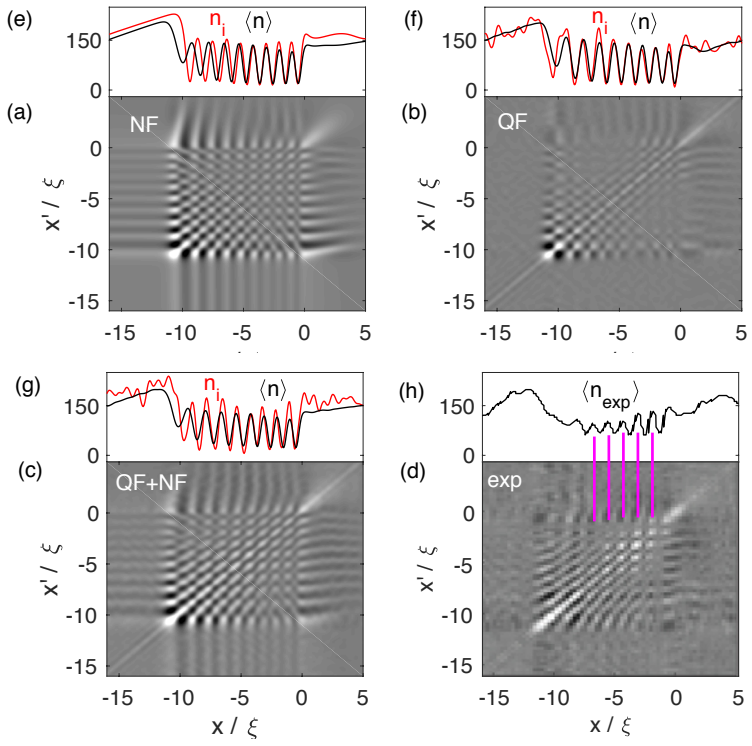

Figure 4.2: The density-density correlations by (a) number fluctuations, (b) quantum fluctuations, and (c) both. (d) experimental density-density correlation taken from [1]. Note that for panels (a) and (c), the number of condensate atoms fluctuates about $\Delta N/\bar{N} = 0.05$. Top panels (e-g) are the profiles of the averaged density $\langle n(x) \rangle$ (black) and that of one realization in the corresponding ensemble , $n_i(x)$ (red). Panel (h) is the ensemble average of experimental density, $\langle n_{\rm exp} \rangle$, taken from [1].

4.2.2.1 Atom number fluctuations

Figures 4.2(a,e) correspond to the case of fluctuating atom number N ($\bar{N} = 6000$, $\Delta N = 0.05\bar{N}$), without quantum fluctuations. The correlation function con-

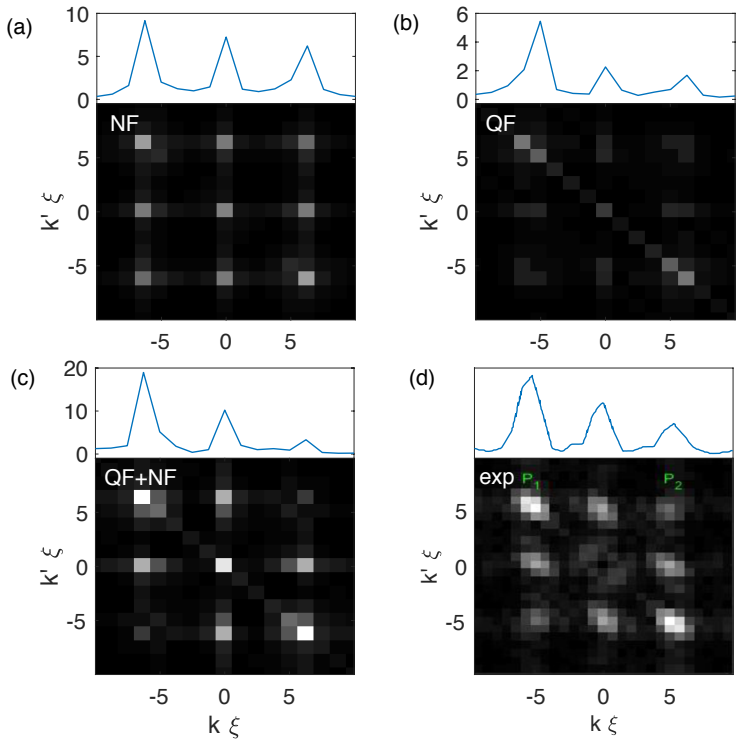

Figure 4.3: 2D wavevector spectra for the correlations by (a) number fluctuations, (b) quantum fluctuations, and (c) both. Bottom: 2D wavevector spectrum; top: cut-through of the 2D spectrum at $k'\xi = 6$ (note different scales on the plots). Panel (d): 2D wavevector spectrum of the experimental correlation taken from [2]; upper panel is its cut-through along P_1 and P_2. Note that for panels (a) and (c), the number of condensate atoms fluctuates about $\Delta N/\bar{N} = 0.05$.

tains a checkerboard similar to that in the experimental plot. Also, near the WH horizon, the pattern is partially smeared out into lines parallel to the diagonal. Figure 4.3(a) shows the 2D wavevector spectrum of Fig. 4.2(a) and its cut-through at $k'\xi = 6$. The peaks at $k\xi = \pm 6$ are consistent with the spacing of the squares in the checkerboard ($\sim 1\xi$). The peak at $k = 0$ indicates a non-oscillatory component. The 2D Fourier transform is quite similar to that in the experimental plot, Fig. 4.2(d), the principal differences being that in the simulation the peaks are somewhat more sharply defined and do not vary as much in intensity.

4.2.2.2 Quantum fluctuations

Figures 4.2(b,f) show the result of including quantum fluctuations using TWA simulations at zero temperature, with a fixed total atom number. In each run, these fluctuations correspond to "noise" added at the beginning of the evolution, which evolves with the condensate, and whose effect on a random realization is shown in the red curve of the top panel. The correlation function also contains a checkerboard in the cavity region, but not so distinct as in the NF case near the BH horizon. The bright diagonal line is a feature resulting from the quantum noise, which adds up constructively at $x = x'$ [44]. The 2D Fourier spectrum for Fig. 4.2(b) and its cut-through are shown in Fig. 4.3(b). As in the previous case, we find peaks at $k\xi \sim \pm 6$ corresponding to the checkerboard. In addition, there is an off-diagonal line, that arises from the diagonal line in the correlation function (since the Fourier transform of $\delta(x - x')$ is $\delta(k + k')$). The off-diagonal peak is thus enhanced relative to the other peaks. The intensity of all peaks is less than in the NF case.

4.2.2.3 Atom number and quantum fluctuations

Fig. 4.2(c,g) shows the result of incorporating both types of fluctuations together into the simulation. For each realization, we randomly select a total atom number N_i to determine the initial condensate, then introduce quantum fluctuations on top of this, and finally rescale the initial condensate wavefunction so that the total atom number, including the fluctuations, is N_i, before proceeding with the simulation. The checkerboard near the BH is consistent with the pure NF case, and

the presence of the diagonal line is due to the quantum fluctuations. The correlation function closely resembles the experimental one, Fig. 4.2(d,h), regarding the checkerboard near the BH, the diagonal line, and the parallel lines near the WH. The corresponding 2D wavevector spectrum is shown in Fig. 4.3(c). It combines features of panels (a) and (b). In particular, the peaks are broadened by the quantum fluctuations, and the off-diagonal peak is enhanced. This is qualitatively similar to the experimental spectrum Fig. 4.3(d), but the relative differences of the three peaks are greater in the simulation.

4.2.2.4 Comparison of different atom number variances

Figures 4.4(a-c) display the results incorporating both quantum fluctuation and number fluctuation, with three different values for the standard deviation, $\Delta N = (0.05, 0.1, 0.15)\bar{N}$. The top panels (e-g) show the ensemble average of density, $\langle n(x) \rangle$, given by the black curve, and that of a single, random realization, $n_i(x)$, given by the red curve. Figs. 4.5(a-c) show the 2D wavevector spectra of Figs. 4.4(a-c). For comparison, we show the experimental results on the rightmost panel of Figs. 4.4, 4.5.

For all three number variances, the structure of the density variations near the BH horizon, the checkerboard patterns in the right half of the cavity, and their spectra in simulation and experiment agree fairly well with the experiment. The discrepancy, as discussed in the previous subsection, concerns the relative sizes of the peaks. The smeared lines parallel to the diagonal in the correlation function match

the experiment better in the $\Delta N/\bar{N} = 0.1, 0.15$ cases. The overall experimental density profile $n(x)$ decreases sharply from the BH horizon to the WH horizon, a behavior that is best matched for $\Delta N = 0.15\bar{N}$.

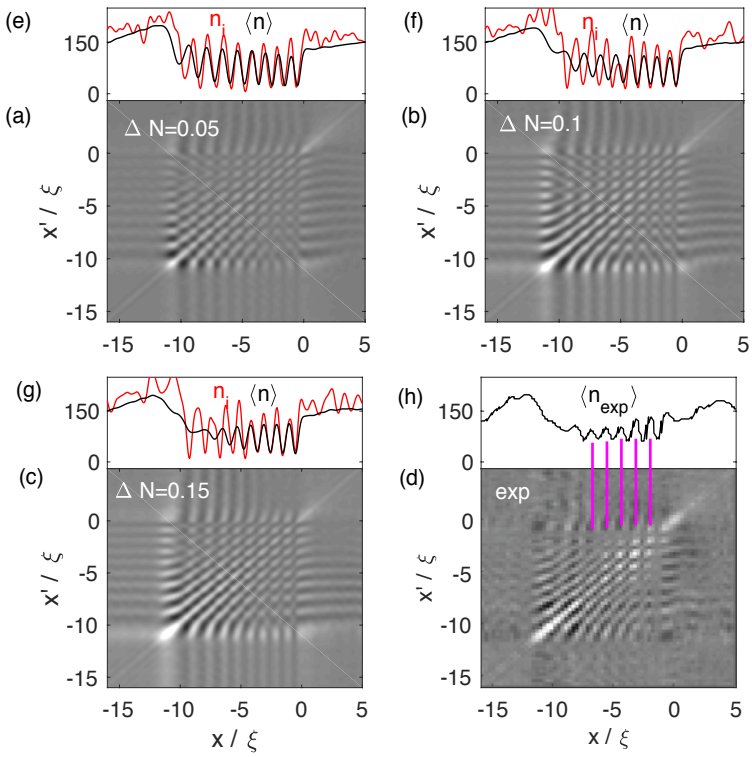

Figure 4.4: The density-density correlations by both number and quantum fluctuations. For panels (a-c), the number of condensate atoms fluctuates about $\Delta N/\bar{N} = 0.05, 0.1, 0.15$, respectively. Panel (d): experimental density-density correlation taken from [1]. Top panels (e-g) are the profiles of the averaged density $\langle n(x)\rangle$ (black) and that of one realization in the corresponding ensemble , $n_i(x)$ (red). Panel (h) is the ensemble average of experimental density, $\langle n_{\rm exp}\rangle$, taken from [1].

4.2.3 Influence of atom number and quantum fluctuations on standing wave and correlation

In this subsection we suggest some mechanisms for the effect of number and quantum fluctuations on the standing wave and correlation function, and we briefly

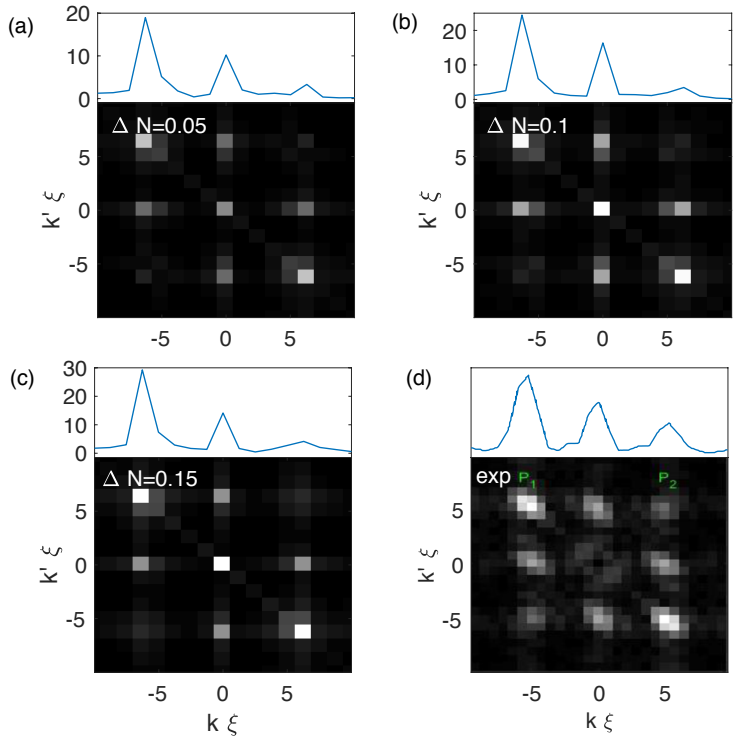

Figure 4.5: 2D wavevector spectra for the correlations in Figs. 4.4. Panels (a-c): $\Delta N/\bar{N} = 0.05, 0.1, 0.15$, respectively. Bottom: 2D wavevector spectrum; top: cut-through of the 2D spectrum at $k'\xi = 6$. Panel (d): 2D wavevector spectrum of the experimental correlation taken from [2]; upper panel is its cut-through along P_1 and P_2.

consider also some other simulations described in the literature. As a preliminary comment, we found that very small modifications of the strength of the trap potential can have a relatively large effect on certain details in the evolution of the condensate. This sensitivity to the potential is demonstrated in Appendix B.1, where it is shown that a 3% variation in the overall coefficient of the (one-dimensional) trap leads to measurable differences.

Atom number fluctuations influence both the amplitude of the background flow, and the amplitude and phase of the cavity standing wave. Fig. 4.6(a) shows the density variation, $\delta n = n - \langle n \rangle$ (where $\langle n \rangle$ is the average density for the en-

semble with standard deviation $\Delta N = 0.05\bar{N}$) as a function of position and atom number variation δN. The correlation function is the product of the density variations $\delta n(x)\delta n(x')$, averaged over the different number values in the normal distribution, with 68% weight from $|\delta N|/\bar{N} < 0.05$, and another 27% weight from $0.05 < |\delta N|/\bar{N} < 0.1$, and only 5% from outside the region of the plot. The phase varies with N more in the left half of the cavity, closer to the WH, but also varies on the right half. However in the right half of the cavity, near the BH, the response to number fluctuations is markedly weaker, and asymmetric, being stronger for negative fluctuations than for positive ones. Therefore in that region the correlation function is more influenced by negative number fluctuations.

The plot in Fig. 4.6(b) shows the average density (dashed black curve, $\langle n \rangle$) together with two realizations from the ensemble: one with $\delta N = 0.075\bar{N}$ (red curve, $n_{\max}$), and one with $\delta N = -0.075\bar{N}$ (blue curve, $n_{\min}$). Compared to $\langle n \rangle$, the amplitudes of $n_{\max}$ and $n_{\min}$ are above and below, respectively, and for $n_{\max}$ the left edge of the cavity shifts towards the right, while for $n_{\min}$ it shifts towards the left. The density variation $\delta n = n_{\min} - \langle n \rangle$ is shown in Fig. 4.6(c). It has a wavelength similar to that of the density itself, and its wavevector spectrum, shown in Fig. 4.6(d), has peaks close to those of the average density spectrum shown in Fig. 4.1(c). The contribution from zero wavenumber corresponds to the overall modulation of the total number of atoms, which can be seen in the single realizations in position space shown in Fig. 4.6(b). The variation δN thus modulates the overall condensate density, and it also changes the location of the WH horizon, and thus modulates the phase of the standing wave at a given location.

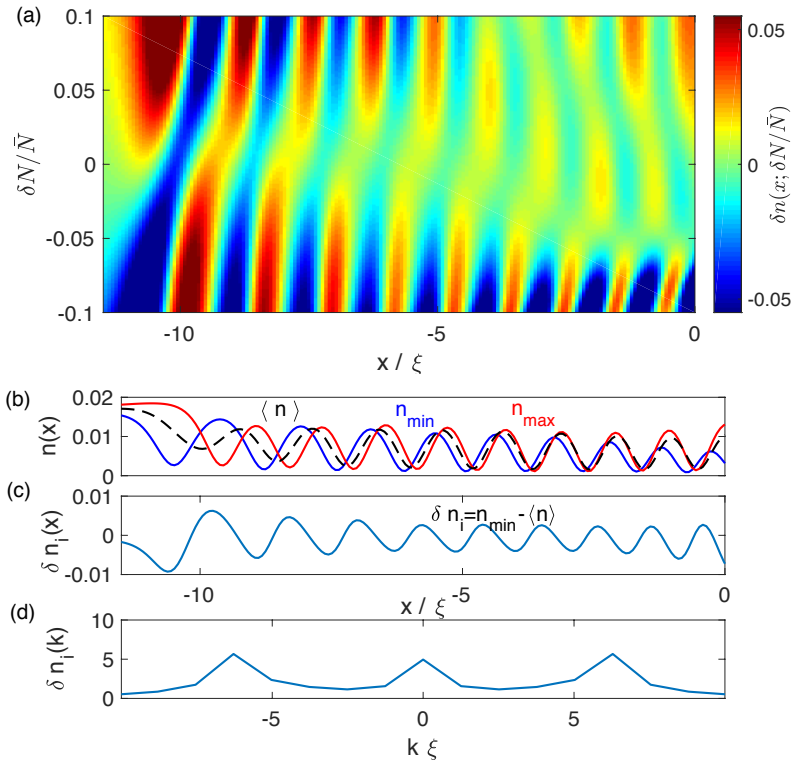

Figure 4.6: Effects of atom-number variation on the standing wave. (a) density variation, $\delta n = n - \langle n \rangle$, as a function of position, for atom number $N = \bar{N} + \delta N$. (b) dashed black: averaged density over atom-number fluctuation, $\Delta N/\bar{N} = 0.05$; solid red: density of a realization with atom number $N = \bar{N} + 0.075\bar{N}$, $n_{\max}$; solid blue: one with atom number $N = \bar{N} - 0.075\bar{N}$, $n_{\min}$. (c) difference between the density with $N_{\min}$ and the averaged density, $\delta n = n_{\min} - \langle n \rangle$. (d) wavevector spectrum for $\delta n(x)$ in a region near the BH, $-11\mu\text{m} < x < -1\mu\text{m}$.

Atom number fluctuations therefore result in a fluctuating δn, with a characteristic wavenumber equal to that of the standing wave, as well as a background ($k = 0$) component, and hence a nonzero correlation function $\langle \delta n(x) \delta n(x') \rangle$ with that same wavenumber. The pattern that emerges is different in the right and left halves of the cavity, because of the differences in the intensity of the variation and the shifting of the phase of the oscillation. On the left half of the cavity, the phase fluctuates more, hence the correlation function is smeared out to be relatively constant on diagonal lines of constant $x' - x$, as seen in the correlation function with

number fluctuations, Fig. 4.2(a), and observed in the experiment Fig. 4.2(d). On the right half, there is little density variation except for the larger negative number variations, so a fairly constant phase contributes, and the resulting correlation function is therefore similar to the plot of $n(x)n(x')$ shown in Fig. 4.1(b), which is similar to the checkerboard pattern seen in the figures just mentioned. Note that this "checkerboard" differs from an ordinary checkerboard pattern, in that there are wide dark nodes, rather than an alternating pattern of adjacent light and dark squares. The $k = 0$ component of δn is essential for the occurrence of these dark nodes. Without it, the correlation function would be something like $\cos kx \cos kx'$, whereas with it the correlation function is more like $(A + \cos kx)(A + \cos kx')$, where A is a constant.

Quantum fluctuations alone also produce a correlation function. Fig. 4.2(f) shows the background standing wave in the cavity, with the addition of fluctuating spatial noise. The standing-wave amplitude for each run varies slightly from the average profile, while the phase is less affected than for number fluctuations, since the zero-point field does not change the overall flow structure. Such variation results in a faint checkerboard, seen in Fig. 4.2(b), and its wavevector spectrum in Fig. 4.3(b) shows peaks at the same values as produced by number fluctuations but weaker, and with off-diagonal ($k' = -k$) contribution much larger than the other contributions. The checkerboard feature of this correlation function, including the dark nodal lines, might arise as follows: the GP wavefunction has the form $\Psi(x,t) = \Psi_0(x,t) + \delta\psi(x,t)$, where $\Psi_0(x,t)$ is the wavefunction without the quantum noise having been added at $t = 0$. The dominant contribution to the

density-density correlation function will come from the cross terms in the density $n(x) = \Psi^\dagger(x)\Psi(x)$ between Ψ_0 and $\delta\psi$. The components of $\delta\psi$ with wavelength long compared with that of the standing wave thus modulate the amplitude of the background and standing wave in Ψ_0, in a spatially correlated fashion. We check this interpretation by simulating the quantum noise from only the short wavelength modes, and the resulting correlation does not have the checkerboard pattern.

4.2.3.1 Comparison with other simulated results

Correlation functions similar to Fig. 4.2 are simulated and reported in Refs. [2, 46]. These simulations include some sort of noise as a proxy for the effect of quantum fluctuations (local Gaussian noise in the case of [46], and noise induced by a short pulse Bragg technique in the case of [2]). The effect of fluctuations in the WH horizon location induced by fluctuations in the step potential were also explored in [46].

Fig. 5(a) of Ref. [46] and Fig. 4(c) of Ref. [2] show a similar checkerboard pattern, which alternates between black and white in the region near the BH. This is somewhat consistent with our TWA simulation, regarding the black-white-alternating feature; however, for our QF simulations, the dark nodes (discussed above in this subsection), while not so distinct as in the NF case, are more evident. This difference is also manifested in the Fourier transform, which has more power at $k = 0$ in our simulation.

Fig. 5(b) of Ref. [46] shows the correlation function for the ensemble with fluc-

tuations in the step potential, and therefore fluctuations in the position of the WH horizon. This correlation function displays diagonal streaks, consistent with what one expects when the phase of the standing wave is fluctuating within the ensemble, across the entire cavity between the WH and BH horizons. This is similar to the pattern we have seen induced by number fluctuations on the WH side of the cavity, but not on the BH side. It should also be noted that the step potential fluctuations introduced in [46] were more than two orders of magnitude larger than in the experiment [2], whereas the number fluctuations we have introduced are comparable to those encountered in BEC experiments. Ref. [46] also mentions finding that atom number fluctuations have no significant effect on observables, and in particular do not change the position of the WH horizon. As discussed in Appendix B.1, we found that the condensate is more affected by number fluctuations for a shallower trap. This might explain why Ref. [46] found no significant effect of number fluctuations, as the trap potential shown in their Fig. 1 appears to be steeper than the one we used.

In sum, while the noise added in the simulations of Refs. [2, 46] does have the effect of eliciting correlation functions that reflect the structure of the background standing wave, the correlation function we obtain combining number fluctuations and quantum fluctuations via the TWA is significantly closer to the experimentally observed one.

4.3 Conclusion

We have found that atom number fluctuations play a dominant role in giving rise to density-density correlations in a BEC with a background density wave structure. This, together with a similar contribution from quantum fluctuations, appear to account for all features of the checkerboard correlation pattern observed in the BH/WH cavity in the experiment of [1].

In Ref. [34] we modeled this experiment using the GP equation without any fluctuations, and found that the standing wave is zero frequency Bogoliubov-Čerenkov radiation (BCR), originating at the WH horizon where the flow transitions from supersonic to subsonic. This frequency is Doppler shifted to a nonzero value in the reference frame of the BH horizon (because the WH horizon is receding from the BH horizon), where it stimulates Hawking radiation at that frequency. We found no sign of the black hole laser instability [14, 19] that can in principle take place in this configuration, and inferred that the observed phenomena are driven by the BCR alone. However, since our previous analysis did not include any fluctuations, it was unable to produce the observed correlation function, and was unable to demonstrate explicitly that the addition of quantum fluctuations does not trigger the laser instability (although the condensate in the cavity is sufficiently inhomogeneous and time-dependent to expect that if the instability could occur on the timescale of the experiment, it would have manifested in our previous GP simulations).

The present chapter demonstrates that the correlation function, too, can be explained based on nothing more than the BCR and fluctuations, and that the quan-

tum fluctuations do not seed a laser instability on the time scale of the experiment. Although the details depend on the types of fluctuations, and small variations of trap and step potentials, the main checkerboard pattern is a robust feature, with a spectrum consistent with that of the background BCR. That is, quantum fluctuations, and number fluctuations only modify a pattern that is already established by the BCR standing wave.

Finally, the possibility that the correlation function observed in other BEC experiments may be strongly affected by number fluctuations deserves to be investigated. In the future, for an experiment where it is important to suppress atom number fluctuations, they might be reduced below the $1/\sqrt{N}$ shot noise level using recently developed experimental techniques [47].

Chapter 5: Resonant phonon wavepackets on a ring-shaped Bose-Einstein condensate

In this chapter, we study the excitations in a ring BEC, driven harmonically by a potential barrier localized in a small region of the ring. The content of this chapter is taken from a published work [48], in collaboration with A. Kumar, F. Jendrzejewski, Ryan M. Wilson, Mark Edwards, S. Eckel, G. K. Campbell, and Charles W. Clark.

As introduced in Chapter 1, phonon wavepackets can be created by applying the potential barrier in the ring condensate. Modulating periodically the amplitude and position of the barrier, we find a number of resonant frequencies at which the driven condensate exhibits recurrent wavepacket trains traveling at the speed of sound. The resonant frequencies are multiples of the orbital frequencies of the wavepackets, which are easily calculated from the speed of sound and the symmetry of the driving potential. We construct a simple model of the resonant wavepackets that seems to have wide applicability. The resonant wavepackets persist over many cycles of the driven oscillation. For sufficiently long excitation times, atoms eventually acquire enough energy to escape from the trap. We find that atom loss from the trap is strongly enhanced at the resonant frequencies, and that it is well

described by solutions of the time-dependent GPE. This suggests that our atom loss is dominated by the effects of mode-coupling that are known to exist in the strongly driven GPE [49–52]. For strong conditions of excitation, we observe wavepackets that move faster than the speed of sound. These resemble the shock waves that have been seen in previous studies [53, 54]. In this system we also observe the collision of two shock waves.

This chapter is organized as follows. Sec. 5.1 presents an intuitive picture of the dynamics of harmonically driven ring BECs in terms of phonon wavepackets. Sec. 5.2 describes the details of our experimental setup. In Sec. 5.3, we model the condensate dynamics with the GPE and the condensate's elementary excitations with the Bogoliubov-de Gennes equations. Sec. 5.4 shows that appropriate modulations of the potential barrier can be used for controlled excitation of resonant wavepackets. We present evidence for the generation of supersonic shock waves and collisions of two shock wavepackets in Sec. 5.5.

5.1 A simple model of resonant wavepacket generation by an oscillating weak link

In a Bose-Einstein condensate, phonon wavepackets can be constructed by forming a superposition of low-lying Bogoliubov excitations (see Sec. 5.3 for details). If a localized weak perturbation with a typical length scale w is suddenly applied to the condensate [55], it will generate a wavepacket consisting of phonon modes with wavelengths less than w. These wavepackets will travel away from the perturbation

at the speed of sound without dispersion. Stronger perturbations can generate a variety of nonlinear wave motions [56], including supersonic shock waves that are discussed in Sec. 5.5.

In a ring condensate, one can create wavepackets that travel around the ring. The orbital period, T, of a single wavepacket establishes a characteristic frequency, $\nu = 1/T = c/(2\pi R)$, where c is the speed of sound in the BEC and R is the radius of the ring. If the localized weak perturbation is modulated periodically, resonances may occur when the perturbation consistently adds energy to the wavepacket over each cycle of its motion, as is the case in cyclotron and synchrotron particle accelerators [57]. Two classes of such resonances, associated with amplitude- and position-modulation of a weak link, have been seen in our experiment. This section presents a simple model for understanding them.

Consider first the case where the perturbation is a symmetric potential barrier at a fixed location in the ring, with the barrier height driven sinusoidally around a positive value. This amplitude-modulation case is shown schematically in Fig. 5.1. Here, the widths of the gray-shaded regions at $\phi = 0$ and 2π denote the height of the barrier as a function of time. As the height increases, the barrier displaces the BEC, generating a symmetric pair of wavepackets. Traveling in opposite directions around the ring, the wavepackets return to the barrier at time T. If the barrier is rising when they return, energy will be added to the wavepackets as they begin their next journey around the ring. The resonance condition in this case corresponds to the frequency of the barrier oscillation being an integer multiple of ν, i.e., $\nu_q = q\nu$, where q is an integer. Panels (c) and (d) of Fig. 5.1 depict this resonant case with

$q = 1$ and 2, respectively. On the other hand, if the barrier is falling when the wavepackets arrive, they will lose energy. This non-resonant case corresponds to $\nu_q = q\nu$, where q is now a half-integer. Panels (a) and (b) of Fig. 5.1 show this non-resonant case with $q = 1/2$ and $3/2$, respectively.

When the counterpropagating wavepackets overlap, they create a localized region of high density. The alternation of regions of high and low densities follows a pattern analogous to a standing wave, which is shown by the dashed and solid blue curves to the right of each panel. For panels (c) and (d), this standing density wave propagates like $\cos(q\phi)\sin(2\pi\nu_q t)$. Since their wavefunctions resemble the eigenfunctions of a particle on a ring, we denote these modes as 'ring modes'. For the nonresonant conditions shown in panels (a) and (b), the density wave propagates like $\sin(q\phi)\sin(2\pi\nu_q t)$. Given their similarity to the eigenfunctions of a particle in a box potential, we denote them as 'box modes'. For amplitude-modulation excitation, the ring modes are resonant and the box modes are nonresonant.

We now consider position-modulation excitation, in which the shape of the barrier remains constant, but its azimuthal position in the ring oscillates in time. In this case, a wavepacket is created by the barrier pushing atoms in front of it during the fastest part of its motion. The wavepacket then orbits the ring with period T. On its return, if the wavepacket encounters the barrier moving opposite to its direction of travel, it will be reflected from the barrier with a momentum kick. Therefore, the resonance condition in the position-modulation case corresponds to the frequency of wavepacket oscillation being a half-integer multiple of ν, i.e. $\nu_q = q\nu$ with $q = 1/2$, $3/2$, etc. Fig. 5.2 shows the wavepacket propagation for position-modulation, in

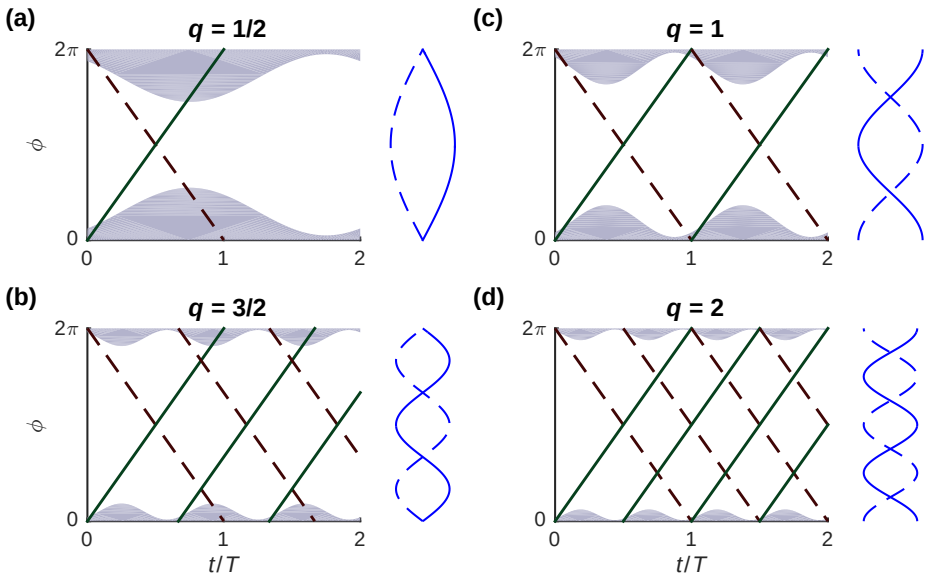

Figure 5.1: Trajectories of wavepackets in a ring driven by a barrier whose height oscillates with frequency $\nu_q = q\nu$: (a) $q = 1/2$; (b) $q = 3/2$; (c) $q = 1$; (d) $q = 2$. The grey shaded areas represent the barrier height as a function of time, t, and the solid (green) and dashed (black) lines indicate the ring azimuthal coordinates, ϕ, of the centers of the wavepackets. The blue lines show the standing-wave-like density modulation created by the overlapping wavepackets.

a manner similar to Fig. 5.1. Panels (a-d) correspond to $q = 1/2$, 1, 3/2, and 2, respectively. The corresponding standing waves are shown on the right of each panel. For position-modulation excitation, the box modes are resonant and the ring modes are nonresonant.

The above argument for the resonance condition of a position-modulated barrier is valid only if the wavepacket is predominantly reflected from the barrier. If, on the other hand, the wavepacket were predominantly transmitted, the barrier would only add energy to the wavepacket if it were traveling in the same direction as the wavepacket. In this case, the resonance condition would again correspond to the oscillation frequency being an integer multiple of ν. (In this case, the ring modes would be again resonant.) Whether the wavepacket is transmitted or reflected de-

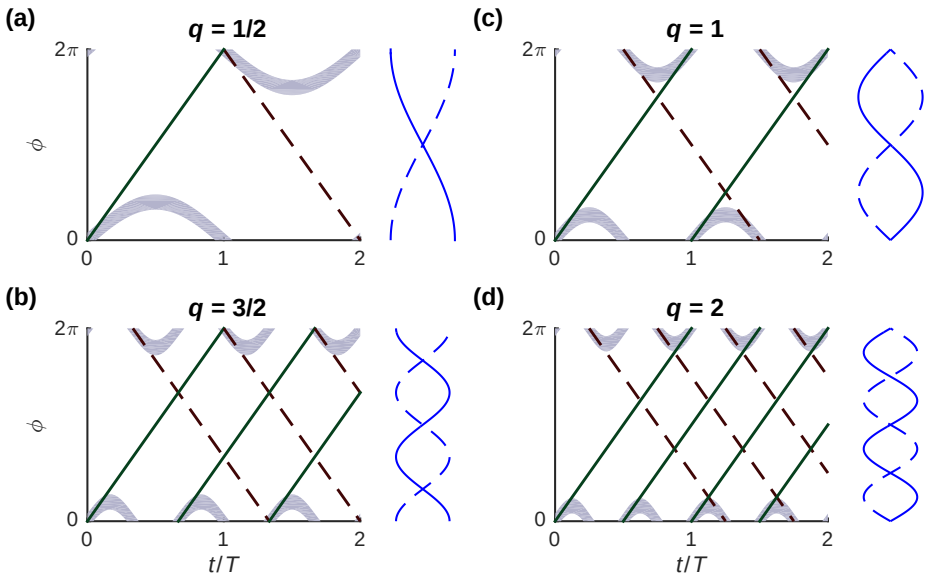

Figure 5.2: Trajectories of wavepackets in a ring driven by a barrier whose position oscillates with frequency $\nu_q = q\nu$: (a) $q = 1/2$; (b) $q = 3/2$; (c) $q = 1$; (d) $q = 2$. The grey shaded areas represent the barrier position as a function of time, t, and the solid (green) and dashed (black) lines indicate the azimuthal coordinate, ϕ, of the centers of the wavepackets. The blue lines show the standing-wave-like density modulation created by the overlapping wavepackets.

pends on the change in the speed of sound in the barrier region. If the barrier is strong compared to the chemical potential, the density will be depleted, and the speed of sound would be reduced. In analogy to optics, the change in the index of refraction going from the ring to the barrier would be large, consequently causing a large reflectivity. If the barrier is weak compared to the chemical potential, the index of refraction change would be small, minimizing the amount of reflection. Thus, one should expect a change in the resonance condition for a position-modulated barrier: as the strength of the barrier potential is increased, the resonance should shift from integer to half-integer values of q.

5.2 Experimental Parameters

The BEC is formed in a crossed optical dipole trap with the same procedures as in Ref. [58]. The trap is created by two laser beams: a red-detuned laser beam shaped like a sheet for the vertical confinement and a blue-detuned laser beam transmitting through an intensity mask [59]. The intensity mask is imaged onto the atoms, providing in-plane confinement. Laser-cooled ^{23}Na atoms in the $|F = 1, M_F = -1\rangle$ state are condensed into the trap after forced evaporation.

The intensity mask forms a "target"-shaped trap [58], which has both a toroidal (ring) and a concentric disc trap. The resulting condensate in the ring has a mean radius of 22(1) μm and a Thomas-Fermi full-width of ≈ 8 μm. (All uncertainties are the uncorrelated combination of 1σ statistical and systematic uncertainties unless stated otherwise.) The disc-shaped condensate, which is left unperturbed during the experiment, serves as a reference to check atom number stability. The vertical trapping frequency is $\omega_z/2\pi = 542(13)$ Hz while the radial trapping frequency of the ring is $\omega_\rho/2\pi = 400(20)$ Hz. The average number of atoms in the target trap is $\approx 7 \times 10^5$, with ≈ 80 % of atoms in the toroid and ≈ 20 % in the central disk. On any individual repetition of the experiment, the atom number can fluctuate from its mean by up to 10 % (2σ). We measure the atomic density using *in-situ* partial transfer absorption imaging [60].

We create the weak link potential by using a focused, blue-detuned Gaussian beam. The $1/e^2$ full-width of the Gaussian is ≈ 5 μm. This beam generates a repulsive potential that depletes the condensate density locally in the region of the

beam. An acousto-optic deflector (AOD) controls the position of the beam. By changing the power applied to the AOD, we can control the intensity of the beam. To create a radially-elongated weak link, the AOD scans the beam rapidly in the radial direction at 2 kHz. The resulting time-averaged potential is a wide, flat potential barrier with an effective width of ≈ 15 μm.

For the experiments here, we manipulate the weak link in a variety of different ways. For the experiments described in Sec.5.4, the weak link is first applied adiabatically to the BEC, so as to not generate excitations. The weak link beam's intensity is ramped on linearly over 300 ms. During this linear ramp, the azimuthal position of the weak link is fixed. After the intensity reaches its final value, the weak link position is oscillated in the azimuthal direction, or its intensity is modulated as a function of time. For the experiments described in Sec. 5.5, the weak link beam is turned on suddenly while it remains in a fixed azimuthal position. The response time of the AOD and the servo that controls the intensity of the beam limits the rise time of the weak link to approximately 100 μs.

5.3 BdG description of elementary excitations of a BEC

Dilute Bose-Einstein condensates, like the one we study here, are often [32,61] described by a mean-field theory with an order parameter $\Psi_0 = \langle\hat{\Psi}\rangle$, where $\hat{\Psi}$ is the quantum field operator, which can be expanded as

$$\hat{\Psi} \;=\; \Psi_0 + \delta\hat{\Psi}. \tag{5.1}$$

Here, $\delta\hat{\Psi}$ denotes the field operator for the non-condensate atoms: it describes the elementary excitations of the condensate in the linear-response regime. The order parameter Ψ_0 can be interpreted physically as the condensate wave function, which is macroscopically occupied. The dynamics of the condensate wave function are described by the time-dependent Gross-Pitaevskii equation (TDGPE),

$$i\hbar\frac{\partial}{\partial t}\Psi_0(\mathbf{r},t) = \left[-\frac{\hbar^2}{2M}\nabla^2 + V(\mathbf{r}) + g\left|\Psi_0(\mathbf{r})\right|^2\right]\Psi_0(\mathbf{r}), \tag{5.2}$$

where $V(\mathbf{r})$ is the external potential, M is the atomic mass, and g quantifies the interaction strength between the atoms, and is given by $g = 4\pi\hbar^2 a/M$, where a is the s-wave scattering length associated with binary atomic collisions. The stationary, ground state solution of the GPE can be expressed as

$$\Psi_0(\mathbf{r},t) = \sqrt{n(\mathbf{r})}e^{-i\mu t/\hbar} \tag{5.3}$$

where $n(\mathbf{r})$ is the condensate density, and μ is the chemical potential of the system.

Elementary excitations are those for which the number of excited atoms is much smaller than the number of atoms in the BEC. The field operator for the excited atoms then satisfies the linearized equation of motion,

$$i\hbar\frac{\partial}{\partial t}\delta\hat{\Psi}(\mathbf{r},t) = \left[-\frac{\hbar^2}{2M}\nabla^2 + V(\mathbf{r}) + 2gn(\mathbf{r}) - \mu\right]\delta\hat{\Psi}(\mathbf{r},t) + g\Psi_0^2\delta\hat{\Psi}^\dagger. \tag{5.4}$$

We solve this equation in a Bogoliubov-de Gennes framework [32, 61], and expand $\delta\hat{\Psi}$ in the Bogoliubov operators a_i and $a_i^\dagger$,

$$\delta\hat{\Psi} = \sum_i \left(u_i e^{-i\omega_i t}a_i + v_i^* e^{i\omega_i t}a_i^\dagger\right), \tag{5.5}$$

where ω_i are the elementary excitation frequencies and u_i, v_i are the Bogoliubov amplitudes of the i^{th} excitation. These amplitudes satisfy the Bogoliubov-de Gennes

(BdG) equations:

$$\begin{aligned}\left[\hbar\omega_i + \frac{\hbar^2}{2M}\nabla^2 - V(\mathbf{r}) - 2gn(\mathbf{r}) + \mu\right] u_i(\mathbf{r}) &= gn(\mathbf{r})v_i(\mathbf{r}) \\ \left[-\hbar\omega_i + \frac{\hbar^2}{2M}\nabla^2 - V(\mathbf{r}) - 2gn(\mathbf{r}) + \mu\right] v_i(\mathbf{r}) &= gn(\mathbf{r})u_i(\mathbf{r}).\end{aligned} \tag{5.6}$$

We numerically diagonalize Eqs. 5.6 to find the spectrum of elementary excitations for the condensate, as shown in Fig. 5.3.

In a spatially uniform condensate ($V(\mathbf{r}) = 0$), Eq. (5.6) has plane-wave solutions [32], $u_\mathbf{k}(\mathbf{r}) = u_\mathbf{k} e^{i\mathbf{k}\cdot\mathbf{r}}$ and $v_\mathbf{k}(\mathbf{r}) = v_\mathbf{k} e^{i\mathbf{k}\cdot\mathbf{r}}$, where $\mathbf{k}$ denotes the wave vector, and a continuous spectrum of elementary excitations,

$$\hbar\omega_\mathbf{k} = \sqrt{\epsilon_\mathbf{k}^2 + 2\epsilon_\mathbf{k} gn}, \tag{5.7}$$

where $\epsilon_\mathbf{k} = \hbar^2 k^2/2M$ is the kinetic energy of a free quantum particle of mass M. For small k, the frequencies $\omega_\mathbf{k}$ are linear in k, i.e. $\omega_\mathbf{k} \approx k\sqrt{gn/M}$. Since this dispersion relation is the same as that for a sound wave, $\omega = ck$, these excitations, or quasiparticles, can be viewed as phonons, and the proportionality constant determines the speed of sound, $c = \sqrt{gn/M}$.

In our experiments, we do not deal with a homogeneous BEC, but one confined to a ring trap. The trap's potential has the form

$$V(\mathbf{r}) = \frac{1}{2}M\omega_z^2 z^2 + V_G\left(1 - e^{-2(\rho-R)^2/w_\rho^2}\right), \tag{5.8}$$

where the first term is a harmonic potential in the axial (z) direction with frequency $\nu_z = 542$ Hz, and the second term represents the ring potential, with: depth $V_G = 266\text{nK} \times k$, where k is the Boltzmann constant; ring radius $R = 22.4$ μm; and $1/e^2$ half-width $w_\rho = 5.5$ μm. (These parameter values best reproduce the experiment

as described in Sec. 5.2.) In this trap, the low-momentum quasiparticles obey a *quantized* dispersion relation analogous to that of the homogeneous system given by Eq. 5.7. We now describe this correspondence.

In the absence of a weak link, the potential and the ground state of the BEC have cylindrical symmetry about the z axis. The Bogoliubov quasi-particle amplitudes thus have sharp values of the projection of the angular momentum operator $\hat{l}_z = \hat{x}\hat{p}_y - \hat{y}\hat{p}_x$, and thus have the azimuthal dependence of the form $\sim e^{im\phi}$, where $\phi = \arctan(y/x)$ is the conventional azimuthal angle of a two-dimensional coordinate system and m is an integer. Our lowest energy solutions to Eqs. (5.6) scale like $\omega_m \sim m\sqrt{g\bar{n}/MR^2}$, where $\bar{n}$ is the mean condensate density and R is the radius of the ring [62]. These solutions form a manifold of discrete phonon-like modes that propagate azimuthally with the characteristic speed of sound of the ring condensate,

$$c = \sqrt{g\bar{n}/M}. \tag{5.9}$$

Fig. 5.3 shows the calculated the energy spectrum of elementary excitations by solving the BdG equations. For small m, the modes for the lowest branch are nodeless in the radial and axial (z) directions [63]. The linear dependence at small m is clear. Using the experimental parameters of Sec. 5.2, our linear fit at small m provides an orbital frequency for sound of $\nu = 37.9(2)$ Hz. Note the avoided crossing between the lowest two branches around $m = 17$, which is due to the near degeneracy of angular and radial excitation there. In a manner characteristic of two-level crossing systems [64], the predominantly angular modes continue on the second branch for $m > 20$, where they show roughly the same linear dispersion

relation.

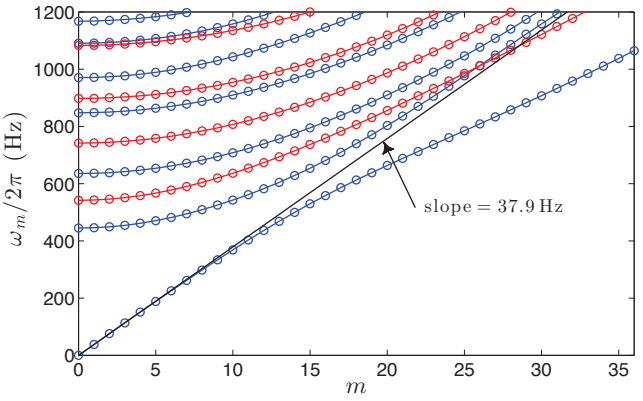

Figure 5.3: The BdG spectrum for the elementary excitations of a ring condensate. The blue (red) curves correspond to the excitation modes that are even (odd) in the axial (z) direction. The lowest branch represents the excitations in the azimuthal direction, the frequency of which is linear at small m (denoted by the black line). The slope determines the orbital frequency of sound $\nu = 37.9(2)$ Hz.

We theoretically model the procedure described in Sec. 5.1 by propagating Eq. (5.2) in imaginary time to find the ground state condensate wave function $\Psi_0(\mathbf{r})$, then propagating in real time to model the dynamics. We implement the split-step Crank-Nicholson algorithm as in [65] on a Cartesian grid of dimensions $x \times y \times z = (100 \times 100 \times 10)$ μm. To generate various wavepacket trajectories, we generalize to a time-dependent potential $V(\mathbf{r}, t)$. This potential includes both the static potential (Eq. 5.8) and a potential for the weak link. This latter potential is repulsive and includes a Gaussian of $1/e^2$ half-width $w_L = 5$ μm along the azimuthal direction, and a rectangle of width $L = 15$ μm along the radial direction (see the supplemental material of Ref. [66]).

During the simulation, atoms can gain sufficient energy to escape from the trap. Such atoms are nonetheless bounded in the box, and can reflect at the bound-

aries and subsequently return to the ring trap. To eliminate this numerical effect, we implement absorbing layers at the edges of the xy-plane of the gridded box, by adding a damping term $H_{damp} = i\Gamma(x, y)$ in the Hamiltonian. We adopt the damping term that follows the form in [67], in which $\Gamma(x, y)$ slowly increases as x or y approach the box boundaries. In the x direction (equivalently for y), $\Gamma = V_d/\cosh^2(|x - x_d|/L_d)$, where the damping constant V_d is taken to be 0.01 μ, the absorbing layer width $L_d = 10$ μm, and $|x - x_{\rm d}|$ is the distance of a point in the absorbing layers from the nearest box boundary, x_d.

5.4 Driving and Probing the Excitations

Knowing the orbital frequency $\nu = 37.9$ Hz (Sec. 5.3), we now proceed to oscillate the barrier to find the resonant frequencies for wavepacket propagation (Sec. 5.1). This oscillation can take on two different forms. The first, shown schematically in Fig. 5.1, is the amplitude-modulation case discussed in Sec. 5.1. The barrier height is given by $V_b(t) = V_0 + V_a \sin(2\pi v_q t)$, where $V_0/\mu = 0.54(5)$ is the average amplitude of the barrier, $V_a = 0.95\, V_0$ is the amplitude of modulation, and $\nu_q = q\nu$ is the drive frequency. (The uncertainty in V_0 applies only to the experimental value.) The barrier is ramped up to V_0 in 10 ms at the beginning of each evolution. Fig. 5.4 shows the resulting time evolution of the condensate density for both the experiment (e) and the GPE simulations (a)-(d). At each time t, we integrate the condensate density along the radial and vertical directions to obtain an integrated 1D density $n_{1D}(\theta)$ along the azimuthal direction. The normalized density shown in

Fig. 5.4 is then obtained by dividing $n_{1D}(\theta)$ by $n_{1D,0}(\theta)$, the 1D density measured in a unperturbed ring without a weak link. In the experiment, the condensate density is not clearly periodic until several cycles of the oscillation have elapsed; therefore, we show data for later times $t \approx 15.5\,T$ to $t \approx 19\,T$. At these later times, atoms have already left the trap causing the measured normalized densities to tend to be less than unity. (For clarity, we scale the theoretical predictions to have the same range of normalized densities as the experiment.) Because the wavepackets in the $q = 1$ and $q = 2$ cases collide with the accelerating barrier, each oscillation cycle increases the energy of the wavepacket. Therefore, these ring modes are on resonance, as predicted in Sec. 5.1. The experimental data (Fig. 5.4e) shows the resonant $q = 1$ mode, which is consistent with the GPE simulation (Fig. 5.4c).

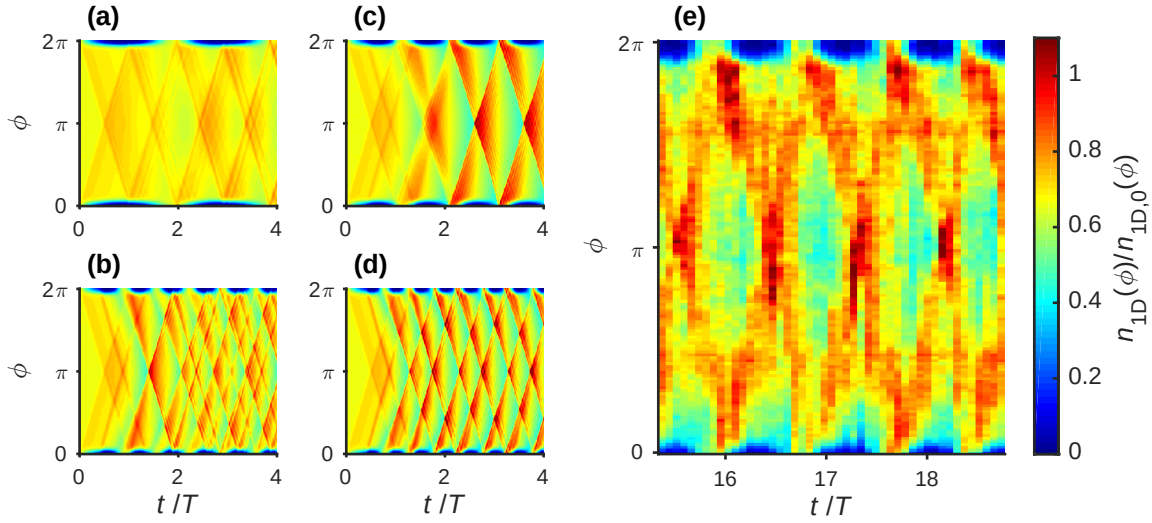

Figure 5.4: Time evolution of wavepackets generated through amplitude modulation of the barrier (see Fig. 5.1). The normalized 1D density (colorbar) shows wavepackets, or localized regions of high density, moving around the ring (azimuthal coordinate ϕ) with time t. The density also shows the barrier oscillating at $\phi = 0$ with frequency $\nu_q = q\nu$. Modes with $q = 1/2$ (a) and $q = 3/2$ (b) are nonresonant; modes with $q = 1$ (c and e) and $q = 2$ (d) are resonant.

The second oscillation scheme, shown schematically in Fig. 5.2, is the position-

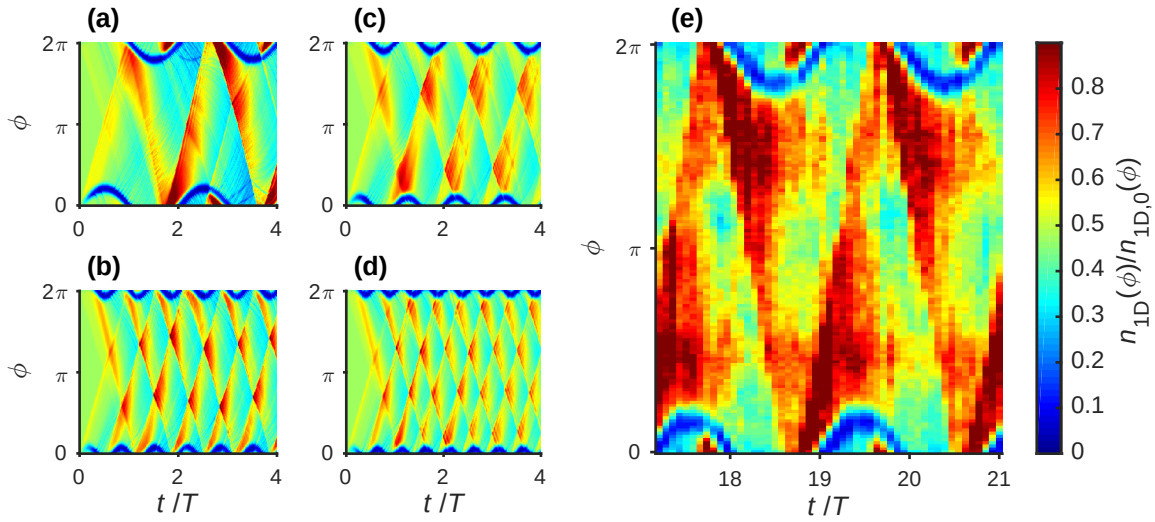

Figure 5.5: Time evolution of wavepackets generated though position modulation of the barrier (see Fig. 5.2). The normalized 1D density (colorbar) shows wavepackets, or localized regions of high density, moving around the ring (azimuthal coordinate ϕ) with time t. The density also shows the barrier oscillating about $\phi = 0$ with frequency $\nu_q = q\nu$. Modes with $q = 1/2$ (a and e) and $q = 3/2$ (b) are resonant; modes with $q = 1$ (c) and $q = 2$ (d) are nonresonant.

modulation case discussed in Sec. 5.1. Here, the position of the barrier is given by $\phi_b(t) = \phi_0 + \phi_a \sin(2\pi\nu_q t)$, where $\phi_0 = 0$ is the average position of the maximum height of the barrier, ϕ_a is the amplitude of modulation, and $\nu_q = q\nu$ is the drive frequency. The amplitude satisfies $\nu_q\phi_a = 80$ rad/s, which ensures the maximum velocity of the barrier is independent of ν_q. Fig. 5.5 shows the resulting time evolution of the density for both the GPE simulations (a-d) and the experiment (e). Here, the barrier, with height $V_0/\mu = 0.65(7)$, appears to be mostly reflective. As predicted in Sec. 5.1, the cases $q = 1/2$ and $q = 3/2$ (box modes) are on resonance. In particular, the wavepacket trajectories are synchronized with the barrier motion: a wavepacket generated by the barrier propagates around the ring and collides with the barrier while the barrier is moving in the direction opposite the wavepacket. By contrast, the cases $q = 1$ and $q = 2$ (ring modes) are off resonance: the wavepackets

collide with the barrier at a point in its oscillation when it is moving in the same direction.

Because the oscillating barrier can continually add energy to the condensate, atoms can acquire sufficient energy to escape the trap. If the oscillation is resonant, efficient energy transfer from the barrier will result in atom loss. Atom loss measured as a function of driving frequency will therefore show clear peaks at the resonant frequencies, ν_q. For both the experiment and the GPE simulation, we extract this atom-loss spectrum by oscillating the barrier for 2 s and then counting the remaining atoms in the trap, N_R. The fraction of atoms that remain is given by N_R/N, where N is the number of atoms measured when there is no oscillation.

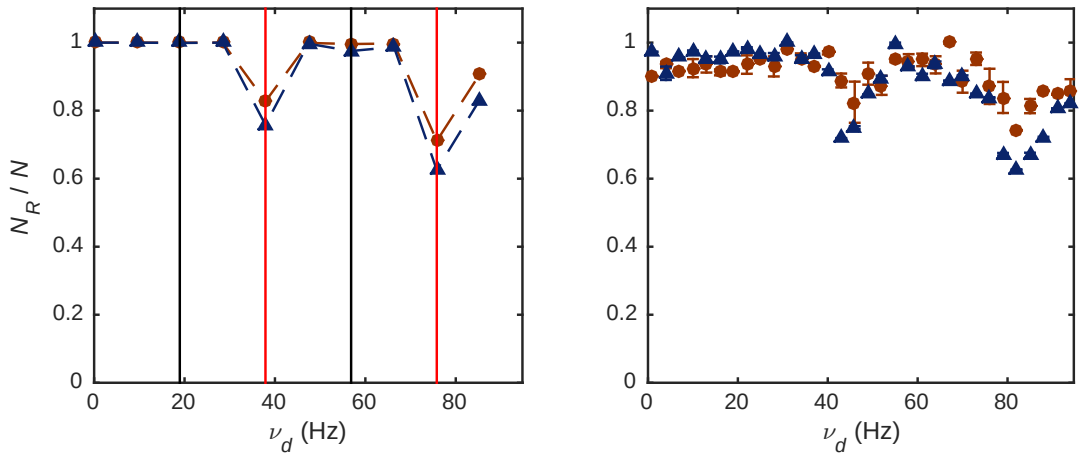

Figure 5.6: Simulated (left) and experimental (right) atom-loss spectra for an amplitude-modulated barrier with frequency ν_d and average heights $V_0/\mu = 0.30(2)$ (blue triangles) and $V_0/\mu = 0.50(4)$ (red circles). Here, N_R/N is the fraction of atoms that remain in the trap after 2 s of excitation. The vertical black (red) lines correspond to the resonant frequencies of the box (ring) modes. The dashed lines are a guide to the eye. The error bars in the experimental spectra correspond to the 1σ statistical uncertainty.

Fig. 5.6 shows the resulting atom-loss spectra obtained by amplitude modulation for two different barrier heights $V_0/\mu = 0.30(2)$ and $0.50(4)$. (Here, as before,

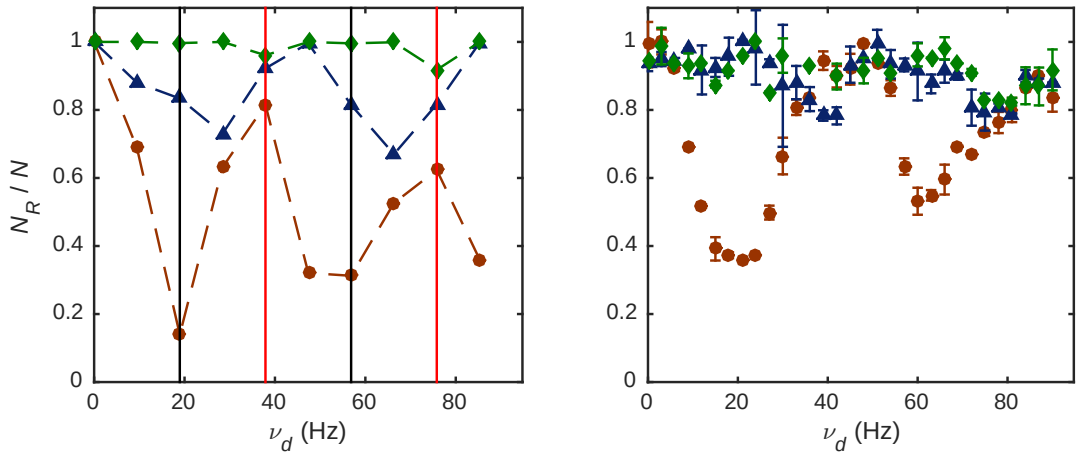

Figure 5.7: Simulated (left) and experimental (right) atom-loss spectra for a position-modulated barrier with frequency ν_d and heights $V_0/\mu = 0.15(1)$ (green diamonds), $V_0/\mu = 0.30(2)$ (blue triangles), and $V_0/\mu = 0.60(4)$ (red circles). Here, N_R/N is the fraction of atoms that remain in the trap after 2 s of excitation. The vertical black (red) lines correspond to the resonant frequencies of the box (ring) modes. The dashed lines are a guide to the eye. The error bars in the experimental spectra correspond to the 1σ statistical uncertainty.

the uncertainty applies only to the experiment.) In both cases, the oscillation amplitude is given by $V_a = 0.5V_0$. Both the experimental and simulated spectra show resonance peaks at drive frequencies corresponding to $q = 1$ and $q = 2$. As expected, these are the resonant frequencies of the ring modes (Fig. 5.1c-d and Fig. 5.4c-d). The location of the peaks in the experiment indicates $\nu \approx 41$ Hz, slightly larger than that predicted by theory. This small discrepancy may be due to uncertainty in atom number, trapping frequencies, or other experimental parameters.

Fig. 5.7 shows the atom loss spectra for position-modulation with barrier heights $V_0/\mu = 0.15(1)$, $0.3(2)$, $0.6(4)$. The displacement amplitude of the position modulation obeys $\nu\phi_a = 60$ rad/s. As V_0 is increased, both the experiment and the simulation show initial peaks at $q = 1$ and $q = 2$ that shift to $q = 1/2$ and $q = 3/2$. This corresponds to a transition from the ring modes being resonant to

the box modes being resonant. For small barrier heights, wavepackets are predominantly transmitted through the barrier. In this case, the ring modes are resonant, as these wavepackets receive more energy when they collide with a co-moving barrier (Fig. 5.2c and d). As the barrier height increases, wavepackets are more likely to be reflected. In this case, the box modes are on resonance, as these wavepackets receive more energy when they impinge on an oppositely moving barrier (Fig. 5.2a and b). This crossover from box-mode resonant behavior to ring-mode resonant behavior appears to occur near $V_0/\mu \approx 0.3$, as seen in Fig. 5.7. We note that in addition to the discrepancy in ν, the simulated spectra show more atom loss than the experiment.

The simulated spectrum with $V_0/\mu = 0.6$ also shows some possible broadening, as seen by the additional atom loss at nonresonant frequencies $\nu_d \approx 47$ Hz and 85 Hz. As atoms are lost from the condensate, the speed of sound and ν decrease, causing the broadening. As such, the broadening becomes evident only after $t \approx 1$ s of oscillation. Broadening in the opposite direction (toward larger ν) could also be present. In particular, driving the condensate with sufficient strength can generate supersonic shock waves rather than sound waves. In the next section, we directly create such dispersive shock waves and study their behavior.

5.5 Generation of supersonic shock waves

Theoretical analyses of the GPE predicted the existence of supersonic shock waves in BECs subject to large-amplitude disturbances [68–70]. Observations of such

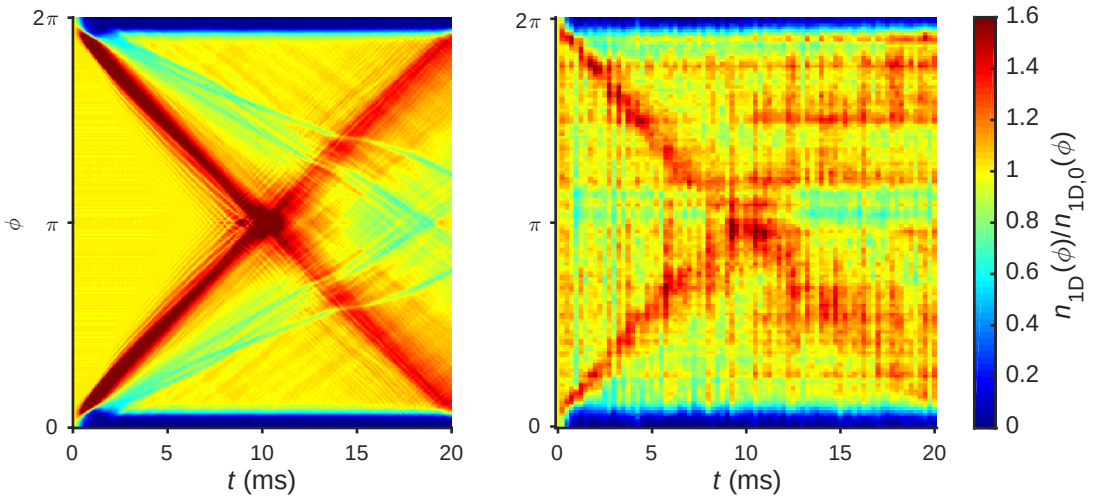

Figure 5.8: Supersonic flow in a shocked BEC. A condensate in our standard configuration is struck with an amplitude pulse that rises to its peak strength during an interval of 100 μs. Normalized density is shown vs. time. Left: solution of the time-dependent GPE; right: experiment.

waves in ^{87}Rb condensates were later reported in Refs. [53] and [54]. There is a substantial theoretical literature on supersonic phenomena in BECs (see refs. [56,71–78] and references therein), and a recent experiment reports the experimental observation of analogue Hawking radiation in a BEC [1]. We have also found evidence for supersonic shock waves, and our ring geometry makes it possible to observe collisions between them.

The left frame of Fig. 5.8 shows the solution of the TDGPE for our standard BEC configuration, subject to a sudden raising of the barrier during 100 μs. (Because there is no atom loss, we do not rescale the theoretical simulation in Fig. 5.8 as we did in Figs. 5.4 and 5.5.) This results in two counterpropagating high-density pulses - the left side of a red "X" - with orbital frequencies of $\nu \approx 50$ Hz, which is about 25 % greater than the orbital frequency of sound. These pulses collide near $\phi = \pi$, resulting in secondary excitations. However, the original shock pulses retain

much of their mass after the collision and continue to travel at the same speed. The shock waves generated in the experiment, which are shown in the right frame, exhibit significantly greater dispersion after the collision.

Also visible in the left frame of Fig. 5.8 are some secondary striations at densities $n \approx 1$, which all propagate with speeds corresponding to orbital frequencies $\nu \approx 34$ Hz. These features are consistent with sound waves. There are other structures at densities around $n \approx 0.6$, with orbital frequencies $\nu \approx 29$ Hz. Note that their speeds decrease during collisions with the shock waves, but are restored after the collision, a behavior characteristic of gray solitons. Both sound waves and solitons were reported in early experiments on large-amplitude excitations of Na and Rb condensates [79–81]. However, we do not see definitive signatures of them in the experimental data, which is shown in the right frame of Fig. 5.8.

5.6 Conclusion

We have investigated the excitations of a ring-shaped condensate with oscillatory amplitude- and position-modulated perturbations. This perturbation, in the form of a weak link, generates phonon wavepackets that travel around the ring at the speed of sound and therefore have an orbital angular frequency $\nu = c/(2\pi R)$. We find that the wavepackets are resonant with an amplitude-modulated perturbation if the perturbation's frequency is an integer multiple of ν. For position-modulation, the wavepackets are in resonance if the frequency of the perturbation is a half-integer multiple of ν. The difference in these cases corresponds to the symmetry

of the drive: an amplitude modulation creates two oppositely moving wavepackets at the same time, whereas position modulation creates two oppositely moving wavepackets at points in its motion that are out of phase by π. By looking at atom loss as a function of drive frequency, we verify these resonance conditions.

Chapter 6: Spinor Bose-Einstein condensates of Positronium

In this chapter, we study a spinor condensate of positronium and its self-annihilation. This chapter is based on a published work [82], in collaboration with Brandon Anderson and Charles Clark.

Positronium (Ps) is an element composed of one electron and one positron. Classically, it can be viewed as a pair of identical-mass particles, binding together with opposite charges, and orbiting about the center of mass, as shown in Fig. 6.1(a). A Ps atom undergoes self-annihilation and emits γ photons. This can be understood by a quantum picture shown in Fig. 6.1(b), where we show the probability distribution of Ps in its electronic ground state, similar to that of a hydrogen atom. The cusp at the center indicates the point of maximal probability, at which an electron and a positron meet and annihilate.

The Ps ground state has no orbital angular momentum, and has ^1S (para-positronium, para- or p-Ps) and ^3S (ortho-positronium, ortho- or o-Ps) components that are separated by an energy $\epsilon = 1.351 \times 10^{-22}$ J [25, 83]. The p-Ps state can decay by emitting two γ rays, and has a lifetime of $\tau_{\rm p} = 0.125$ ns; the o-Ps state must emit at least three γ rays, and has a lifetime of $\tau_{\rm o} = 0.142$ μs (see Fig. 6.1(c)).

The ideas of making a Ps BEC and its application in making a γ-ray laser are

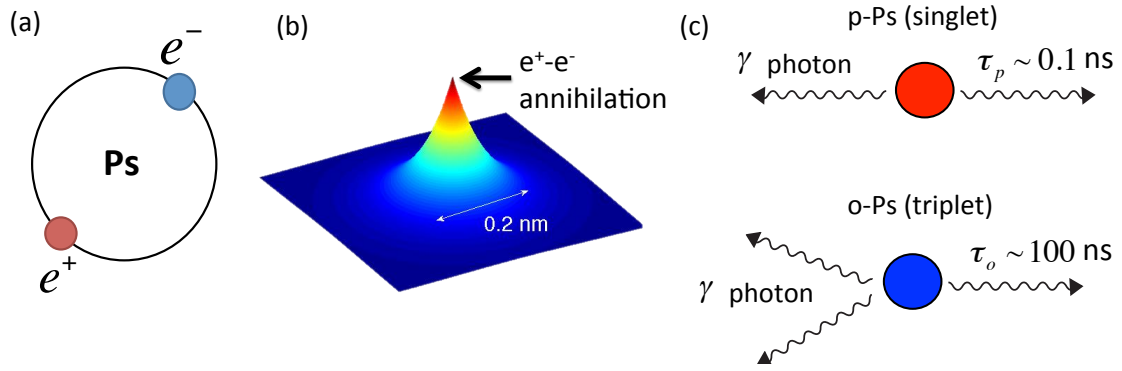

Figure 6.1: Illustrations of positronium (Ps) and its annihilation. Panel (a) classical picture of a Ps atom; panel (b) probability distribution of Ps in its ground state, $|\Psi(\mathbf{r})|^2 \sim e^{-2r/a_{\rm p}}$, where the ground-state radius $a_{\rm p}$ is twice the Bohr radius, ~ 0.1 nm; (c) top: p-Ps, decaying into 2 γ photons; bottom: o-Ps, decaying into 3 γ photons.

illustrated in Fig. 6.2, based on the proposal by Platzman and Mills [26, 27, 31]. In Fig. 6.2(a), it is shown that Ps atoms can be created and collected by impinging a dense, polarized positron pulse into a cavity within a piece of silicon. A fraction of the positrons will capture an electron in the silicon to yield Ps. The Ps atoms in the singlet state will quick decay due to its short lifespan, and a remaining portion of o-Ps will be collected and condensed in the cavity. It is estimated that at a temperature of 15 K, a BEC of o-Ps will be formed if the Ps density exceeds 10^{18} cm^{-3} [27]. By converting the long-lived o-Ps condensate to a p-Ps condensate with a magnetic field, strong γ-ray emission can be generated as the outcome of annihilation of p-Ps (see Fig. 6.2(b)).

There are some differences between Ps BEC and the BECs of alkali atoms. The mass of a Ps atom ($m = 2m_{\rm e}$) is much less than the mass of ordinary atoms, and thus Ps can be brought to Bose-Einstein condensation at much higher number

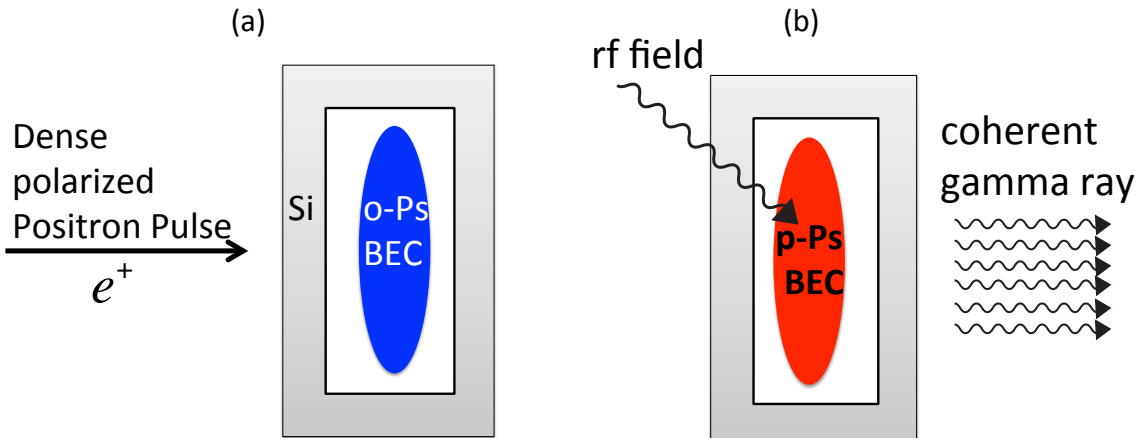

Figure 6.2: The schemes of making a Ps BEC, and then a γ-ray laser. (a) formation of a polarized o-Ps BEC inside a silicon cavity; (b) coherent γ rays emitted from a self-annihilating p-Ps condensate.

densities, n, and/or temperatures, T, than are required for laser cooled atoms [32]. Ps also has a small scattering length $a \sim 0.1$ nm, so that a Ps condensate remains a weakly interacting dilute Bose gas in the higher density regime, i.e., $(na^3 \ll 1)$. Second, a Ps BEC has a short metastable lifetime $\tau \sim \tau_o$ due to spontaneous annihilation into γ rays. Despite its short life, a Ps BEC can be observed though gamma-ray emission signatures [31]. As will be discussed later, an appropriately prepared condensate can be used as the gain medium for γ ray laser, which can be observed through the coherent emission of γ rays.

In the preparation of dense Ps, it has been shown [28, 84] that ortho-to-para spin exchange is one of the main mechanisms for quenching the o-Ps population. To avoid this population loss, a polarized positron beam should be used to generate a nonzero fraction of polarized o-Ps that is long-lived. During the condensation process spin-mixing collisions convert the unpolarized fraction of o-Ps to p-Ps, which quickly annihilates, and the remaining o-Ps is polarized. A standard design of a

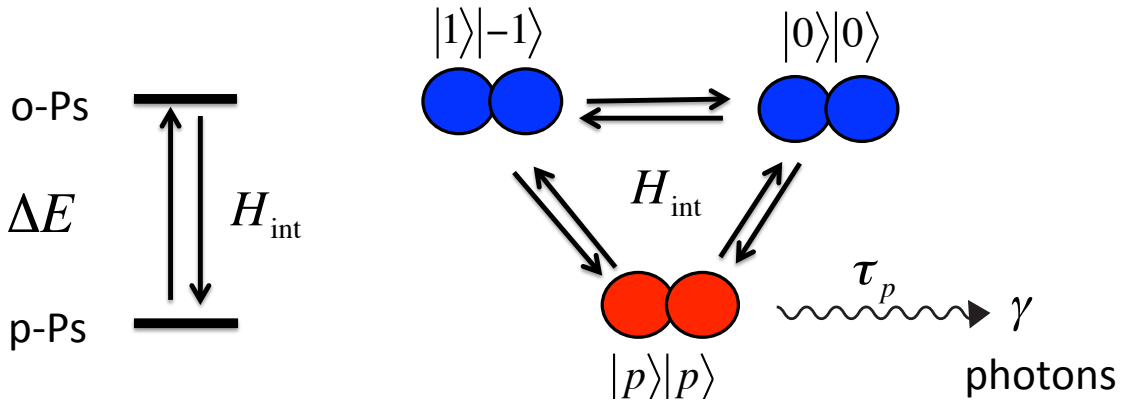

Figure 6.3: Competition between the ortho-para energy difference, $\Delta E = \epsilon$, and the spin-mixing interaction, $H_{\rm int}$.

γ-ray laser based on a Ps BEC uses polarized o-Ps as a storage medium, which is quickly converted to p-Ps by a magnetic field switch that triggers stimulated annihilation [27]. After applying the field, the system again obtains an unpolarized fraction that may undergo spin mixing and reduce the final γ-ray yield. In this chapter, we study the time evolution of o-Ps and p-Ps mixtures in order to understand the interplay of spin-mixing collision rates and γ-annihilation rates. We study spin mixing and Ps self-annihilation effects using two approaches: the solution of the time-dependent Gross-Pitaevskii (GP) equations that described a mixture of o- and p-Ps BECs, and a semi-classical rate-equation method. We also consider how to avoid para- to ortho- conversion during laser action.

To understand the physical properties of a Ps BEC, especially the interplay of spin mixing and Ps annihilation, we start with the GP formalism that consists of both para- and ortho- states. The formalism has the structure of a mixture of spin-1 and spin-0 BECs, and the full spin-mixing interactions have an $O(4)$ symmetry [85].

The internal energy splitting breaks this symmetry to a $SO(3)$ symmetry among the triplet states.

As illustrated in Fig. 6.3, there is a competition between the internal energy splitting and spin-mixing terms in the second-quantized Hamiltonian, which determines the ground state phase, the spin-mixing dynamics, and the stability of the system. At low density, the ground state phase consists of pure p-Ps. There is a critical density above which spin mixing becomes significant and the ground state acquires a non-zero o-Ps fraction. This criticality also plays an important role in determining the dynamics and the stability of a spinor BEC, beyond which strong spin-mixing will occur and breakdown the coherence of the condensate, which further inhibits the production of coherent γ rays.

This chapter is organized as follows. Sec. 6.1 starts with a formalism based on the Ps second-quantized Hamiltonian which is used to derive the time-dependent GP equations. In Sec. 6.1.2 we study the symmetry properties of the Ps system that are invariant under spin rotation. In Sec. 6.1.3, we show that there is a phase transition in the ground state composition at a critical density $n_{\rm c}$. Spin mixing and dynamic instability effects become significant for densities greater than $n_{\rm c}$. In Sec. 6.1.4, we study the spin-mixing dynamics of a mixed homogeneous BEC numerically and analytically at densities above and below $n_{\rm c}$. Sec. 6.2 considers the annihilation of Ps under the influence of spin mixing. We propose a scheme that optimizes the γ-ray laser from a polarized o-Ps BEC. The rate equation approach is first used to model the dynamics for an incoherent mixture. Then, we apply the time-dependent GP equations to simulate the time evolutions of a Ps condensate with decay. At the

same time, dynamic stability is taken into account through the Bogoliubov equations and tested numerically through the GP equations with spatial random noises. The last section summarizes our results.

6.1 Gross-Pitaevskii Theory for Positronium condensates

There are many previous studies of the interactions of two Ps atoms, including their fusion into the diatomic Ps molecule [86–88]. We use results of some of this previous work to determine the scattering lengths for low-energy Ps collisions that are relevant to describing a BEC of Ps within the conventional mean-field theoretical framework, the time-dependent Gross-Pitaevskii (GP) equation. In particular, we use the Gross-Pitaevskii theory to study physical properties of a mixture of o-Ps and p-Ps condensates, such as symmetry under spin rotation operations, stationary structure, and dynamics. The treatment here ignores the effects of electron-positron annihilation. These are included in subsequent sections.

There are four spin states of Ps which we designate by $|\mathrm{p}\rangle$, $|1\rangle$, $|0\rangle$, $|-1\rangle$, where $|\mathrm{p}\rangle$ is the p-Ps state, and $|M\rangle$ is the o-Ps state with spin projection of $M\hbar$ upon the $\hat{z}$-axis for $M = 1, 0, -1$.

6.1.1 Interaction Hamiltonian of spinor Ps condensates

We now derive the many-body interaction Hamiltonian for a dilute Ps gas. For a sufficiently cold and dilute gas, two Ps atoms can only interact through an overall s-wave interaction. Expressing their interaction in a basis of e^- and e^+ pairs,

we have

$$\begin{aligned} U(\mathbf{r},\mathbf{r}') &= \delta(\mathbf{r}-\mathbf{r}') \\ &\times \sum_{\substack{s^+m^+ \\ s^-m^-}}^{s^+=s^-} U_s |s^+m^+;s^-m^-\rangle\langle s^+m^+;s^-m^-|, \end{aligned} \tag{6.1}$$

where

$$U_s = \frac{4\pi\hbar^2 a_s}{m} \tag{6.2}$$

is the effective interaction expressed in terms of the scattering lengths $a_0 = 4.468 \times 10^{-10}$m and $a_1 = 1.586 \times 10^{-10}$ m [87, 88], and s^+m^+ (s^-m^-) denote the spin quantum numbers of the positron(electron) pair. The s-wave scattering constraint requires that that $s^+ = s^- \equiv s = 0$ or 1. It is convenient to express the sum in Eq. 6.1 as

$$\begin{aligned} &\sum_{m^+,m^-} U_1 \left|1m^+;1m^-\right\rangle\left\langle 1m^+;1m^-\right| + U_0 \left|00;00\right\rangle\left\langle 00;00\right| \\ &= U_1\mathbb{I} + (U_0 - U_1)\left|00;00\right\rangle\left\langle 00;00\right|, \end{aligned} \tag{6.3}$$

where $\mathbb{I}$ is the identity operator in the basis of s-wave scattering states. Next, we expand the lepton-pair ket $|00;00\rangle = 1/2\left(|\uparrow\downarrow\rangle - |\downarrow\uparrow\rangle\right)_{e^-} \otimes \left(|\uparrow\downarrow\rangle - |\downarrow\uparrow\rangle\right)_{e^+}$ in terms

of o-Ps and p-Ps states. It follows that

$$\begin{aligned}
&(|\uparrow\downarrow\rangle - |\downarrow\uparrow\rangle)_{e^-} \otimes (|\uparrow\downarrow\rangle - |\downarrow\uparrow\rangle)_{e^+} \\
&= |\uparrow\uparrow\rangle_{\mathrm{Ps}_1} \otimes |\downarrow\downarrow\rangle_{\mathrm{Ps}_2} + |\downarrow\downarrow\rangle_{\mathrm{Ps}_1} \otimes |\uparrow\uparrow\rangle_{\mathrm{Ps}_2} \\
&-1/2\,(|\uparrow\downarrow\rangle + |\downarrow\uparrow\rangle)_{\mathrm{Ps}_1} \otimes (|\uparrow\downarrow\rangle + |\downarrow\uparrow\rangle)_{\mathrm{Ps}_2} \\
&+1/2\,(|\uparrow\downarrow\rangle - |\downarrow\uparrow\rangle)_{\mathrm{Ps}_1} \otimes (|\uparrow\downarrow\rangle - |\downarrow\uparrow\rangle)_{\mathrm{Ps}_2} \\
&= |1\rangle|-1\rangle + |-1\rangle|1\rangle - |0\rangle|0\rangle + |\mathrm{p}\rangle|\mathrm{p}\rangle \\
&\equiv |\Psi_s\rangle. \qquad (6.4)
\end{aligned}$$

Substituting $|\Psi_s\rangle$ into Eq. 6.1, we obtain the effective interaction represented in the basis of Ps scattering states

$$U(\mathbf{r},\mathbf{r}') \quad = \delta(\mathbf{r}-\mathbf{r}')\left(g_0\mathbb{I} + g_1\,|\Psi_s\rangle\langle\Psi_s|\right). \qquad (6.5)$$

where $g_0 = U_1$ and $g_1 = (U_0 - U_1)/4$.

To construct the many-body interaction Hamiltonian, we follow the standard procedure and replace the two-body interaction with a sum over field operators

$$\mathcal{H}_{\mathrm{int}} \;=\; \int d^3r d^3r' \left[\Psi_i^\dagger(\mathbf{r})\Psi_j^\dagger(\mathbf{r}')U_{ijkl}(\mathbf{r},\mathbf{r}')\Psi_k(\mathbf{r}')\Psi_l(\mathbf{r})\right]. \qquad (6.6)$$

Performing the delta function integral, and re-arranging terms, the second-quantized

interaction Hamiltonian can take the following form:

$$\begin{aligned}\mathcal{H}_{\text{int}} &= \frac{g_0}{2}\sum_{\substack{i,j=\\0,\pm1,\text{p}}}\int d^3r\,\Psi_i^\dagger\Psi_j^\dagger\Psi_i\Psi_j \\ &+\frac{g_1}{2}\int d^3r \begin{pmatrix} 2\Psi_1\Psi_{-1} \\ -\Psi_0\Psi_0 \\ \Psi_\text{p}\Psi_\text{p}\end{pmatrix}^\dagger \begin{pmatrix} 1 & 1 & 1 \\ 1 & 1 & 1 \\ 1 & 1 & 1\end{pmatrix} \begin{pmatrix} 2\Psi_1\Psi_{-1} \\ -\Psi_0\Psi_0 \\ \Psi_\text{p}\Psi_\text{p}\end{pmatrix},\end{aligned} \tag{6.7}$$

where $\Psi_i(\mathbf{r})$ $\left(\Psi_i^\dagger(\mathbf{r})\right)$ annihilates(creates) a particle of spin state $|i\rangle$ at point $\mathbf{r}$, and g_0 and g_1 are pseudo-potential constants with values $g_0/\hbar = 1.154\times10^{-7}$ cm^3/s and $g_1/\hbar = 5.240\times10^{-8}$ cm^3/s. The full many-body Hamiltonian, including the single-particle contribution, is

$$\mathcal{H} = \int d^3r \sum_{i=0,\pm1,\text{p}} \Psi_i^\dagger\left(\frac{\mathbf{p}^2}{2m}+V_\text{ext}+\epsilon_i\right)\Psi_i + \mathcal{H}_\text{int} \tag{6.8}$$

where $\mathbf{p}$ is the momentum operator, m is the mass of Ps, V_ext is the external potential, and ϵ_i is the internal energy of spin state i. Throughout this chapter, $\epsilon_1 = \epsilon_0 = \epsilon_{-1} \equiv \epsilon_\text{o}$.

Now we go to the mean field limit by replacing each field operator Ψ_i by the corresponding mean field value $\psi_i = \langle\Psi_i\rangle$ [32]. The interaction term can be expressed as

$$\mathcal{H}_\text{int} = \frac{1}{2}\int d^3r\,\left(g_0n^2 + g_1\left|2\psi_1\psi_{-1}-\psi_0^2+\psi_\text{p}^2\right|^2\right) \tag{6.9}$$

where $n = \sum_{i=0,\pm1,\text{p}}|\psi_i|^2$ denotes the total number density. The equations of motion

can be found by taking the functional derivative of the mean-field Hamiltonian

$$i\,\hbar\dot{\psi}_i = \frac{\delta\mathcal{H}}{\delta\psi_i^*}. \tag{6.10}$$

This yields the time-dependent GP equations:

$$\begin{aligned}
i\,\hbar\dot{\psi}_1 &= \left(H_0 + \epsilon_{\rm o} + 2g_1|\psi_{-1}|^2\right)\psi_1 + g_1\psi_{-1}^*(\psi_{\rm p}^2 - \psi_0^2) \\
i\,\hbar\dot{\psi}_0 &= \left(H_0 + \epsilon_{\rm o} + g_1|\psi_0|^2\right)\psi_0 - g_1\psi_0^*(2\psi_1\psi_{-1} + \psi_{\rm p}^2) \\
i\,\hbar\dot{\psi}_{-1} &= \left(H_0 + \epsilon_{\rm o} + 2g_1|\psi_1|^2\right)\psi_{-1} + g_1\psi_1^*(\psi_{\rm p}^2 - \psi_0^2) \\
i\,\hbar\dot{\psi}_{\rm p} &= \left(H_0 + \epsilon_{\rm p} + g_1|\psi_{\rm p}|^2\right)\psi_{\rm p} + g_1\psi_{\rm p}^*(2\psi_1\psi_{-1} - \psi_0^2)
\end{aligned} \tag{6.11}$$

where

$$H_0 = \frac{\mathbf{p}^2}{2m} + V_{\rm ext} + g_0 n. \tag{6.12}$$

The g_1 terms in the second half of the RHS of Eq. 6.11 are responsible for the population exchange among spin states. For the remainder of this section, we take $\epsilon_{\rm o} = \epsilon$ and $\epsilon_{\rm p} = 0$, which amounts to ignoring the spontaneous annihilation process.

6.1.2 Symmetry under spin rotations, the $O(4)$ group

We now consider the symmetry of the system including interactions. We can express $\mathcal{H}_{\rm int}$ in terms of the ortho–para- spinor $\psi^T = (\psi_1,\ \psi_0,\ \psi_{-1},\ \psi_{\rm p})$

$$\mathcal{H}_{\rm int} = \frac{1}{2}\int dr^3\ \left(g_0 n^2 + g_1\left|\psi^T Q\psi\right|^2\right), \tag{6.13}$$

where

$$Q = \begin{pmatrix} 0 & 0 & 1 & 0 \\ 0 & -1 & 0 & 0 \\ 1 & 0 & 0 & 0 \\ 0 & 0 & 0 & 1 \end{pmatrix}. \tag{6.14}$$

In this basis, the components of the spin operator $\mathbf{S} = S_a \hat{\mathbf{e}}_a$, with $a = 1, 2, 3$, are expressed as

$$S_1 = \frac{1}{\sqrt{2}} \begin{pmatrix} 0 & 1 & 0 & 0 \\ 1 & 0 & 1 & 0 \\ 0 & 1 & 0 & 0 \\ 0 & 0 & 0 & 0 \end{pmatrix},$$

$$S_2 = \frac{1}{\sqrt{2}} \begin{pmatrix} 0 & -i & 0 & 0 \\ i & 0 & -i & 0 \\ 0 & i & 0 & 0 \\ 0 & 0 & 0 & 0 \end{pmatrix}, \; S_3 = \begin{pmatrix} 1 & 0 & 0 & 0 \\ 0 & 0 & 0 & 0 \\ 0 & 0 & -1 & 0 \\ 0 & 0 & 0 & 0 \end{pmatrix}. \tag{6.15}$$

It is straightforward to show that $[S_a, Q] = 0$ for all a.

In the limit that $\psi_{\rm p} = 0$, the interaction Hamiltonian is identical to that for a normal spin-1 spinor condensate [89, 90]. That is

$$\mathcal{H}_{\rm int} \;=\; \frac{1}{2} \int d^3r \, \left(g_0 n^2 + g_1 n^2 \left(1 - \langle \mathbf{S} \rangle \cdot \langle \mathbf{S} \rangle \right) \right) \tag{6.16}$$

where $\langle S_a \rangle = \psi^\dagger S_a \psi / n$ with $a = 1, 2, 3$ is the average spin per atom, so that $0 \leq \langle \mathbf{S} \rangle \cdot \langle \mathbf{S} \rangle \leq 1$. Since $g_1 > 0$, the ground state will have $\langle \mathbf{S} \rangle \cdot \langle \mathbf{S} \rangle = 1$ in the limit $\psi_{\rm p} = 0$.

Thus, in this limit, the ortho- sector is a ferromagnetic condensate. However, when $\psi_{\rm p} \neq 0$, the ground state has $\langle \mathbf{S} \rangle = 0$, as will be shown in the next section. As we shall see, in parameter regimes of current experimental interest, Eq. (6.13) can induce significant interconversion between o-Ps and p-Ps.

To specify the symmetry of the system, we can use $\mathbf{S}$ as the generator of rotations $D_{\hat{\mathbf{n}}}(\alpha) = e^{-i\alpha \hat{\mathbf{n}} \cdot \mathbf{S}}$ among the spin-1 states, where α, $\hat{\mathbf{n}}$ denote the angle and axis of the rotation. Since $\psi^T Q \psi$ is invariant under $\psi \to e^{i\alpha S_a}\psi$, we see that $\mathcal{H}_{\rm int}$ is also invariant under arbitrary spin rotations in the ortho- sector, and $\langle S_a \rangle$ for each a is a conserved quantity of the system. This implies that from a given solution to Eq. (6.11), we can obtain a manifold of equivalent solutions related by rotations of the form $D_{\hat{\mathbf{n}}}(\alpha)$. In particular, this implies that there is a continuous degeneracy of the many-body ground state.

Rotations between the ortho- sector and the para- sector $e^{-i\alpha \hat{\mathbf{n}} \cdot \mathbf{R}}$ can be generated by operators $\mathbf{R} = R_a \hat{\mathbf{e}}_a$ with $a = 1, 2, 3$, and

$$R_1 = \frac{1}{\sqrt{2}} \begin{pmatrix} 0 & 0 & 0 & 1 \\ 0 & 0 & 0 & 0 \\ 0 & 0 & 0 & -1 \\ 1 & 0 & -1 & 0 \end{pmatrix},$$

$$R_2 = \frac{1}{\sqrt{2}} \begin{pmatrix} 0 & 0 & 0 & -i \\ 0 & 0 & 0 & 0 \\ 0 & 0 & 0 & -i \\ i & 0 & i & 0 \end{pmatrix}, \; R_3 = \begin{pmatrix} 0 & 0 & 0 & 0 \\ 0 & 0 & 0 & -1 \\ 0 & 0 & 0 & 0 \\ 0 & -1 & 0 & 0 \end{pmatrix}. \tag{6.17}$$

It can be shown that $\mathcal{H}_{\rm int}$ is also invariant under rotations $\psi \rightarrow e^{i\alpha R_a}\psi$. The commutation relations among S_a and R_b are those of the $O(4)$ group [85]

$$[S_a, S_b] = i\varepsilon_{abc}S_c, \tag{6.18}$$

$$[R_a, R_b] = i\varepsilon_{abc}S_c, \tag{6.19}$$

$$[S_a, R_b] = i\varepsilon_{abc}R_c. \tag{6.20}$$

An arbitrary group element is represented by

$$D_{\hat{\mathbf{n}}_1,\hat{\mathbf{n}}_2}(\alpha_1, \alpha_2) = e^{-i\alpha_1\hat{\mathbf{n}}_1\cdot\mathbf{S} - i\alpha_2\hat{\mathbf{n}}_2\cdot\mathbf{R}}, \tag{6.21}$$

where the parameters $\alpha_1, \hat{\mathbf{n}}_1$ represent the rotation angle and rotation axis for the ortho-sector, and $\alpha_2, \hat{\mathbf{n}}_2$ correspond to rotations between the ortho- and para- sectors. The group of elements spanned by $\alpha_2 = 0$, form a subgroup equivalent to $SO(3)$ and corresponds to physical spin rotations in the ortho- sector. Including the internal energy splitting between the ortho- and para- sectors, the symmetry of the full system is reduced from a full $O(4)$ symmetry to this $SO(3)$ subgroup. This symmetry is broken in the full Hamiltonian due to the one-body internal energy difference between ortho- and para- Ps. The only global symmetry is that generated by the operators S_a [89].

6.1.3 Ground State of a Ps BEC

We now consider the ground state of a Ps BEC in the zero temperature limit. Suppose there exists a stationary state $\psi_i(\mathbf{r}, t) = \sqrt{n_i(\mathbf{r})}e^{i\phi_i(\mathbf{r})}e^{-i\mu t/\hbar}$, where n_i and ϕ_i are the number density and phase for the component i, and μ is the chemical

potential. Substituting this ansatz into Eq. 6.11, we can calculate the equilibrium composition of the ground state. In proposed implementations of Ps BEC, [26, 31] Ps is collected in a cavity of volume $\sim 10^{-13}$ cm^3 with a range of densities between 10^{18} cm^{-3} and 10^{21} cm^{-3}. Given the minimal required densities for condensation, the largest attainable values of the healing length, $\xi = \hbar/\sqrt{2m\mu}$, are about $\xi \sim 10^{-6}$ cm. This is much smaller than the characteristic cavity dimension $\sim 10^{-4}$ cm. For this reason, we will neglect the contribution of the kinetic energy operator $\mathbf{p}^2/2m$ for the remainder of this section so that the condensate is uniform in space.

To understand the ortho-/para- balance of the condensate, we consider the competition between the g_1 interaction and the energy separation ϵ, which is manifested in the energy as

$$E = \int d^3r \left(\epsilon n_{\rm o} + \frac{g_1}{2} \left| 2\psi_1\psi_{-1} - \psi_0^2 + \psi_{\rm p}^2 \right|^2 \right), \tag{6.22}$$

where $n_{\rm o} = n_1 + n_0 + n_{-1}$. We rewrite the term that is quartic in ψ_i as

$$\frac{g_1}{2} \left| 2\sqrt{n_1 n_{-1}} e^{i(\phi_1+\phi_{-1})} - n_0 e^{2i\phi_0} + n_{\rm p} e^{2i\phi_{\rm p}} \right|^2. \tag{6.23}$$

The effect of $\epsilon > 0$ is to suppress $n_{\rm o}$ in the ground state. The quartic term on the other hand is minimized at nonzero $n_{\rm o}$. In the limit of $\epsilon \gg g_1 n$, we obtain a pure p-Ps BEC, $n_{\rm o} \to 0$. In the other limit, $\epsilon \ll g_1 n$, the ground state energy is dominated by the quartic interaction, which vanishes when

$$n_{\rm p} e^{2i\phi_{\rm p}} = n_0 e^{2i\phi_0} - 2\sqrt{n_1 n_{-1}} e^{i(\phi_1+\phi_{-1})}. \tag{6.24}$$

Since $\epsilon_{\rm p} < \epsilon_{\rm o}$, the ground state has the largest value of $n_{\rm p}$ consistent with Eq. 6.24 and the fixed value of $n = n_{\rm o} + n_{\rm p}$. It can be seen from Eq. 6.24 that $n_{\rm p}$ is

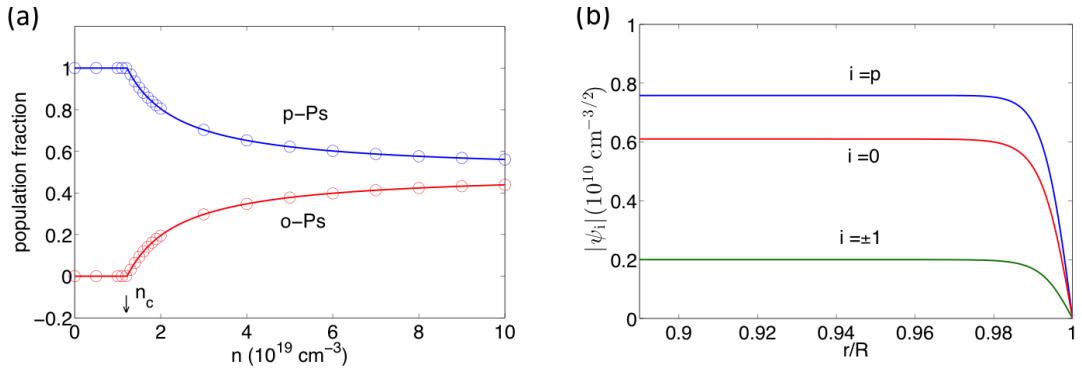

Figure 6.4: Panel (a): relative population fraction of ortho-/para- sectors as a function of density. The solid lines correspond to Eq. 6.28, and the circled dots are obtained by using an imaginary-time approach for the GP equation. The critical density $n_c \approx 1.2 \times 10^{19}\text{cm}^{-3}$ corresponds to a nonzero occupation of the ortho-sector in the ground state. Below the critical density, the ground state is a pure p-Ps condensate. In the high density limit, $n \gg n_c$, the ratio of $n_p/n_o \to 1$. Panel (b): $|\psi_i(r)|$ for the ground state of Ps BEC at $n = 10^{20}$ cm^{-3} confined in a spherical cavity of volume $4\pi R^3/3 = 10^{-13}$ cm^3. These results, obtained from integration of Eq. 6.11 in imaginary time, demonstrate the uniformity and miscibility of the mixed condensates and the equality $|\psi_1| = |\psi_{-1}|$. The density variation is confined to a boundary layer with thickness about 1% of the cavity radius R. Starting from random initial conditions, the numerical calculation converges on a solution that has the phase relationship indicated in Eq. 6.26.

maximized when $\phi_p + q\pi = \phi_0 = [\phi_1 + \phi_{-1} + (2r+1)\pi]/2$ for integers q, r, and thus $n_p = n_0 + 2\sqrt{n_1 n_{-1}}$. To see whether there exists a number imbalance between n_1 and n_{-1}, we let $n_1 = \bar{n} + m$ and $n_{-1} = \bar{n} - m$, where $\bar{n}$ represents the average density of the two species, and m denotes the number imbalance. Keeping $n_1 + n_{-1}$ a constant while varying m, we find that $\sqrt{n_1 n_{-1}} = \sqrt{\bar{n}^2 - m^2}$ has the largest value if the imbalance $m = 0$. Therefore, we obtain the maximal p-Ps density

$$n_p = n_0 + 2\bar{n} = n_o, \tag{6.25}$$

so ortho- and para- populations become equal in the high-density limit. The ortho-sector is equivalent to the polar state of a spin-1 condensate with $\langle \mathbf{S} \rangle = 0$ [89, 91], for which there exists a degree of freedom to distribute the population between n_0

and $\bar{n}$. Adapting the parametrization given by Ho [89], which has since become standard [91, 92], we find the general expression for the ground state to be, up to an overall phase,

$$\psi = \sqrt{n_{\rm o}} \begin{pmatrix} -\frac{1}{\sqrt{2}} e^{-i\alpha} \cos(\beta) \\ \sin(\beta) \\ \frac{1}{\sqrt{2}} e^{i\alpha} \cos(\beta) \\ 0 \end{pmatrix} + \sqrt{n_{\rm p}} \begin{pmatrix} 0 \\ 0 \\ 0 \\ \pm 1 \end{pmatrix} \tag{6.26}$$

where α, β are arbitrary real numbers. To fully specify the ground state of the system, we now identify the relationship between $n_{\rm o}$ and $n_{\rm p}$.

When the effects associated with ϵ and the quartic term in Eq. 6.22 are comparable, $n_{\rm p}$ will lie in the range $n/2 < n_{\rm p} < n$. To determine $n_{\rm p}$, we write $n_{\rm p} = n_{\rm o} + \delta n$ and adopt the phases and densities described in our derivation of Eq. 6.26, then Eq. 6.22 takes the form

$$E = \int d^3 r \left(\epsilon n_{\rm o} + \frac{g_1}{2} \delta n^2 \right). \tag{6.27}$$

Using $n_{\rm o} = (n - \delta n)/2$, we find $n_{\rm p}$ by minimizing Eq. 6.27 with respect to δn, for fixed n. We obtain

$$\begin{aligned} n_{\rm p}/n &= \tfrac{1}{2}(1 + \tfrac{n_{\rm c}}{n}) \quad \text{if} \;\; n > n_{\rm c} \\ n_{\rm p}/n &= 1 \qquad\qquad\quad \text{if} \;\; n \leq n_{\rm c} \end{aligned} \tag{6.28}$$

where the critical density,

$$n_{\rm c} = \frac{\epsilon}{2 g_1}, \tag{6.29}$$

is that at which the para- fraction starts to depart from 1. For Ps, ϵ is known experimentally and theoretically [25] and g_1 is calculated from Eq. 6.5. With these values, we find $n_c \approx 1.2 \times 10^{19}$ cm^{-3}.

We have verified this simple model by exact numerical calculation of the ground state of a Ps BEC as a function of density by integration of the GP equations, Eq. 6.11, in imaginary time. As shown in Fig. 6.4(a), the results are consistent with Eq. 6.28.

The results of this section are based on the premise that individual condensates are uniform and miscible throughout the cavity. To verify the validity of this picture for Ps confined in a cavity, we impose a hard-wall boundary condition on Eq. 6.11 and calculate the ground state by integrating in imaginary time. For an isotropic cavity of volume 10^{-13} cm^3 and total density $n = 10^{20}$ cm^{-3}, we obtain the ground-state solution of a mixed condensate given in Fig. 6.4(b). We see that the assumption holds nicely in the figure with very small boundary effect. The individual condensates are miscible and uniform throughout the bulk region, and the spatial variation around the boundary is only about 0.01 of the cavity radius. In addition, the stationary populations obtained here coincide with those shown in Fig. 6.4(a).

6.1.4 Spin-mixing dynamics

If a Ps BEC is prepared in a non-stationary state, the interaction Hamiltonian $\mathcal{H}_{\rm int}$ can lead to spin-mixing dynamics [91–93]. To understand the basics of

spin-mixing dynamics and its dependence on the critical density n_c, we neglect the contribution of the kinetic energy operator and treat the condensate as uniform. GP calculations of nonuniform condensates are included in the next section, where we find pronounced effects of inhomogeneity for $n > n_c$.

It is convenient to reformulate the coupled GP equations in terms of the fractional populations of individual spin states and the relative phases. For the simplified case involving only the wavefunctions $\psi_p = \sqrt{n\rho}e^{i\phi_p}$ and $\psi_0 = \sqrt{n(1-\rho)}e^{i\phi_0}$, the equations of motion can be recast as

$$\begin{aligned} \frac{d\rho}{d\tau} &= \nu\rho(1-\rho)\sin 2\phi, \\ \frac{d\phi}{d\tau} &= \frac{\nu}{2}(1-2\rho)(1+\cos 2\phi) + 1, \end{aligned} \tag{6.30}$$

where $\phi = \phi_p - \phi_0$ is the relative phase between the two components, ρ is the population fraction in the para- component, $\tau = \epsilon t/\hbar$, and $\nu = n/n_c$ (from Eq. 6.29). As in the Josephson effect [94], the phase and density differences drive population oscillations between the two species. Using a method from Ref. [95], Eq. 6.30 can be solved by recognizing that ρ and ϕ are conjugate variables of a functional,

$$\mathcal{E} = \frac{\nu}{2}\rho(1-\rho)(1+\cos 2\phi) + \rho, \tag{6.31}$$

which is a constant of motion determined by the initial values $\rho(\tau_0)$ and $\phi(\tau_0)$ at an arbitrary value of the scaled time $\tau = \tau_0$. Combining Eq. 6.31 and Eq. 6.30, we obtain

$$\left(\frac{d\rho}{d\tau}\right)^2 = 4\nu\left(\rho - \mathcal{E}\right)(\rho - \rho_+)(\rho - \rho_-) \tag{6.32}$$

where

$$\rho_{\pm} = \frac{1}{2\nu}\left(1+\nu \pm \sqrt{(1+\nu)^2 - 4\mathcal{E}\nu}\right). \tag{6.33}$$

As shown in [95,96], this differential equation can be solved by the Jacobi elliptic [97, 98] function sn (or cn) as

$$\rho = \rho_3 + (\rho_2 - \rho_3)\mathrm{sn}^2\left(\sqrt{\nu(\rho_1-\rho_3)}\,\tau, k_1\right) \tag{6.34}$$

where k_1 is the elliptic modulus given by

$$k_1^2 = \frac{\rho_2 - \rho_3}{\rho_1 - \rho_3} \tag{6.35}$$

and ρ_i are the three zeros of Eq. 6.32, $(\rho_i = \mathcal{E}, \rho_{\pm})$, ordered so that $\rho_1 > \rho_2 > \rho_3$. Eq. 6.34 is strictly periodic in variable τ, in the limit $k_1 \to 0$ it becomes sinusoidal. The period of the solution, T, can be calculated in terms of the elliptic integral of the first kind $F(\phi, k)$ [97, 98] as

$$\mathrm{T} = \frac{2}{\sqrt{\nu\,(\rho_1-\rho_3)}} F\left(\frac{\pi}{2}, k_1\right). \tag{6.36}$$

We have chosen the origin $\tau = 0$, so that $\rho(0) = \rho_3$, the minimum value of para-population fraction. The population oscillates between ρ_3 and ρ_2.

The internal energy difference ϵ between ortho- and para- states gives rise to a barrier for the conversion from p-Ps to o-Ps. This interconversion happens when the interaction that exchanges populations is sufficiently strong to overcome the energy barrier. Thus, we again encounter the competition between the ϵ and the g_1 terms (i.e. spin-mixing interaction) of Eq. 6.22. As discussed above, this competition is

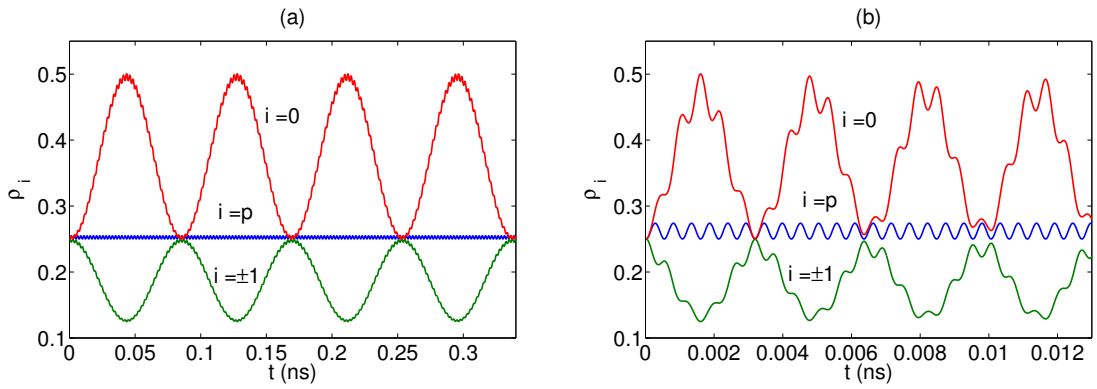

Figure 6.5: Time evolution of the population fractions ρ_i for a system prepared with $\rho_i(t=0) = 1/4$ at densities (a) $n = 10^{18}$ cm^{-3} (b) $n = 10^{20}$ cm^{-3}. In the former case, $n_c > n$ and the spin mixing between the ortho- and para- sectors is minimal; for the latter case, $n_c < n$ and a more substantial spin-mixing is observed. In general, spin mixing between ortho- and para- states is significant only for $n > n_c$ as predicted in Eq. 6.34. Note that Ps annihilation is not included in the calculations.

expressed in the comparison of the condensate density n with the critical value n_c, which corresponds to when the interaction energy is comparable to ϵ. Using the ratio $\nu = n/n_c = 2g_1 n/\epsilon$ as a parameter, we estimate the limiting behaviors of the solution Eq. 6.34, for which the amplitude of population variation is determined by $\rho_2 - \rho_3$. When $\nu \ll 1$, $\rho_2 - \rho_3 \approx \nu(1-\rho(\tau_0))\rho(\tau_0)$, which is of order ν. Thus, regardless of what the initial conditions are, ρ is limited by this quantity, and the p-Ps fraction will not deviate significantly from $\rho \approx \rho_3$. On the contrary, when $\nu \gg 1$, we have $\rho_2 - \rho_3 \approx |1 - 2\rho(\tau_0)|$ for $\cos 2\phi(\tau_0) = 1$ and $\rho_2 - \rho_3 \approx \rho(\tau_0)$ for $\cos 2\phi(\tau_0) = -1$, which are both of order 1. The solution ρ can take any value between 0 and 1. From this analysis, we can see the spin mixing occurs when the condensate density is greater than the critical value n_c.

Taking all four states into consideration, we use Eq. 6.11 to compute numerically the time evolution of populational fractions ρ_i for $i = 0, \pm 1, \mathrm{p}$. The total

population is conserved in this evolution, $\sum_i \rho_i = 1$. Fig. 6.5(a) shows the propagation of the four components at density 10^{18} cm^{-3}, in a case for which the initial populations are all equal. The three ortho- states continuously exchange populations and exhibit sinusoidal time evolution. On the other hand, the para- component has very small oscillations, corresponding to the smallness of the para-ortho- interconversion. Since here we have $n/n_c = \nu = 0.08$, this result is consistent with the solution of the two-component system. In addition, it also implies that although the unpolarized ortho- fraction diminishes very quickly in many experimental scenarios [28], it would be stable in the condensed phase if $n < n_c$. Considering the case with $n > n_c$, we set $n = 10^{20}$ cm^{-3} and use the same initial conditions. The time evolutions are shown in Fig. 6.5(b). Here we can clearly see a more substantial oscillatory pattern for the para- fraction and some additional small-scale fluctuations on the ortho- sector, which reveals a stronger para-ortho- spin-mixing occurring at the high density. Both cases agree very well with our former estimate regarding the critical density.

6.2 Positronium annihilation and γ-ray laser

Proposals for a γ-ray laser [26, 27, 31] call for preparing a BEC of polarized o-Ps. This is used as a storage medium which can subsequently be changed to a gain medium by ortho-para conversion. The p-Ps atoms can then participate in stimulated emission of the γ-rays produced in p-Ps annihilation. As we have shown above, there are complex effects of spin mixing when the Ps density exceeds the

critical density n_c. We now investigate how these effects modify the population distribution within a Ps BEC that is also subject to the processes of spontaneous annihilation. We find that spin mixing can significantly modify the optimal strategy for producing a γ-ray laser.

We consider two approaches. The first is a semi-classical rate-equation approach appropriate for an incoherent mixture of Ps atoms. The second is the full solution of time-dependent GP equations, taking spontaneous annihilation into account. On the microscopic level, the GP equations exhibit behavior much different from the classical rate equations, but when spatial averaging is included, the two approaches give similar results for $n > n_c$.

6.2.1 The rate equation approach

In this section we use a simple rate equation approach to model Ps annihilation in arbitrary mixtures of o-Ps and p-Ps subject to spin-mixing collisions. This approach should be valid for incoherent Ps mixtures which can be modeled as weakly-interacting classical gases [32]. It provides a reference point for understanding the dynamics of nondegenerate gases of Ps, and for comparison with the mixed Ps BECs that need to be described by the GP equations.

Referring to the notation introduced above, the possible spin-mixing collisions

can be described schematically by [88]

$$\begin{aligned} |0\rangle\,|0\rangle &\underset{k_1}{\overset{k_1'}{\rightleftharpoons}} |\mathrm{p}\rangle\,|\mathrm{p}\rangle \\ |+-\rangle &\underset{k_2}{\overset{k_2'}{\rightleftharpoons}} |\mathrm{p}\rangle\,|\mathrm{p}\rangle \\ |0\rangle\,|0\rangle &\underset{k_3}{\overset{k_3'}{\rightleftharpoons}} |+-\rangle \end{aligned} \tag{6.37}$$

where k_α and k'_α denote the rate constants for the left-to-right and inverse processes respectively, and $|+-\rangle = (|1\rangle|-1\rangle + |-1\rangle|1\rangle)/\sqrt{2}$. The first two of these processes describe direct ortho-para- interconversion. The third is associated with redistribution of ortho- state populations. Treating the inelastic scattering events as individual reactions among particles of classical gases, we can calculate the rate equations [32] by summing the products of rate constants, k, and reactant population fractions, ρ_i. Adding the decay terms representing Ps annihilation, the rate equations can be expressed as

$$\begin{aligned} \dot{\rho}_1 &= k_3\rho_0^2 + k_2'\rho_\mathrm{p}^2 - (k_2 + k_3')\rho_1\rho_{-1} - \rho_1/\tau_\mathrm{o} \\ \dot{\rho}_0 &= k_3'\rho_1\rho_{-1} + k_1'\rho_\mathrm{p}^2 - (k_1 + k_3)\rho_0^2 - \rho_0/\tau_\mathrm{o} \\ \dot{\rho}_{-1} &= k_3\rho_0^2 + k_2'\rho_\mathrm{p}^2 - (k_2 + k_3')\rho_1\rho_{-1} - \rho_{-1}/\tau_\mathrm{o} \\ \dot{\rho}_\mathrm{p} &= k_1\rho_0^2 + k_2\rho_1\rho_{-1} - (k_1' + k_2')\rho_\mathrm{p}^2 - \rho_\mathrm{p}/\tau_\mathrm{p} \end{aligned} \tag{6.38}$$

where ρ_0, $\rho_{\pm1}$, and ρ_p are the fractions of the four spin states. Since the total population decays in time, we define the population fractions as $\rho_i(t) = n_i(t)/n_\mathrm{ini}$, where $n_\mathrm{ini} = n(t=0)$. We can calculate the rate constants as $k_\alpha = n_\mathrm{ini}\langle v\sigma_\alpha\rangle$, where $\langle\rangle$ stands for the thermal average over the relative velocity v, and the cross-sections

can be calculated from first-principles quantum mechanics [88].

Here we use the same basis transformation procedure given in Eq.6.4 to calculate the cross-sections. We find that the effective scattering lengths $a_{ij,kl}$ at which two Ps atoms in states i, j are scattered to states k, l are

$$a_{ij,kl} = a_1 \delta_{ik} \delta_{jl} + \frac{a_0 - a_1}{4} \langle kl|\Psi_s\rangle \langle \Psi_s|ij\rangle \,. \tag{6.39}$$

In the low-energy limit, the corresponding cross-section is given by $\sigma_{ij,kl} = 8\pi a_{ij,kl}^2$. The indices should be specified regarding the three spin-mixing processes, Eq. 6.37, which gives rise to $\sigma_1 = 0.130 \times 10^{-14}$ cm^2 and $\sigma_2 = \sigma_3 = 0.261 \times 10^{-14}$ cm^2. These results are consistent with an equivalent procedure found in Ref. [87, 88]. It should be noted that o-Ps and p-Ps have different internal energies, so that the thermal averages of the corresponding k_α and k'_α will also be different.

There are two main mechanisms in the rate equations. Spin mixing has the effect of distributing populations of the four states into an equilibrium, while Ps annihilation depletes populations. For the timescale of interest (1 ns), the system mainly decays through the para- state. As an example, we consider a thermal gas of Ps at temperature $T = 15\,K$ and density $n_{\rm ini} = 10^{18}$ cm^{-3}. For these conditions, the magnitudes of the various rate constants are between 10^9 s^{-1} and 10^{10} s^{-1}, which is comparable to the p-Ps decay rate. We propagate the rate equations in Eq. 6.38 with initial condition $\rho_{\rm p}(t = 0) = 1,\ \rho_{\rm o}(t = 0) = 0$ and plot the resulting time evolution in Fig. 6.6(a). Initially a small portion of p-Ps is converted to o-Ps. After p-Ps decays below a threshold $k_{1,2}\rho_{\rm p} \lesssim 1/\tau_{\rm p}$ further conversion from para- to ortho- becomes small and the ortho- population begins to decay away. When the para-

state is mostly depleted, the dominant decay process comes from conversion from ortho- to para- followed by para- self-annihilation. At this point, the ortho-to-para spin-mixing rate is slower than the p-Ps decay rate, which creates a bottleneck that slows down the decay process. Thus, at $t = 1$ ns, we can still see a fraction of the total population remains in the ortho- sector.

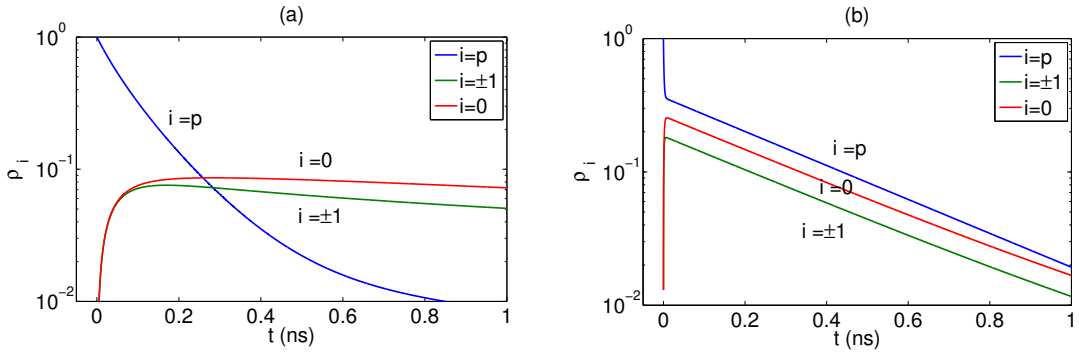

Figure 6.6: Evolution of the population fractions calculated with the rate equations (Eq. 6.38) at densities (a) $n_{\rm ini} = 10^{18}$ cm^{-3} and (b) $n_{\rm ini} = 10^{20}$ cm^{-3}. In both cases the initial population is pure p-Ps. In the low density case, the spin mixing is not sufficiently strong to reach a quasi-equilibrium. At long times, the para- population is significantly depleted and the ortho- population slowly decays away through spin-mixing with the para- sector. In the high density case, the relative populations quickly reach a quasi-equilibrium and collectively decay with an effective time constant $\tau_{\rm eff} \approx 4\tau_{\rm p}$.

At a density of $n_{\rm ini} = 10^{20}$ cm^{-3}, all the rate constants are increased by two orders of magnitude. The same initial conditions give rise to a qualitatively different evolution as shown in Fig. 6.6(b). Since the spin mixing rates are much stronger than the p-Ps decay rate, we expect rapid population redistribution on a timescale shorter than $\tau_{\rm p}$. Thus the relative populations remain in quasi-equilibrium at all times during the decay process. As shown in Fig. 6.6(b), all components decay with an effective lifetime $\tau_{\rm eff} \approx 4\ \tau_{\rm p}$ during this quasi-equilibrium redistribution. For the same reason, regardless of the initial state of the system, it quickly acquires

some mixture of the para- state and decays, so that the system loses its population more rapidly than for the lower density case. By $t = 1$ ns, a substantial fraction of initial Ps has decayed; at longer times, the population decays more slowly due to the bottleneck effect discussed above.

6.2.2 The Gross-Pitaevskii equations

In this section, we follow the GP formulation provided in Sec. 6.1 and take into account the effect of Ps annihilation. To incorporate the Ps decay into the formulation, we use an effective Hamiltonian which modifies the internal energies of individual species with an imaginary component

$$\begin{aligned} \epsilon_{\mathrm{o}} &= \epsilon - i\frac{\hbar}{2\tau_{\mathrm{o}}}, \\ \epsilon_{\mathrm{p}} &= -i\frac{\hbar}{2\tau_{\mathrm{p}}}. \end{aligned} \tag{6.40}$$

Using the internal energies in Eq. 6.40 and neglecting the spatial dependence in Eq. 6.11, we calculate the time evolution of a condensate prepared in the para- state at various densities. As discussed in Sec. 6.1, when $n_{\mathrm{ini}} > n_{\mathrm{c}}$, the initial p-Ps condensate is no longer a ground state and the system will undergo strong spin-mixing.

We demonstrate this by considering a system prepared in a predominantly para- state, with a small admixture of ortho-. In particular, our initial state consists of equal populations of the three ortho- states, each with population fraction $\sim 10^{-7}$. The phases were determined using imaginary time evolution to find the lowest energy state consistent with this population distribution. We then numerically integrate

Eqs. 6.11 starting with this initial state.

Figs. 6.7 (a) and (b) show the time evolution of a condensate at $n_{\rm ini} = 10^{20}$ cm^{-3} at different time scales. Figure (a), which depicts a shorter timescale, reveals a quasi-periodic oscillation pattern caused by the spin-mixing. As time progresses, the amplitude of the oscillations decreases due to the decay term introduced in the GP equation. As t becomes comparable to $\tau_{\rm p}$, both the para- population and its population exchange with the ortho- state begin to disappear. However, the total population does not simply decay away through the para- state. It evolves into a pure o-Ps state that is decoupled from the para- annihilation process. About one third of the population is trapped in the ortho- sector as $t > 1\,$ns. This behavior is qualitatively different from that observed in the rate-equation approach, where there is no phase coherence of population amplitudes. In contrast to the classical rate equations, in the GP equation, the spin-mixing interactions depend on both the reactant and product densities, and ortho–para conversion is suppressed if either density is small [99].

In the calculations discussed above, we assumed all components of the condensate occupy the same homogeneous spatial profile. We now discuss more realistic cases, in which this assumption is not made. First we consider a one-dimensional quasi-homogeneous condensate, in which each wavefunction is modulated at $t = 0$ with random spatial noises.

In particular, we assume the transverse directions are tightly confined in a box smaller than the healing length, ξ. We then define a new 1D pseudo-potential constant such that the interaction energy per particle is the same as a 3D system

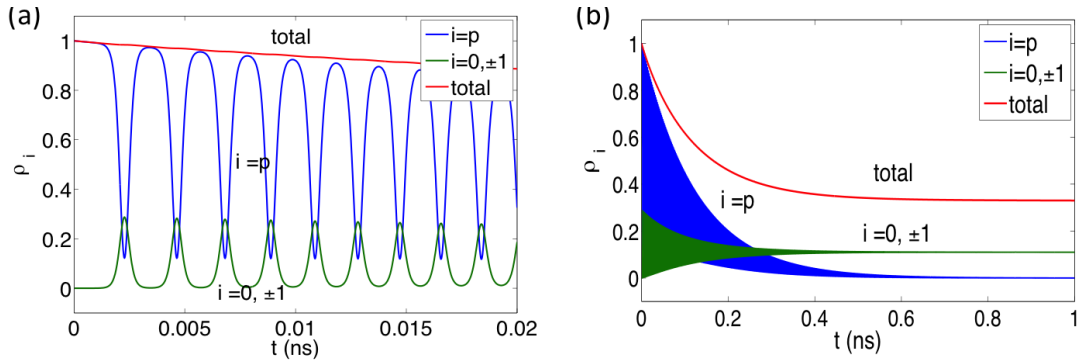

Figure 6.7: Population evolution of a mixed Ps condensate undergoing both spin mixing and Ps annihilation over timescales of (a) 0.02 ns and (b) 1 ns. The system is prepared in $|\mathrm{p}\rangle$ at a density of $n_{\mathrm{ini}} = 10^{20}$ cm^{-3}. The short-scale evolution shows rapid oscillations due to spin mixing. The long-time evolution reveals a prominent decay behavior, but with about one third of the total population trapped in the ortho- sector.

with density n_{ini} after integrating over the transverse directions. We prepare an initial state that corresponds to the state chosen above, defined on a uniform grid of 1000 points. Then, at each grid point m we multiply the wave function of each component i by a factor of $1 + \eta_{m,i}$, where $\eta_{m,i}$ is a complex Gaussian random number with $\langle \eta^*_{m,i}\eta_{m',i'}\rangle = 2\sigma^2\delta_{m,m'}\delta_{i,i'}$, $\langle \eta_{m,i}\eta_{m',i'}\rangle = \langle \eta_{m,i}\rangle = 0$, and $\sigma = 0.01$. We emphasize that this propagation is not intended to simulate the effects of dissipation beyond that associated with electron-positron annihilation. It amounts to applying a small relative change to the populations of the initial state discussed above, in order to test the sensitivity of time evolution to initial conditions.

We find that when $n_{\mathrm{ini}} > n_{\mathrm{c}}$, the initial spatial noise grows rapidly in time into a regime of highly irregular evolution. For example, we consider the evolution of a condensate as prepared above, at a density of $n_{\mathrm{ini}} = 10^{20}\mathrm{cm}^{-3}$, as shown in Fig. 6.8. All species decay with about the same time constant $\tau \approx 4\tau_p$, and there is no persistence of a trapped o-Ps population that occurs in the absence of noise. In

this regime, spin structures of size comparable to the healing length rapidly collide and inter-convert. In Fig. 6.9, we can see the noise grows substantially during one cycle of spin mixing oscillation, giving rise to irregular spatial structure. This irregular spatial evolution guarantees that there are always regions where o-Ps can be converted to p-Ps, and then decay. As suggested by Fig. 6.8, the evolution of the relative populations is qualitatively similar to that found in the rate equation approach. The overall density also decays on a timescale set by $\sim 4\tau_{\rm p}$ instead of $\tau_{\rm p}$. This is because the irregular spatial variation plays a role similar to that of phase averaging in an incoherent mixture.

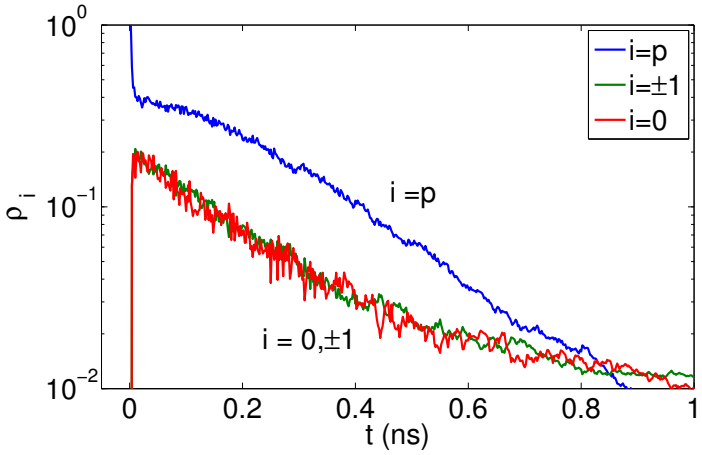

Figure 6.8: Time evolution of a mixed condensate of initial density $n_{\rm ini} = 10^{20}$ cm^{-3} prepared in the para- state with random spatial noise. At short times, spin-mixing drives the populations toward the equilibrium distribution. Then, all species decay exponentially at the same rate, given approximately by $4\tau_p$, subject to background fluctuations. Due to the presence of noise, no population is trapped in the ortho-sector. The population evolution is qualitatively similar to that obtained from the rate equations (see Fig. 6.6 (b)) with fitted decay lifetimes equal to $\tau_{\rm eff}/\tau_{\rm p} = 4.3$, 4.3, 4.3, 3.7 for states $i = 1, 0, -1, {\rm p}$, respectively.

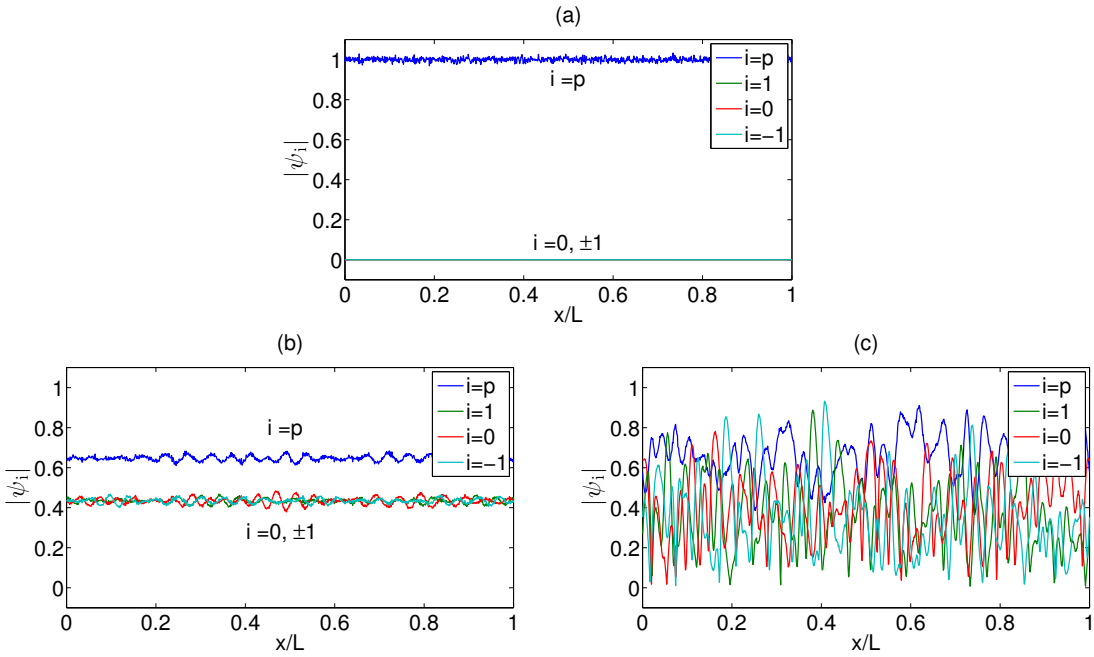

Figure 6.9: The wavefunction amplitudes $|\psi_i(x)|$ recorded at (a) $t = 0$ ns, (b) $t = 0.002$ ns and (c) $t = 0.004$ ns for the evolution in Fig. 6.8. The system size L is selected such that $L \sim 200\xi$. The noise grows significantly within one cycle of spin-mixing oscillation. At $t = 0$ ns, we introduce small random noises to each of the initial wavefunctions $\psi_i(x)$. At $t = 0.002$ ns, $|\psi_i(x)|$ follows the evolution pattern of Fig. 6.7 and is about uniform with small spatial fluctuations. At $t = 0.004$ ns, the background fluctuations begin to dominate and destroy the uniform spatial structures. By this time, the irregular spin structures have formed such that the system undergoes local spin mixing.

6.2.3 Stability analysis using the Bogoliubov-de Gennes equations

The short-time amplification of the noise in the GP evolution can be understood by solving the Bogoliubov-de Gennes (BdG) equations [92], which are derived as follows. We start by introducing small variations $\delta\psi$ to the spinor wavefunction

$$\psi_j(\mathbf{r}, t) = \left(\psi_j^0(\mathbf{r}) + \delta\psi_j(\mathbf{r}, t)\right) e^{-i\mu t/\hbar}, \tag{6.41}$$

where j is the conventional spin index used in this chapter, and ψ_j^0 corresponds to a reference spinor state. The variation $\delta\psi_j$ can take the form

$$\delta\psi_j\left(\mathbf{r},t\right)=u_j\left(\mathbf{r}\right)e^{-i\varepsilon t/\hbar}+v_j^*\left(\mathbf{r}\right)e^{i\varepsilon t/\hbar}. \tag{6.42}$$

When the system size is much greater than the healing length, we can assume plane wave solutions of the type $u_j\left(\mathbf{r}\right)\equiv u_j\left(\mathbf{k}\right)e^{-i\mathbf{k}\cdot\mathbf{r}}$ and $v_j\left(\mathbf{r}\right)\equiv v_j\left(\mathbf{k}\right)e^{-i\mathbf{k}\cdot\mathbf{r}}$, and $\varepsilon\equiv\varepsilon\left(\mathbf{k}\right)$, where $\mathbf{k}$ is the characteristic wavevector of the plane wave. To calculate the fluctuations u,v we substitute Eq. 6.41 into the coupled GP equations (Eq. 6.11), linearize to first order in $\delta\psi$, and then collect terms whose phases rotate as $e^{-i\varepsilon t/\hbar}$. We obtain the Bogoliubov-de Gennes equations for u_j and v_j

$$\begin{aligned}
H_{ji}u_i^{(\lambda)}\left(\mathbf{k}\right)+H_{ji}^{'}v_i^{(\lambda)}\left(\mathbf{k}\right) &= \varepsilon^{(\lambda)}\left(\mathbf{k}\right)u_j^{(\lambda)}\left(\mathbf{k}\right)\\
H_{ji}^{'*}u_i^{(\lambda)}\left(\mathbf{k}\right)+H_{ji}^{*}v_i^{(\lambda)}\left(\mathbf{k}\right) &= -\varepsilon^{(\lambda)}\left(\mathbf{k}\right)v_j^{(\lambda)}\left(\mathbf{k}\right)
\end{aligned} \tag{6.43}$$

where $j,\ i=1,\ 0,\ -1$ and p are the indices for spin states, and λ is a band index whose meaning will presently become clear. The matrices in Eq. 6.43 are given by

$$\begin{aligned}
H_{ji} &= \left(\frac{\hbar^2k^2}{2m}-\mu\right)\delta_{ji}+g_0\psi_j\psi_i^*(1+\delta_{ji})+\frac{\partial^2F}{\partial\psi_j^*\partial\psi_i},\\
H_{ji}^{'} &= g_0\psi_j\psi_i+\frac{\partial^2F}{\partial\psi_j^*\partial\psi_i^*},
\end{aligned} \tag{6.44}$$

where

$$F\equiv\frac{g_1}{2}\left|2\psi_1\psi_{-1}-\psi_0^2+\psi_{\mathrm{p}}^2\right|^2, \tag{6.45}$$

and in Eqs. 6.44, 6.45 only, we drop the superscript 0 in ψ_j^0.

For each given value of $\mathbf{k}$, Eq. 6.43 is an eight-dimensional generalized eigenvalue problem. This is because the four spin indices are replicated in the four-dimensional matrices H_{ji} and H'_{ji}. Thus for a given value $\mathbf{k}$, Eq. 6.43 has eight eigenvalues $\varepsilon^{(\lambda)}(\mathbf{k})$ where λ is an eight-fold index. It can be shown that the eigenvalues occur in pairs such that if ε is an eigenvalue, then so is $-\varepsilon$. The eigenvalues ε may in general be complex numbers, but only real eigenvalues correspond to stable fluctuations about the reference state ψ^0. A complex eigenvalue indicates an instability of the GP equations. At short times the amplitude of the instability grows exponentially with time constant given by $\hbar/\mathrm{Im}[\varepsilon]$.

We find that when $n > n_\mathrm{c}$, a condensate initially in the para- state has complex BdG eigenvalues, $\varepsilon = \varepsilon_\mathrm{R} + i\varepsilon_\mathrm{I}$. If $\varepsilon_\mathrm{I} \neq 0$, the mode amplitude will grow exponentially until the nonlinear terms in the GP equations dominate. This regime is characterized by significant spatial irregularity on a short length scale. The condensate therefore is composed of many spatial modes, and correspondingly has a wide distribution in momentum space. This may reduce the γ-ray yield, as studied in [27]. We characterize the instability of a condensate by the largest value of ε_I of any of its BdG modes, $\varepsilon_\mathrm{I}^\mathrm{max}$. Fig. 6.10 shows the dependence of $\varepsilon_\mathrm{I}^\mathrm{max}$ as a function of kinetic energy and p-Ps density. It shows that the unstable modes appear when $n_\mathrm{ini} > n_\mathrm{c}$, which is the same condition for the occurrence of spin mixing. Thus, when spin mixing is most pronounced, there is also a propensity for spatial inhomogeneity of the system.

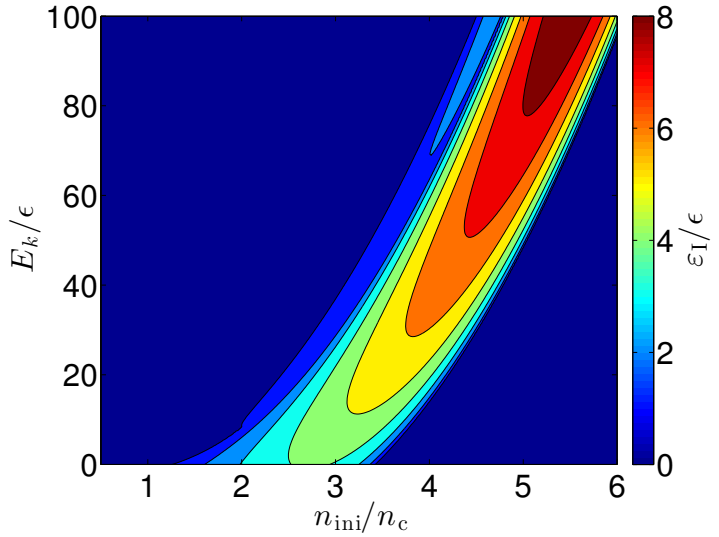

Figure 6.10: Imaginary part of the energy, $\varepsilon_{\rm I}$, of the most unstable BdG mode as a function of condensate density $n_{\rm ini}$ and kinetic energy E_k. We express these variables in dimensionless form as indicated by the axis labels. For $n_{\rm ini} < n_{\rm c}$, all BdG modes are stable, i.e. the imaginary part vanishes. When $n_{\rm ini}$ increases above $n_{\rm c}$, the low energy (long wavelength) modes become unstable. For any value of $n_{\rm ini} > n_{\rm c}$, there is an energy band of instability, whose width is about four orders of magnitudes greater than the natural γ-ray linewidth ($\Delta E \sim 10^4 \hbar/\tau_{\rm p}$).

6.2.4 Optimizing γ-ray yield

It has been shown that [100] the formation of a Ps BEC corresponds to large p-Ps stimulated annihilation cross-section. For zero temperature BECs, a macroscopic number of Ps atoms occupy the zero-momentum mode. This results in a small energy uncertainty and a narrow γ-ray line-width determined by the natural lifetime: $\Delta E \sim \hbar/\tau_{\rm p} = (1/2)\ \alpha^5 m_{\rm e} c^2$, where α is the fine structure constant [27]. As the population of states in $\mathbf{p} \neq 0$ modes increases, both the energy uncertainty and the γ-ray line-width will increase. This will decrease the resulting coherent γ-ray yield. As discussed in the previous section, the instability associated with the spin mixing would lead to a broad uncertainty in kinetic energies that is about four

orders of magnitude greater than the natural γ-ray linewidth (see Fig. 6.10). The corresponding γ-ray yield would be greatly reduced. To avoid this effect, it is crucial to conduct the experiment such that the condensate is composed primarily of the zero momentum mode.

Original proposals suggested that lasing can be initiated by converting an ortho- condensate into a para- condensate by application of a radio frequency pulse [31]. For dense condensates, this procedure could result in a spread of momentum states due to the spatial instability demonstrated above. However, if the para-fraction is kept sufficiently small by properly manipulating the duration and strength of external pulses, this instability can be avoided, and the γ-ray yield maximized. In the following, we model a polarized Ps BEC subject to external magnetic fields. We provide two ideal schemes for ortho- to para- conversion, and subsequent γ-ray emission, without exciting spin-mixing instabilities. To calculate the final gain of a γ-ray laser, it is necessary to consider the actual construction of a laser, the geometry structure of the cavity, and how the stimulated annihilation is initiated with respect to that structure. Future simulations can be made with the inclusion of these factors.

We now consider the effect of an external magnetic field $\mathbf{B} = (B_x, B_y, B_z)$ applied to a Ps atom. Using the same basis as Eq. 6.11, the atom-field interaction

is given by

$$H_{\rm ext} = -\mu_{\rm e} \begin{pmatrix} 0 & 0 & 0 & \frac{-B_x+iB_y}{\sqrt{2}} \\ 0 & 0 & 0 & B_z \\ 0 & 0 & 0 & \frac{B_x+iB_y}{\sqrt{2}} \\ \frac{-B_x-iB_y}{\sqrt{2}} & B_z & \frac{B_x-iB_y}{\sqrt{2}} & 0 \end{pmatrix}, \tag{6.46}$$

where $\mu_{\rm e}$ is the magnetic moment of the electron [101]. This matrix shows that a field in either the $\hat{x}$ or $\hat{y}$ direction couples the $|\pm 1\rangle$ states with $|{\rm p}\rangle$ with equal probability. A field in the $\hat{z}$ direction induces coupling only between $|0\rangle$ and $|{\rm p}\rangle$. In order to couple the state $|\pm 1\rangle$ to the state $|{\rm p}\rangle$, we can use circularly polarized light. We assume an rf pulse where $B_x = B\cos(\omega_0 t)$, $B_y = \pm B\sin(\omega_0 t)$, and $B_z = 0$, where ω_0 is the frequency of the rf field and $+(-)$ denotes right(left)-hand polarization. If $\hbar\omega_0 \sim \epsilon$, we can invoke the rotating wave approximation, and eliminate the counter rotating terms. In this approximation, left(right)-handed polarization will couple only the state $|1\rangle$ ($|-1\rangle$) to the state $|{\rm p}\rangle$. Note that if linear polarization were used, i.e., $B_x = B\cos(\omega_0 t)$ and $B_y = B_z = 0$, then half of the population would be trapped in a "dark state" of the coupling Hamiltonian, and at most half of the ortho- states would be converted to para-.

Below the critical density, a strong γ-ray beam can be created by converting the entire population from $|1\rangle$ to $|{\rm p}\rangle$ with a single strong circularly polarized pulse. However, for $n_{\rm ini} > n_{\rm c}$, care must be taken to avoid the spin-mixing instabilities discussed in the previous section. An instability can occur if a sufficiently large population is converted to the para- state. Therefore, it is necessary to design a

pulse sequence that keeps the para- fraction small.

To do this, note that for sufficiently small para- population, spin-mixing effects are frozen out and the spin evolution will be dominated by the Rabi oscillations induced by the rf pulse. To choose an appropriate pulse sequence, we consider a homogeneous two state model, consisting of only $|1\rangle$ and $|\mathrm{p}\rangle$, and the density-density terms. The effective GP equation in the rotating frame is then

$$i\partial_t \begin{pmatrix} \psi_1 \\ \\ \psi_\mathrm{p} \end{pmatrix} = \begin{pmatrix} 0 & \Omega \\ \\ \Omega & -i\gamma + \delta + g_1 n_\mathrm{p}/\hbar \end{pmatrix} \begin{pmatrix} \psi_1 \\ \\ \psi_\mathrm{p} \end{pmatrix} \tag{6.47}$$

where $\Omega = -\mu_e B/\hbar$, $\gamma = 1/2\tau_\mathrm{p}$, $\hbar\delta = \epsilon - \hbar\omega_0$ and we have neglected the finite ortho- lifetime since it will not be relevant on the timescales of the system. In what follows, we assume that we are on rf resonance, i.e., $\delta = 0$, unless otherwise stated.

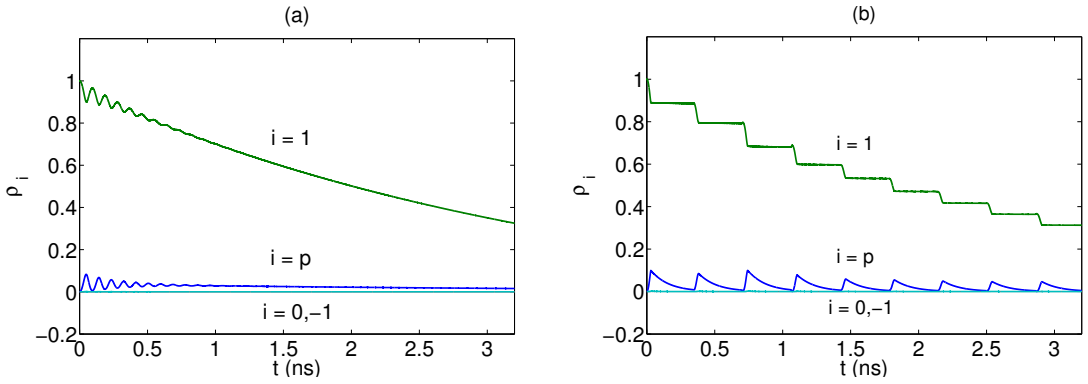

Figure 6.11: Time evolution of a polarized Ps condensate of density $10^{20}\mathrm{cm}^{-3}$ (a) under a single circularly-polarized rf pulse of frequency $\omega = \epsilon/\hbar$ and field strength $B = 1/\hbar\mu_\mathrm{e}\tau_p$ (b) under a series of circularly-polarized rf pulses of the same frequency but with field strength $B = 0.1$ T. In both cases, Ps atoms are transferred from $|1\rangle$ to $|\mathrm{p}\rangle$ using B fields that are chosen to restrict the maximal n_p to be less than $n_\mathrm{c} \approx 0.12 n_\mathrm{ini}$. Since $n_\mathrm{p} < n_\mathrm{c}$, spin-mixing and the corresponding instability do not appear throughout the process.

We first ignore the effects of interactions by setting $g_1 = 0$, and express Eq. 6.47 as an eigenvalue problem by assuming time dependence of the form

$\psi \sim e^{-i\omega_\pm t}\chi_\pm$. The solution is characterized by two eigenmodes $\chi_\pm$ with eigenvalues $\omega_\pm = \pm\omega - i\gamma/2$, where $\omega = \sqrt{\Omega^2 - (\gamma/2)^2}$. The real part of $\omega_\pm$ is responsible for the oscillatory behavior of the modes, and the imaginary part contributes to the exponential decay. Solving for the initial conditions $\psi_1(0) = \sqrt{n_{\rm ini}}$ and $\psi_{\rm p}(0) = 0$, the para- population is given by

$$n_{\rm p}(t) = n_{\rm ini} e^{-\gamma t} \sin^2(\omega t)\, \Omega^2/\omega^2. \tag{6.48}$$

The evolution is characterized by two regimes. In the under-damped regime, where $\Omega > \gamma/2$ and ω is real, population can oscillate between $|1\rangle$ to $|{\rm p}\rangle$ with frequency ω and an overall decay rate γ.

In the overdamped regime where $\Omega < \gamma/2$, ω becomes imaginary and Eq. 6.48 can be equivalently expressed as $n_{\rm p}(t) = n_{\rm ini} e^{-\gamma t} \sinh^2(|\omega| t)\, \Omega^2/|\omega|^2$. The para- fraction rises to a maximum value of $n_{\rm p} = n_{\rm ini} \exp[-\gamma/|\omega| \cosh^{-1}(\gamma/2\Omega)]$ before decaying away exponentially with slower decay rate given approximately by $\gamma - 2{\rm Im}[\omega]$.

If nonlinear interactions are included, i.e., $g_1 \neq 0$, we find small oscillations in either regime. These can be understood by replacing the interaction term $g_1 n_{\rm p}$ with an effective detuning $\delta_{\rm eff} = g_1 \bar{n}_{\rm p}/\hbar$, where $\bar{n}_{\rm p}$ is the para- density time averaged over the short oscillations. With this replacement, the eigenvalues gain a real component which allows the corresponding modes to oscillate. At longer times, this mode damps out and the long-time behavior is well approximated by the non-interacting model. Note that these oscillations can be reduced by choosing the detuning such that $\delta \approx -\delta_{\rm eff}$.

To test the efficacy of this pulse sequence, we perform a simulation using the previously described quasi-1D method applied to a condensate initially prepared in $|1\rangle$ at a density of $n_{\rm ini} = 10^{20}$ cm^{-3}. The circularly polarized rf field is added according to Eq. 6.46, without invoking the rotating wave approximation. A small random noise is added as in the previous section. Two pulse forms are considered. In Fig. 6.11(a), a continuous rf pulse is applied such that the maximum para- population is set at about $n_{\rm c}$. In this case the solution of Eq. 6.47 is in the under-damped regime, in which the para- fraction grows, and then decays as described above. Rapid oscillations are present at short times before quickly decaying away. In Fig. 6.11(b), a series of short pulses are applied to pump the para- population. Between every two pulses is a period of no rf fields during which the system undergoes coherent decay. The field strength is 0.1 T as suggested in [31] and the pulse durations are selected such that $n_{\rm p}$ does not exceed $n_{\rm c}$. In both pulse sequences, the absolute density of the para- condensate is kept below the critical density, and no spin-mixing instabilities form. This comes at the cost of a longer overall decay time.

6.3 Conclusions

In summary, we have considered the effects of interactions in a BEC of positronium atoms. We first derived the many-body interaction Hamiltonian describing the interactions of the ortho- (triplet) and para- (singlet) sectors. We found that the interaction Hamiltonian has an $O(4)$ symmetry. The ortho-para- energy difference breaks this symmetry to $SO(3)$, that of the triplet sector. We calculate

the ground state for a uniform, homogeneous system. Below the critical density $n_c = \epsilon/2g_1 \approx 1.2 \times 10^{19}$ cm^{-3}, the ground state is entirely polarized in the para- state. Above the critical density, the ground state contains a non-zero fraction of the ortho- state. We then consider the effects of interactions on spin dynamics for a uniform system prepared in a non-stationary state. We find that the critical density again characterizes the density for which spin mixing between the ortho- and para- sectors becomes significant.

We then consider how the effects of spin mixing will affect the use of a Ps BEC as a γ-ray laser. We develop a rate equation approach to describe an incoherent thermal mixture, including the effects of spontaneous electron-positron annihilation. When the spin mixing is strong the entire system decays with a lifetime approximately four times the lifetime of the para- state. We then model a coherent condensate using a 1D GP equation, and find that there are significant spin-mixing effects above the critical density. This spin mixing induces high frequency spatial modulations, which have the effect of averaging over populations in a way that resembles phase averaging in an incoherent system. The evolution and decay of the populations is qualitatively similar to the rate equation approach. Furthermore, the large spread of kinetic energies of the cloud will reduce the yield of a γ-ray laser. This suggests that a straightforward preparation of a high density para- condensate will not result in an optimal γ-ray yield.

Finally, we consider an experimentally relevant setup where an initially spin-polarized beam of positrons is used to prepare a Ps BEC that is initially spin polarized in the $|1\rangle$ state. We consider the effect of an external rf field used to convert

the initial state to the para- state for the production of coherent γ rays. For a circularly polarized field with frequency that is nearly resonant with the internal energy splitting of the ortho- and para- states, the ortho- condensate can be fully converted to the para- condensate. If the initial density is above n_c, a modified pulse sequence can be used to avoid significant para- population, at the cost of a longer overall timescale. This suggests that for large densities, the γ-ray yield is optimized by transferring population more slowly. This comes at the cost of a lower γ-ray peak amplitude, but spread over a longer time.

Chapter 7: Summary and Future Outlook

We extensively study a laboratory BEC that implements a sonic black hole in Chapter 3. We propose that the observed features in the laboratory condensate is due to a Bogoliubov-Čerenkov mode generated at the white-hole horizon (WH), which stimulates the creation of a Hawking pair at the black-hole horizon (BH). Based on this mechanism, we modify the experimental parameters, and find a regime where sharper signal of Hawking radiation can be obtained. We observe a clear signal of pair creation which agrees with the prediction based on the stimulated mechanism, and the BdG theory of linearized modes. This modified parameter regime, along with the stimulated Hawking mechanism, may be useful in detecting Hawking radiation in future laboratories.

A more recent experiment at Technion reported the observation of correlated Hawking pair from a density-density correlation function [18]. This experiment took a very similar step-sweeping procedure as in the previous experiment [1]. The difference is that the correlated pair was detected at an earlier timeframe at which a WH may just form. We are currently in a preliminary stage of simulating this experiment. We are investigating the roles of shot-to-shot variations in the atom number, which may be relevant in interpreting the observed correlated features as

in the case of Chapter 4.

Furthermore, it is also likely to realize the analog Hawking effect in a ring-shaped condensate [23, 24]. In Chapter 5, we create phonon wavepackets by modulating a potential barrier in the ring. If a transonic flow is formed in the ring, we can develop similar schemes to launching phonon wavepackets to the transonic region, and trigger stimulated pair creation at the BH. This can be an alternative approach for the observation of stimulated Hawking radiation.

Lastly, in the chapter of spinor Ps condensates, we find a critical density for the p-Ps fraction beyond which strong spin mixing between o-Ps and p-Ps would occur, and suppress the coherent emission of γ rays. We propose a scheme of applying an external field to control the p-Ps density and the yield of coherent γ ray. However, some aspects of the system are simplified: (i) the system is considered as homogeneous (before introducing the spatial noise) and one dimensional; (ii) the Ps annihilation is treated phenomenologically in the GP equation. In the future, we would like to take into account more realistic aspects of the system, such as the role of the silicon cavity and its geometry, and develop a model that can more accurately describe the stimulated annihilation process, and the emission of coherent γ ray.

Appendix A: Numerical procedures for Chapter 3

A.1 Characterization of the experimental condensates and description of simulation procedures

In this appendix, we introduce the basic procedures to simulate the experiment. We use the time–dependent Gross–Pitaevskii (GP) equation to determine the condensate wavefunction $\Psi(\mathbf{r},t)$,

$$i\hbar\frac{\partial\Psi(\mathbf{r},t)}{\partial t} = \left(T(\mathbf{r})+U(\mathbf{r})+g_{3\mathrm{D}}N\left|\Psi\right|^2\right)\Psi(\mathbf{r},t), \tag{A.1}$$

where $T(\mathbf{r})$ and $U(\mathbf{r})$ are the kinetic and potential energy operators, N is the number of condensate atoms, $g_{3\mathrm{D}}=4\pi\hbar^2a/m$ where a is the s–wave scattering length, and m is the mass of a condensate atom. For a cylindrically symmetric system, the potential depends only on radial coordinate ρ and axial coordinate x, $U(\mathbf{r})=U(\rho,x)$; and $T(\mathbf{r})$ can be expressed as

$$T(\mathbf{r})=-\frac{\hbar^2}{2m}\left(\frac{\partial^2}{\partial\rho^2}+\frac{1}{\rho}\frac{\partial}{\partial\rho}+\frac{\partial^2}{\partial x^2}+\frac{\partial^2}{\partial\phi^2}\right). \tag{A.2}$$

Regarding the ground state of the BEC, the azimuthal coordinate ϕ in the wavefunction can be suppressed, such that $\Psi(\mathbf{r},t)=\Psi(\rho,x,t)$.

For the experiment of interest [1], the trap potential is formed by a Gaussian

laser beam:

$$U(\rho, x) = U_0 \left[1 - \left(\frac{w_0}{w\,(x)} \right)^2 \exp\left(\frac{-2\rho^2}{w^2\,(x)} \right) \right]. \tag{A.3}$$

where U_0 is the trap strength proportional to the peak laser intensity and

$$w(x) = w_0 \sqrt{1 + \left(\frac{x}{x_0} \right)^2}, \qquad x_0 = \frac{\pi w_0^2}{\lambda}. \tag{A.4}$$

where λ and w_0 denote the wavelength and the waist of the laser beam, respectively. According to [1], $\lambda = 812$ nm, $w_0 = 5$ mm, and the radial frequency is $\omega_\rho = 123$ Hz. This corresponds to a trap tightly confined in the radial direction ρ, and elongated along the axial direction x. Expanding the trap at $x = \rho = 0$ to second order, we obtain an approximate harmonic potential:

$$U(\rho, x) \approx \left(\frac{2U_0}{w_0^2} \right) \rho^2 + \left(\frac{U_0}{x_0^2} \right) x^2 \equiv \frac{1}{2} m\omega_\rho^2 \rho^2 + \frac{1}{2} m\omega_x^2 x^2. \tag{A.5}$$

from which the trap strength can be estimated by $U_0 = (1/4) m\omega_\rho^2 w_0^2 \approx 39\,k\,\mathrm{nK}$, where k is the Boltzmann constant.

When the system is tightly-confined in the radial direction, such that the integrated density $n(x)$ in the axial direction satisfies $an \ll 1$, it can be viewed as quasi-one-dimensional [102]. Were the potential cylindrically symmetric, one could approximate the wavefunction in the radial direction by the solution of a harmonic oscillator, such that

$$\Psi(\mathbf{r}, t) \approx \Phi(\rho) \Psi_{1\mathrm{D}}(x, t), \tag{A.6}$$

where the radial wavefunction is $\Phi(\rho) = \exp\left[-\rho^2/\left(2d^2\right)\right]/(d\sqrt{\pi})$, $d = \sqrt{\hbar/\left(m\omega_\rho\right)}$, and $\Psi_{1\mathrm{D}}(x, t)$ is the axial wavefunction. Integrating the GP equation in Eq. A.1

over ρ would then yield a 1D GP equation for $\Psi_{1\mathrm{D}}(x,t)$, with an effective interaction coefficient $g_{1\mathrm{D}} = g_{3\mathrm{D}} m\omega_\rho/h$:

$$\begin{aligned} i\hbar\frac{\partial\Psi_{1\mathrm{D}}(x,t)}{\partial t} &= \left(-\frac{\hbar^2}{2m}\frac{\partial^2}{\partial x^2} + U_{1\mathrm{D}}(x) + \hbar\omega_\rho\right)\Psi_{1\mathrm{D}}(x,t) \\ &+ g_{1\mathrm{D}} N\left|\Psi_{1\mathrm{D}}(x,t)\right|^2 \Psi_{1\mathrm{D}}(x,t). \end{aligned} \tag{A.7}$$

where $U_{1\mathrm{D}}(x)$ is the axial trap.

A.1.1 Solution of the time–dependent 1D GP equation

The time-dependent 1D GP equation is solved by using the split-step Crank-Nicholson algorithm [103] on a 1D spatial grid of 320 μm with 4800 points, first propagating in imaginary time to obtain the initial stationary condensate, then propagating in real time with the given initial state to simulate the dynamics. To simulate the step-sweeping experiment [1], we use a step potential $U_{\mathrm{step}}(x,t)$, which takes the form

$$U_{\mathrm{step}}(x,t) = -U_{\mathrm{s}}\Theta(x_{\mathrm{s}}(t) - x), \tag{A.8}$$

where Θ is Heaviside's step function; U_{s} is the step strength, which takes the values of $U_{\mathrm{s}}/k = 3$ nK and 6 nK; $x_{\mathrm{s}}(t)$ represents the step location, moving at a constant speed, $v_s = 0.21$ mm/s.

A.1.2 Growing standing wave, spacetime portrait, and frequency spectrum from a 3D simulation

To test our findings from the 1D simulation, we simulate the same step-sweeping experiment using the 3D GP equation, with the potential Eq. A.3, as-

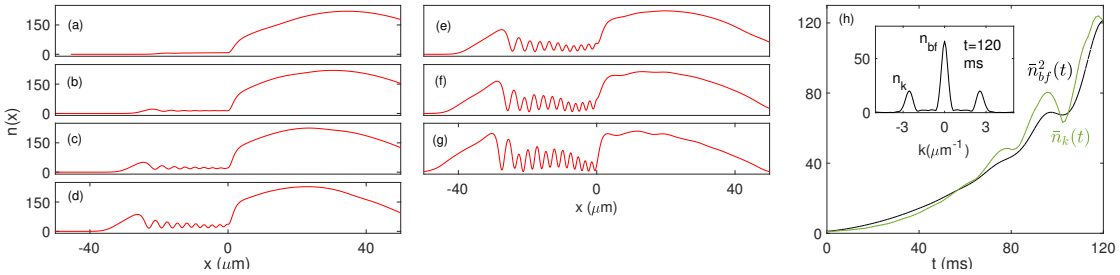

Figure A.1: 3D GP simulation of the condensate. (a-g) Evolution of integrated density from a 3D simulation at 20 ms intervals with step $U_s/k = 5$ nK, scaled by a common factor to match experiment, and viewed in the moving frame where $x = 0$ defines the step edge. (h) Simulated growth of the standing-wave pattern in the supersonic region for $U_s/k = 5$ nK. Green: normalized standing-wave amplitude $\bar{n}_k(t)$, $\bar{n}_k(t) = n_k(t)/n_k(0)$, for which $\ln[\bar{n}_k(120)] \sim 4.8$. Dashed black: the square of background density, $\bar{n}_{\rm bf}(t)$, scaled to match the final standing-wave amplitude, $\bar{n}^2_{\rm bf}(t) = n^2_{\rm bf}(t)[\bar{n}_k(120)/n^2_{\rm bf}(120)]$. The growths of $n_{\rm bf}$ and n_k are determined from a spatial WFT of $n(x)$ at $x = -12.5$ μm.

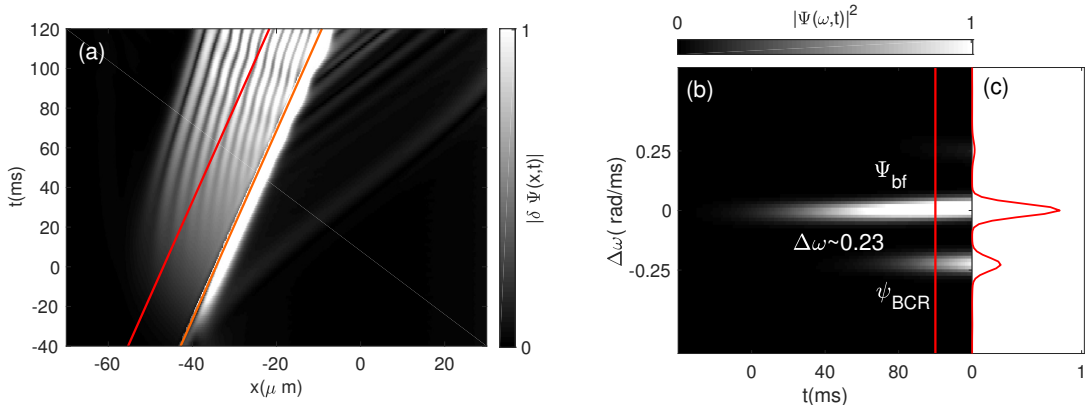

Figure A.2: Spacetime diagram and WFT frequency spectrum for the 3D simulation. Panel (a): time evolution of $|\delta\Psi(x,t)|$. Panel (b): windowed Fourier spectrum evaluated along the red line in (b); panel (c) is the cut-through of the spectrum at $t = 100$ ms. Note that the Doppler-shifted frequency $\Delta\omega_{\rm pair} \sim 0.23$ rad/ms, which is about twice the value from the 1D GPE.

suming the condensate shares the axial symmetry of the potential..

Figs. A.1(a-g) shows the integrated density profiles with a potential step, $U_{\rm s}/k = 5$ nK, which is adjusted slightly to match the cavity size with the experiment. The growth of the standing wave amplitude, $\bar{n}_k$, and that of the background density, $\bar{n}_{\rm bf}$, are shown in Fig. A.1(h). The standing wave grows by $\sim \exp(4.8)$,

which is greater than the 1D simulation ($\sim \exp(4.4)$), but the growth relation, $\bar{n}_k \propto \bar{n}_{\rm bf}^2$, are preserved in the 3D simulation.

Similarly, we calculate the spacetime portrait and the local frequency spectrum using the GP wavefunction at the center of the radial trap, $\rho = 0$. The spacetime portrait in Fig A.2(a) shows very similar features as those in the 1D simulation, including the standing wave parallel to the WH, and the stimulated Hawking pair. The WH recession can also be seen in the portrait, which gives rise to a Doppler-shifted BCR frequency in the WFT spectrum in Fig A.2(b-c), $\Delta\omega \sim 0.23$ rad/ms.

Although there are some quantitative differences with the 1D simulation, all the qualitative features found in the 1D GPE are preserved here: (i) the growth relation between the standing wave and the background density, (ii) the stimulated HR pair by the BCR, and (iii) the Doppler shift due to the WH recession.

A.2 Windowed Fourier transform

Here we summarize the basic ideas of the windowed Fourier transform (WFT), and explain our use of it. In A.2.1, we give the definition of WFT used here, and provide a few basic examples to show how it can resolve spectral information on non-stationary phenomena. In A.2.2, we describe the the application of the WFT to the determination of flow and sound speeds, $v(x)$ and $c(x)$, in inhomogeneous media. In A.2.3, we discuss calculations of the wavevector and frequency spectra displayed in Fig. 3.13(a-b), and the additional spectra that distinguish the partner and BCR modes. In A.2.4, we show the windowed frequency spectrum for the experimental

regime, and a comparison with the dispersion relation.

A.2.1 Definition and examples

A windowed Fourier transform [38] $f(k,x)$ of a function $f(x)$ is defined as:

$$f(k,x) = \int_{-\infty}^{\infty} dy\, f(y) w(y-x;D) e^{-iky}, \tag{A.9}$$

where $w(y-x;D) = \exp(-(y-x)^2/D^2)/\left(\sqrt{\pi}D\right)$ is a Gaussian window function of width D. With the filtering of the window, the transformed function $f(k,x)$ constitutes a local Fourier transform of $f(x)$, capturing features that vary on length scales much smaller than D. For a plane wave with wavevector q and amplitude f_q , $f(x) = f_q \exp(iqx)$, the transformed function is $f(k,x) = f_q \exp(-(k-q)^2(D/2)^2)$: a Gaussian in k-space, centered at $k = q$ with width $2/D$ and peak amplitude f_q.

Suppose now that $f(x) = f_q(x)\exp(iqx)$, where $f_q(x)$ has weak dependence on x, and can be adequately approximated near a point x_0 by

$$f_q(x) = f_q(x_0) + f_q'(x_0)(x - x_0). \tag{A.10}$$

Then for sufficiently small values of D, the WFT of $f(x)$ near $x = x_0$ is approximately

$$\begin{aligned} f(k,x_0) &\approx f_q(x_0) e^{-(k-q)^2(D/2)^2} \\ &+ f_q'(x_0)\, i\frac{k-q}{2} D^2\, e^{-(k-q)^2(D/2)^2}. \end{aligned} \tag{A.11}$$

Note that the second term vanishes at the peak position $k = q$, so that $f(q,x_0) \approx f_q(x_0)$.

Finally, let $f(x)$ be composed of a number of such slowly–varying modes,

$$f(x) = \sum_n f_{q_n}(x) e^{iq_n x}, \tag{A.12}$$

so that Eq. A.11 becomes

$$\begin{aligned} f(k, x_0) \;\; &\approx \;\; \sum_n \left[f_{q_n}(x_0) + f'_{q_n}(x_0) \left(i \frac{k - q_n}{2} D^2 \right) \right] \\ &\quad \times e^{-(k-q_n)^2 (D/2)^2}. \end{aligned} \tag{A.13}$$

In k–space, each mode presents a Gaussian distribution centered on its respective q_n, whose peak value of $f(q_n, x_0)$ defines the local mode amplitude. This is how we make quantitative determinations of the mode amplitudes that are discussed in Chapter 3.

A.2.2 Determination of the profiles of flow speed and the speed of sound

As shown in the Chapter 3, during the sweep of the step, the time-dependent GP wavefunction $\Psi(x, t)$ exhibits excitation modes on top of the background condensate. To calculate the speed of sound $c(x)$ and flow speed $v(x)$, we resolve the background condensate flow by applying a WFT.

First, the amplitude of the background flow at a given time t_0 can be calculated by applying a spatial WFT on the GP density $|\Psi(x, t_0)|^2 = n(x)$, where t_0 is suppressed for brevity.

$$n(k, x) = \int_{-\infty}^{\infty} dy \, n(y) w(y - x; D) e^{-iky}. \tag{A.14}$$

Fig. A.3(a) shows the result of a spatial WFT of density $n(x)$ (which corresponds to Fig. 3.5(a)) with width $D = 5$ μm. The central streak at $k \sim 0$ corresponds to the background flow, whose peak value gives rise to the background density $n_{\rm bf}(x) = |n(k \sim 0, x)|$, as shown in Fig. A.3(b). The local speed of sound can then be expressed as by $c(x) = \sqrt{g n_{\rm bf}(x)/m}$. In Fig. A.3(b), we see that WFT works quite well in the slowly varying regions away from the two horizons: in the exterior region, $n_{\rm bf}(x)$ matches the GP density $n(x)$; in the interior region, $n_{\rm bf}(x)$ is at about the center of spatial oscillations. Near the event horizons, the background density changes rather quickly, such that WFT fails to estimate the correct local amplitude, and the resulting $n_{\rm bf}(x)$ is smoothed out nearby these regions.

Second, the flow velocity can be calculated by a WFT of the GP wavefunction

$$\Psi(k, x) = \int_{-\infty}^{\infty} dy\, \Psi(y) w(y - x; D) e^{-iky}, \tag{A.15}$$

where again t_0 is suppressed for brevity. Fig. A.3(c) shows the windowed wavevector spectrum $|\Psi(k, x)|^2$ with width $D = 5$ μm. The dominant streak is the background flow, whose peak location $k_{\rm bf}(x)$ gives rise to the flow velocity in the rest frame of the step, $-v(x) = \hbar k_{\rm bf}(x)/m - v_s$, as shown in Fig. A.3(d); the peak value of the streak also corresponds to the background density $n_{\rm bf}(x) = |\Psi(k_{\rm bf}, x)|^2$. In addition, we calculate the velocity profile by using the full GP wavefunction, $v_{\rm GP}(x) = \hbar/(mn(x))\, {\rm Im}\,[\Psi^*(x) d\Psi(x)/dx] - v_s$. We can see that WFT works well in regions apart from the event horizons, and effectively projects out the spatial oscillation present in $v_{\rm GP}(x)$.

Fig. A.3(e-f) compares $v(x)$ and $c(x)$ from the windowed spectra (panel (e))

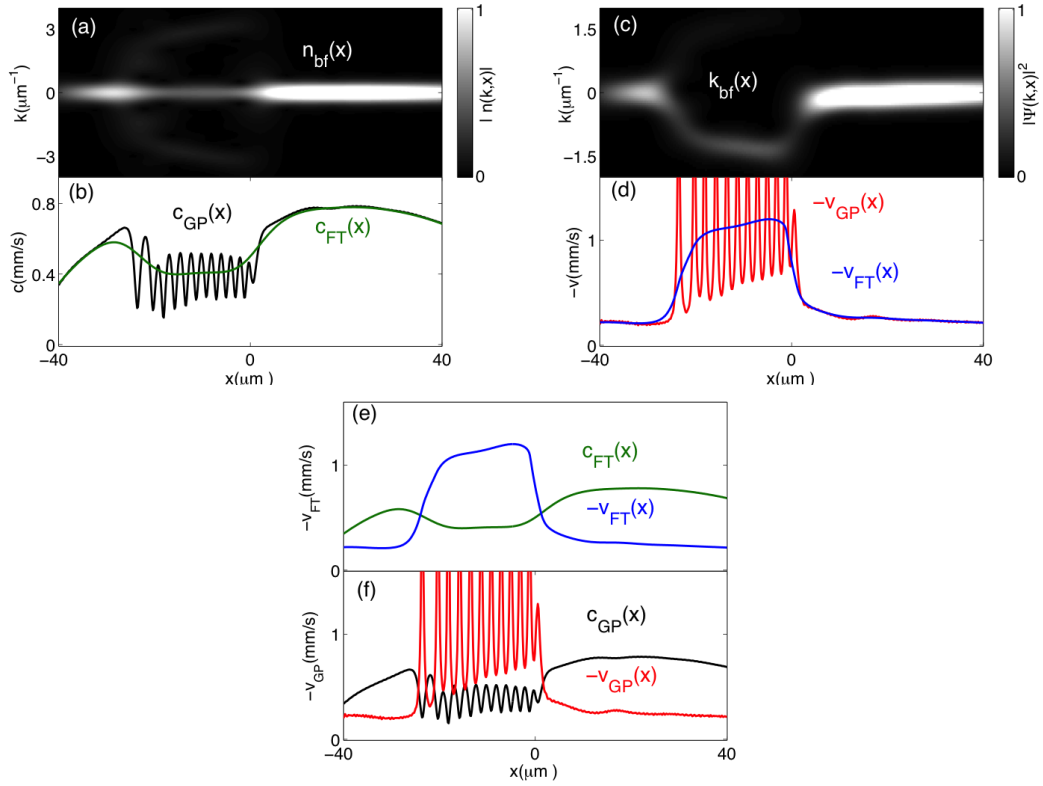

Figure A.3: Determination of flow speed $v(x)$ and the speed of sound $c(x)$. (a) windowed wavevector spectrum of density $n(x)$ at $t_0 = 80$ ms (Fig. 3.5(b)); (b) black: local speed of sound $c_{\rm GP}$ from total density $n(x)$; green: speed of sound $c_{\rm FT}$ from the background flow density $n_{\rm bf}(x)$, filtered with the Fourier spectrum; (c) windowed wavevector spectrum of GP wavefunction $\Psi(x)$; (d) red: windowed flow speed, $v_{\rm GP}$, from a direct calculation on $\Psi(x)$; blue: flow speed $v_{\rm FT}$ from the background flow wavevector $k_{\rm bf}(x)$; panels (e-f): flow structure determined by the Fourier spectra (e) and that directly obtained from the GP wavefunction (f).

with those obtained from the full GP wavefuntion (panel (f)). In short, near the event horizon, the approach of directly adopting the GP wavefunction gives more accurate speed profiles, with the correct horizon locations and the respective surface gravity; yet away from the horizons, the WFT effectively removes excitations from the background flow, and hence gives a more suitable definition for $v(x)$ and $c(x)$.

A.2.3 Spectral analysis with windowed Fourier transform

The spectral properties of excitation modes can be obtained by performing spatial and temporal WFTs on the condensate wavefunction. Given a GP wavefunction, $\Psi(x,t)$, we calculate its local wavevector spectrum and frequency spectrum by applying the WFTs. To obtain a local wavevector spectrum, we perform a spatial WFT on the wavefunction $\Psi(x,t_0)$ using Eq. A.15 at a time t_0 in which excitation modes are present. The result is presented in Fig. 3.13(a), in which the excitation modes are resolved in addition to the background flow. Note that for the region on the RHS of the step, we perform the WFTs on the variation function $\delta\Psi(x,t)$ rather than $\Psi(x,t)$, in order to subtract the background component and bring out the excitation mode in that region.

For a local frequency spectrum, we apply a temporal WFT at position $x_0(t)$ moving at constant speed v_s with the potential step:

$$\Psi(\omega,t) = \int_{-\infty}^{\infty} d\tau\, \Psi(x_0(\tau),\tau) w(\tau - t; T) e^{i\omega\tau}, \tag{A.16}$$

where $w(\tau - t; T)$ represents a Gaussian window function of width T, $w(\tau - t; T) = e^{-(\tau-t)^2/T^2}/\sqrt{\pi}T$; x_0 is selected to be both inside (x_I) and outside the BH cavity (x_O), which is indicated by the red and blue lines in Fig. 3.11(b). The result is presented in Fig. 3.13(a). In the figure, there are two modes (ψ_p and ψ_BCR) overlapped in the frequency spectrum ($\omega \sim 0.15\ \mu$m) evaluated at position $x_\mathrm{I}(t)$. To resolve the two modes, we perform a spatial WFT evaluated at $x_\mathrm{I}(t)$ for various times

$$\Psi(k,t) = \int_{-\infty}^{\infty} dy\, \Psi(y,t) w(y - x_\mathrm{I}(t); D) e^{-iky}. \tag{A.17}$$

The result is presented in Fig. A.4(a), from which $\psi_{\rm BCR}$ and $\psi_{\rm p}$ are separated at different k values, $k_{\rm BCR}$ (solid red line) and $k_{\rm p}$ (dashed red line). Furthermore, by performing a temporal WFT on $\Psi(k,t)$ at the two wavevectors, we resolve the overlapped streaks in the initial frequency spectrum at $\omega \sim 0.15$ rad/ms, as shown in Fig. A.4(b-c).

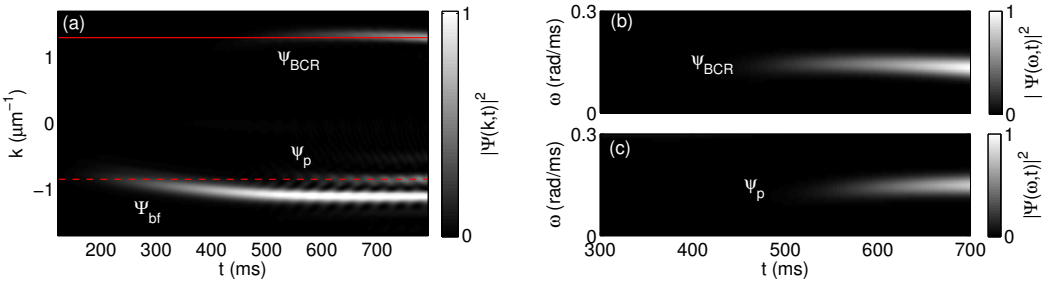

Figure A.4: Distinguishing the BCR mode ($\psi_{\rm BCR}$) and the partner mode ($\psi_{\rm p}$). (a) Local wavevector spectrum evaluated at $x_{\rm I}(t)$ for various times, in which the BdG modes ($\psi_{\rm BCR}$ and $\psi_{\rm p}$) of the same frequency are separated at different k values; (b) the frequency spectrum of $\Psi(k_{\rm BCR},t)$, where $k_{\rm BCR}$ is indicated by the solid red line in (a); (c) the frequency spectrum of $\Psi(k_{\rm p},t)$, with $k_{\rm p}$ indicated by the dashed red line in (a).

A.2.4 Windowed frequency spectrum for the experimental regime

In Chapter 3, we presented a full spectral analysis for the modified regime, which agrees with the prediction from the dispersion relations. Here we present the dispersion relation and the frequency spectrum for the experimental regime. This shows that no black hole laser effect is apparent in our simulation of the experiment of Ref. [1].

We apply the temporal WFT on $\Psi(x,t)$ at a position about the center of the cavity, $x_{\rm I} = x_{BH} - 12$ μm, indicated by the red line in Fig. 3.10(a). The resulting

frequency spectrum is given in Fig. A.5. The streak that appears from early times shows the frequency of the background flow wavefunction $\Psi_{\rm bf}$. The lower streak corresponds to the superposition of the BCR and the partner mode. The cut-through at $t = 100$ ms is shown in panel (b), from which the relative frequency (of the u-components) $\Delta\omega \sim$ -0.11(3) rad/ms.

We also predict this relative frequency using the dispersion relation. The assumption that the BCR is the zero-frequency mode in the WH frame determines $\Delta k_{\rm BCR} = 2.9\ \mu{\rm m}^{-1}$. Taking into account the velocity difference between the WH and the BH, $v_{\rm BH} - v_{\rm WH} \sim 0.032$ mm/s, the relative frequency of BCR (and p-mode) in the BH frame is given by $\Delta\omega = \pm\Delta k_{\rm BCR}(v_{\rm BH} - v_{\rm WH}) \sim \pm 0.09$ rad/ms, which is indicated by the dashed black lines in panel (c). This predicted frequency agrees with the measured value from the WFT to within the uncertainty.

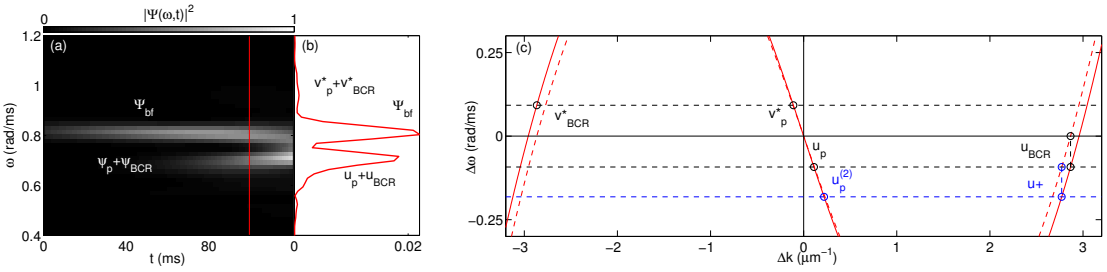

Figure A.5: Windowed frequency spectrum and dispersion relation for the experimental regime. (a) frequency spectrum evaluated at $x = x_{BH} - 12\ \mu$m. (b) cut-through along the red line in (a). (c) dispersion relations in the WH (dashed red) and BH (solid red) reference frames, evaluated at $t = 100$ ms. The dashed black lines show the frequencies of the BCR mode in the BH frame, which stimulates the first HR pair. The dashed blue line indicates the frequency of a positive-norm mode ψ_+ in the BH frame, which stimulates the second HR pair. Note that u_+ represents the u-component of ψ_+ (Eq. 5.5); $u_{\rm p}$ and $u_{\rm p}^{(2)}$ denote the u-components of the first and the second p-modes, respectively.

The wavelength of the partner mode predicted using the dispersion relation

is $\lambda_{\rm p} \sim 57$ μm, which is greater than the width of the supersonic cavity $L \sim 25$ μm. Therefore the partner cannot be treated in the WKB approximation, and the discrete spectrum of cavity modes modifies the emission, unlike in the M2 regime where the ratio $\lambda_{\rm p}/L$ is smaller. This may explain the irregular wavelength of the HR in the experimental regime seen in Fig. 3.10(a).

In addition, we find that the laser amplification will not take place in the experimental regime, where the WH recedes from the BH. When the p-mode scatters at the WH, it creates a pair of positive-norm (ψ_+) and negative-norm (ψ_-) modes [1] (here we only show the former, u_+ in panel (c)), whose frequency is the same as that of the partner in the WH frame. Due to relative velocity between BH and WH, u_+ has a shifted frequency in the BH frame (the dashed blue line in Fig. A.5(c)), lower than the frequency of the first p-mode, and it stimulates the second p-mode ($u_p^{(2)}$) at that shifted frequency. The repetitive scatterings at the horizons do not occur at a single frequency to causing lasing. Therefore, self-amplification will not occur.

A.3 BEC parameter regimes in which Hawking radiation has greater visibility

To find a more distinctive signature of HR, we study the GP evolution in different parameter regimes where the frequency of the trapping potential, ω_x, and the depth, $U_{\rm s}$, and speed, $v_{\rm s}$, of the potential step are varied away from the values (ω_x^0, $U_{\rm s}^0$, $v_{\rm s}^0$) reported in Ref. [1], which are recorded in Sec. A.1. We find that by choosing an appropriate set of experimental parameters, the HR can be observed

with well-resolved wavelengths and frequencies.

Fig. A.6 shows four representative cases for our investigation. Regimes E1 and E2 use the same trapping frequency as the experimental value ω_x^0, but adopt a greater step speed $v_s = 1.5v_s^0$; case E1 uses the step strength, $U_s/k = 6$ nK; case E2 has a greater step strength, $U_s/k = 9$ nK. Note that ω_x^0 and v_s^0 are the reference values taken from [1], $\omega_x^0 = (2\pi) \times 4.5$ Hz, and $v_s^0 = 0.21$ mm/s.

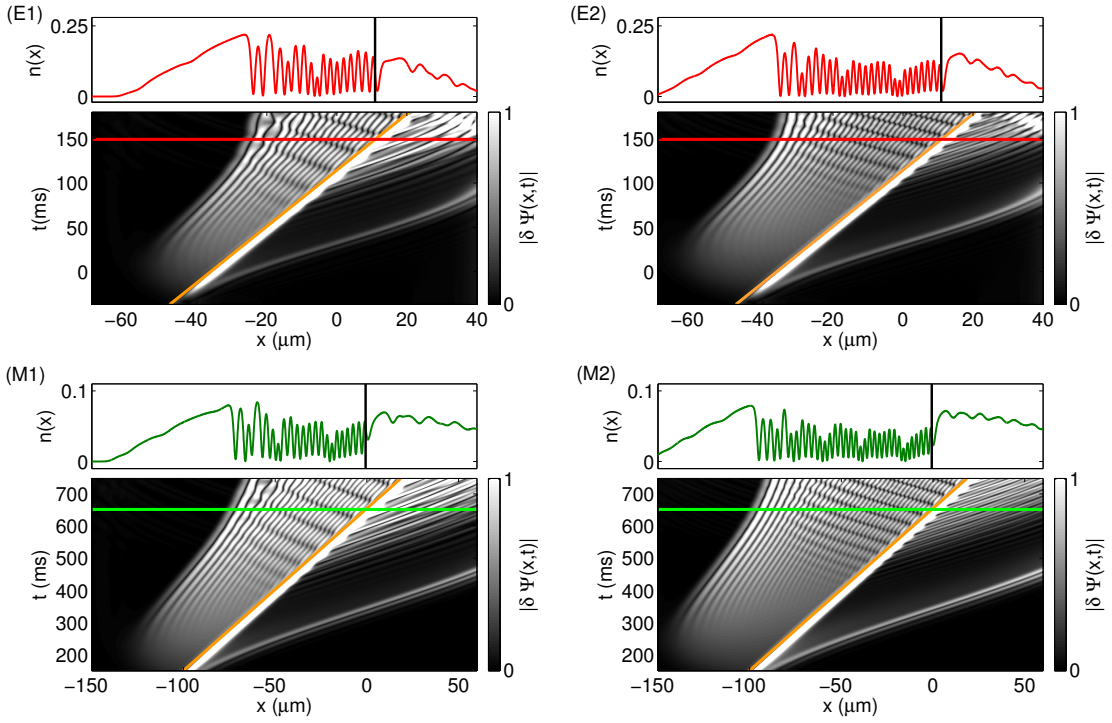

Figure A.6: Time evolution for modified parameter regimes, characterized by modified trapping frequency $\omega_x = \gamma\omega_x^0$, step speed $v_s = 1.5\gamma^{1/3}v_s^0$, and step strength U_s. Note that ω_x^0 and v_s^0 are the reference values taken from [1], $\omega_x^0 = (2\pi) \times 4.5$ Hz, and $v_s^0 = 0.21$ mm/s. Modified regimes: (E1) $\gamma = 1$, $U_s/k = 6$ nK and $v_s = 1.5v_s^0$; (E2) $\gamma = 1$, $U_s/k = 9$ nK, and $v_s = 1.5v_s^0$; (M1) $\gamma = 1/4$, $U_s/k = \gamma^{2/3} \times 6$ nK, $v_s = 1.5\gamma^{1/3}v_s^0$; (M2) $\gamma = 1/4$, $U_s/k = \gamma^{2/3} \times 9$ nK, $v_s = 1.5\gamma^{1/3}v_s^0$. Bottom: time evolution of $|\delta\Psi(x,t)|$; top: density profile $n(x)$ at times indicated by the horizontal red (green) line in the lower panel. Note that $|\delta\Psi(x,t)|$ is multiplied by 10 for $x > x_{\rm BH}$, where $x_{\rm BH}$ is indicated by the solid orange lines.

Regimes M1 and M2 are the cases equivalent to E1 and E2 with a modified

trapping frequency, $\omega_x = (1/4)\omega_x^0$. Here we use some scaling relations to determine the step speed v_s and depth U_s that give rise to an equivalent flow structure with the modified trapping frequency. We know that modifying ω_x changes the speed of sound c (due to the change of $n(x)$) and the chemical potential μ, and subsequently changes the flow structure shown in Fig. A.3. Using the Thomas-Fermi approximation [32] for a 1D condensate in a harmonic trap, we find that $\mu \propto \omega_x^{2/3}$, and the maximal density $n_\mathrm{max} \propto \omega_x^{2/3}$ (i.e. $c_\mathrm{max} \propto \omega_x^{1/3}$). By keeping ratios U_s/μ and $v_\mathrm{s}/c_\mathrm{max}$ fixed, we can construct an equivalent flow structure under a different trapping frequency. We define the scaling factor $\gamma = \omega_x/\omega_x^0$, and incorporate γ into the ratios. This gives rise to the scaling relations, $U_\mathrm{s} = \gamma^{2/3} U_\mathrm{s}^0$ and $v_\mathrm{s} = \gamma^{1/3} v_\mathrm{s}^0$. Regime M1 is the modified case for E1, such that $U_s/k = \gamma^{2/3} \times 6$ nK, $v_s = 1.5\gamma^{1/3} v_s^0$; likewise, M2 is the modified case for E2, so $U_\mathrm{s}/k = \gamma^{2/3} \times 9$ nK, $v_s = 1.5\gamma^{1/3} v_s^0$.

Our investigation shows that a clear mode structure occurs in regimes where the background flow is sufficiently homogeneous. Then the BdG modes can be described as WKB modes with well-characterized frequency and wavevector, as in Ref. [14]. In the experimental regime (Fig. 3.10(a)), ψ_p has the longest wavelength, and is comparable to the width of the BH cavity, L (the distance between the BH and WH). We find that the mode structure is improved when reducing the wavelength of the partner mode ψ_p, relative to L.

To control the wavelength of ψ_p, one can refer to the BCR mechanism and the stimulated Hawking effect, and use the dispersion relation shown in Fig. 3.12(a). Overall, the wavelength of the p-mode decreases with increasing step speed, v_s. According to the dispersion relation, the BCR is the zero frequency mode in the

WH frame, $\Delta\omega(\Delta k_{\mathrm{BCR}}) = 0$. Increasing v_s increases the flow speed inside the supersonic cavity, which lowers (raises) the positive-k (negative-k) branch of the dispersion curve $\Delta\omega(\Delta k)$, and displaces the intersection $\Delta\omega(\Delta k) = 0$ to a larger Δk value. This further increases the frequency $|\Delta\omega|$ of the Hawking pair, which is proportional to k_{BCR}, and displaces the root of the dispersion curves for ψ_{HR} and ψ_{p} to greater $|\Delta k|$ (see Fig. 3.12). In regime E1, we increase v_{s} by 50% over the experimental value. This decreases the p-mode wavelength relative to the cavity length, L, and the corresponding HR appears more periodic. We further extend L, by increasing step depth, U_s. Regime E2 in Fig. A.6 corresponds to the case with a greater step depth, in which the number of oscillations of ψ_{p} doubles.

Regimes M1 and M2 adopt a smaller trapping frequency, $\omega_x = (1/4)\omega_x^0$. Reducing ω_x increases the size of a BEC, and extends the flow structure, by which excitation modes can be more easily observed and resolved in the laboratory. We can see that cases M1 and M2 have clear mode structures as in E1 and E2, with approximately twice the cavity length. Note that regime M2 is reported in Chapter 3, along with a mode analysis using the spatial and temporal WFTs.

Appendix B: Numerical procedures for Chapter 4

B.1 GP simulation and optimizing experimental parameters

The GP simulation in Chapter 4 is similar to that in Chapter 3. In Chapter 4, we further modify the parameters for the trapping and the step potentials, to better model the experiment. Here we provide the details of such modification.

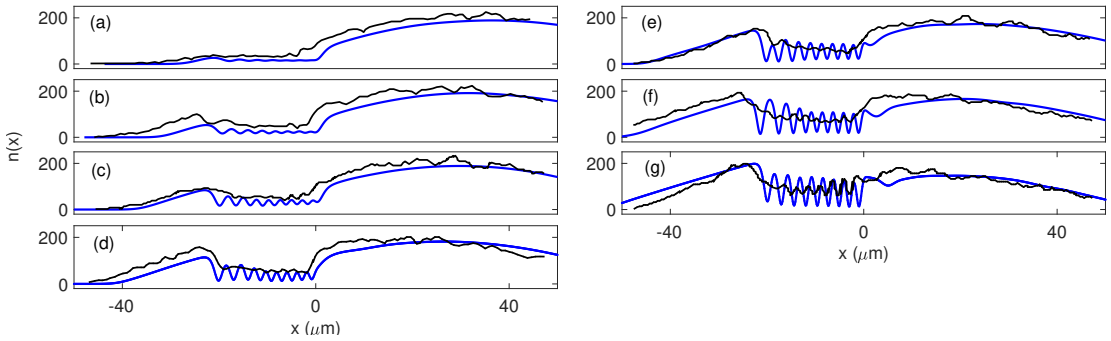

Figure B.1: The evolution of a condensate. The density profile is plotted at 20 ms intervals with moving potential step $U_s = 0.75\mu$, scaled by a common factor to match experiment, and viewed in the moving frame where $x = 0$ defines the step edge. Black: experiment [1]; blue: present simulation.

First, for the trapping potential $U_{1D}(x)$, we use the Gaussian-beam potential (A.3) evaluated at $\rho = 0$, i.e. $U_{1D}(x) = U_0 x^2/(x^2 + x_0^2)$. We adjust the parameter U_0 from the estimate in Eq. A.5, to optimize the consistency of the simulation with the experimental observations [1]. Using this potential and 1DGPE, we simulate the step-sweeping experiment [1, 34]. We introduce a step potential $U_{\text{step}}(x, t)$, which

takes the form

$$U_{\rm step}(x,t) = -U_{\rm s}(\tanh((x_{\rm s}(t)-x)/D_s)-1)/2. \tag{B.1}$$

Here $U_{\rm s}$ is the step strength, $U_s = 0.75\mu$, with μ the chemical potential, $x_{\rm s}(t)$ is the step position, moving at speed, $v_s = 0.21$ mm/s, and $D_{\rm s}$ is the step width, $D_{\rm s} = 0.5\mu$m.

Figure B.1 shows the evolution of the condensate density profile with $U_0 = 33.2\,k$ nK. The single evolution of the 1D condensate agrees qualitatively well with the average density measured in the experiment, regarding the shape of the background condensate, the cavity size, and the wavelength and phase of the standing wave near the BH. As discussed in the text, the addition of atom number fluctuations to the simulated ensemble suppresses the oscillation amplitude on the left half of the cavity, and so improves the agreement.

We noticed that certain features of the condensate evolution can be very sensitive to parameters in the potential. To illustrate this here, we vary the trap coefficient slightly, by 3%, $U_0' = (1 \pm 0.03)U_0$, which is illustrated in Fig. B.2(a). The resulting density profiles at $t = 120$ ms are shown in Fig. B.2(b). The cavity size in the density profiles is similar, however there is a change in the standing wave patterns, and the density to the right of the cavity (where the Hawking radiation is emitted), as shown in Fig. B.2(b). We also found that this phase shift modifies the checkerboard pattern in the correlation functions. The checkerboard is present in all cases, but the variation $\delta n(x)$ is more sensitive to the change of atom number with a lower trap. This produces stronger features of the lines parallel to the

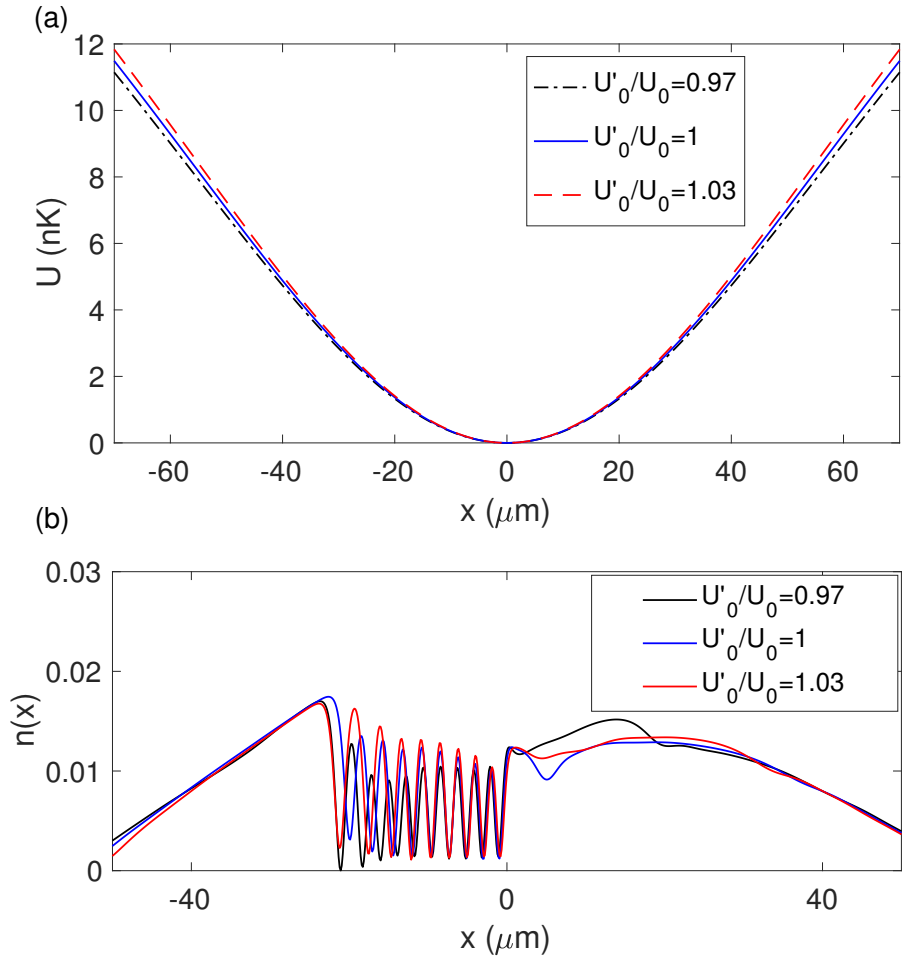

Figure B.2: Simulations with various trap coefficients, $U_0' = (1 \pm 0.03)U_0$. Panel (a): effective axial potential, $U_{1D}(x)$. Solid blue: $U_0'/U_0 = 1$; dashed-dotted black: $U_0'/U_0 = 0.97$; dashed red $U_0'/U_0 = 1.03$. Note that the minimum of $U(x)$ is shifted to zero. Panel (b): density profiles using the corrected potentials with parameter $U_0'/U_0 = 0.97$, 1, 1.03.

diagonal near the WH, and the dark nodal lines near the BH in the checkerboard. We conjecture that this hypersensitivity to the potential strength is related to the Čerenkov instability that produces the standing wave, since small differences in the condensate and flow early in the evolution may be amplified by the onset of the instability.

Bibliography

[1] Jeff Steinhauer. Observation of self-amplifying Hawking radiation in an analogue black-hole laser. *Nature Physics*, 10(11):864–869, 2014.

[2] Jeff Steinhauer and Juan Ramón Muñoz de Nova. Self-amplifying Hawking radiation and its background: A numerical study. *Phys. Rev. A*, 95:033604, Mar 2017.

[3] A. Einstein. Quantentheorie des einatomigen idealen gases. *Sitzungsbericht der Preussischein Akademie der Wissenschaften*, page 3, 1925.

[4] MH Anderson, JR Ensher, MR Matthews, CE Wieman, and EA Cornell. Observation of Bose-Einstein condensation in a dilute atomic vapor. *Science*, 75:198, 1995.

[5] K. B. Davis, M. O. Mewes, M. R. Andrews, N. J. van Druten, D. S. Durfee, D. M. Kurn, and W. Ketterle. Bose-Einstein condensation in a gas of sodium atoms. *Phys. Rev. Lett.*, 75:3969–3973, Nov 1995.

[6] C. C. Bradley, C. A. Sackett, J. J. Tollett, and R. G. Hulet. Evidence of Bose-Einstein condensation in an atomic gas with attractive interactions. *Phys. Rev. Lett.*, 75:1687–1690, Aug 1995.

[7] William D. Phillips. Nobel lecture: Laser cooling and trapping of neutral atoms. *Rev. Mod. Phys.*, 70:721–741, Jul 1998.

[8] Wolfgang Ketterle and N.J. Van Druten. Evaporative cooling of trapped atoms. volume 37 of *Advances In Atomic, Molecular, and Optical Physics*, pages 181 – 236. Academic Press, 1996.

[9] Franco Dalfovo, Stefano Giorgini, Lev P. Pitaevskii, and Sandro Stringari. Theory of Bose-Einstein condensation in trapped gases. *Rev. Mod. Phys.*, 71:463–512, Apr 1999.

[10] Immanuel Bloch, Jean Dalibard, and Wilhelm Zwerger. Many-body physics with ultracold gases. *Rev. Mod. Phys.*, 80:885–964, Jul 2008.

[11] E. P. Gross. Structure of a quantized vortex in boson systems. *Nuovo Cimiento*, 20:454, 1961.

[12] L. P. Pitaevskii. Vortex lines in an Imperfect Bose gas. *Sov. Phys. JETP*, 13:451, 1961.

[13] N. N. Bogoliubov. On the theory of superfluidity. *J. Phys. (USSR)*, 11:23, 1947.

[14] S Finazzi and R Parentani. Black hole lasers in Bose-Einstein condensates. *New J. Phys.*, 12(9):095015, 2010.

[15] L. J. Garay, J. R. Anglin, J. I. Cirac, and P. Zoller. Sonic analog of gravitational black holes in Bose-Einstein condensates. *Phys. Rev. Lett.*, 85:4643–4647, Nov 2000.

[16] W. G. Unruh. Experimental black-hole evaporation? *Phys. Rev. Lett.*, 46:1351–1353, May 1981.

[17] Oren Lahav, Amir Itah, Alex Blumkin, Carmit Gordon, Shahar Rinott, Alona Zayats, and Jeff Steinhauer. Realization of a sonic black hole analog in a Bose-Einstein condensate. *Phys. Rev. Lett.*, 105:240401, Dec 2010.

[18] Jeff Steinhauer. Observation of quantum Hawking radiation and its entanglement in an analogue black hole. *Nature Physics*, 12(10):959–965, 2016.

[19] Steven Corley and Ted Jacobson. Black hole lasers. *Phys. Rev. D*, 59:124011, May 1999.

[20] Alice Sinatra, Carlos Lobo, and Yvan Castin. The truncated Wigner method for Bose-condensed gases: limits of validity and applications. *Journal of Physics B: Atomic, Molecular and Optical Physics*, 35(17):3599, 2002.

[21] A. Ramanathan, K. C. Wright, S. R. Muniz, M. Zelan, W. T. Hill, C. J. Lobb, K. Helmerson, W. D. Phillips, and G. K. Campbell. Superflow in a Toroidal Bose-Einstein condensate: an atom circuit with a tunable weak link. *Phys. Rev. Lett.*, 106(13):130401, March 2011.

[22] K. Wright, R. Blakestad, C. Lobb, W. Phillips, and G. Campbell. Driving phase slips in a superfluid atom circuit with a rotating weak link. *Phys. Rev. Lett.*, 110(2):25302, January 2013.

[23] L. J. Garay, J. R. Anglin, J. I. Cirac, and P. Zoller. Sonic black holes in dilute Bose-Einstein condensates. *Phys. Rev. A*, 63:023611, Jan 2001.

[24] P. Jain, A. S. Bradley, and C. W. Gardiner. Quantum de Laval nozzle: Stability and quantum dynamics of sonic horizons in a toroidally trapped Bose gas containing a superflow. *Phys. Rev. A*, 76:023617, Aug 2007.

[25] Arthur Rich. Recent experimental advances in positronium research. *Rev. Mod. Phys.*, 53:127–165, Jan 1981.

[26] P. M. Platzman and A. P. Mills. Possibilities for Bose condensation of positronium. *Phys. Rev. B*, 49:454–458, Jan 1994.

[27] A. P. Mills, D. B. Cassidy, and R. G. Greeves. *Materials Science Forum*, 445-446:424, 2004.

[28] D. B. Cassidy, V. E. Meligne, and A. P. Mills. Production of a fully spin-polarized ensemble of positronium atoms. *Phys. Rev. Lett.*, 104:173401, Apr 2010.

[29] D. B. Cassidy, S. H. M. Deng, and A. P. Mills. Evidence for positronium molecule formation at a metal surface. *Phys. Rev. A*, 76:062511, Dec 2007.

[30] D. B. Cassidy and A. P. Mills. Interactions between positronium atoms in porous silica. *Phys. Rev. Lett.*, 100:013401, Jan 2008.

[31] Allen Paine Mills. Positronium molecule formation, Bose–Einstein condensation and stimulated annihilation. *Nuclear Instruments and Methods in Physics Research Section B: Beam Interactions with Materials and Atoms*, 192(1–2):107 – 116, 2002.

[32] C.J. Pethick and H. Smith. *Bose-Einstein condensation in dilute gases*. Cambridge University Press, second edition, 2008.

[33] Scott J Robertson. The theory of Hawking radiation in laboratory analogues. *J. Phys. B: At. Mol. Opt. Phys.*, 45(16):163001, 2012.

[34] Yi-Hsieh Wang, Ted Jacobson, M. Edwards, and C. W. Clark. Mechanism of stimulated Hawking radiation in a laboratory Bose-Einstein condensate. arXiv:1605.01027, 2016.

[35] Carlos Mayoral, Alessio Recati, Alessandro Fabbri, Renaud Parentani, Roberto Balbinot, and Iacopo Carusotto. Acoustic white holes in flowing atomic BoseEinstein condensates. *New J. Phys.*, 13(2):025007, 2011.

[36] I. Carusotto, S. X. Hu, L. A. Collins, and A. Smerzi. Bogoliubov-Čerenkov Radiation in a Bose-Einstein condensate flowing against an obstacle. *Phys. Rev. Lett.*, 97:260403, Dec 2006.

[37] Jean Macher and Renaud Parentani. Black-hole radiation in Bose-Einstein condensates. *Phys. Rev. A*, 80:043601, Oct 2009.

[38] Jonas Gomes and Luiz Velho. *From Fourier Analysis to Wavelets*. Springer, 2015.

[39] P. Leboeuf and N. Pavloff. Bose-Einstein beams: coherent propagation through a guide. , 64(3):033602, September 2001.

[40] Iacopo Carusotto and Germain Rousseaux. The Cerenkov effect revisited: From swimming ducks to zero modes in gravitational analogs. *Lect. Notes Phys.*, 870:109–144, 2013.

[41] W. G. Unruh. Sonic analog of black holes and the effects of high frequencies on black hole evaporation. *Phys. Rev. D*, 51:2827–2838, 1995.

[42] W. G. Unruh. Has Hawking radiation been measured? *Found. Phys.*, 44:532–545, 2014.

[43] L. Isella and J. Ruostekoski. Quantum dynamics in splitting a harmonically trapped Bose-Einstein condensate by an optical lattice: Truncated Wigner approximation. *Phys. Rev. A*, 74:063625, Dec 2006.

[44] Sebastian Wuster, Beata J. Dabrowska-Wuster, Ashton S. Bradley, Matthew J. Davis, P. Blair Blakie, Joseph J. Hope, and Craig M. Savage. Quantum depletion of collapsing Bose-Einstein condensates. *Phys. Rev. A*, 75:043611, Apr 2007.

[45] J. Ruostekoski and A. D. Martin. Truncated Wigner method for Bose gases. arXiv:1009.1073, 2012.

[46] Tettamanti, M., Cacciatori, S. L., Parola, A., and Carusotto, I. Numerical study of a recent black-hole lasing experiment. *EPL*, 114(6):60011, 2016.

[47] M. Gajdacz, A. J. Hilliard, M. A. Kristensen, P. L. Pedersen, C. Klempt, J. J. Arlt, and J. F. Sherson. Preparation of ultracold atom clouds at the shot noise level. *Phys. Rev. Lett.*, 117:073604, Aug 2016.

[48] Yi-Hsieh Wang, A Kumar, F Jendrzejewski, Ryan M Wilson, Mark Edwards, S Eckel, G K Campbell, and Charles W Clark. Resonant wavepackets and shock waves in an atomtronic SQUID. *New Journal of Physics*, 17(12):125012, 2015.

[49] Augusto Smerzi and Stefano Fantoni. Large amplitude oscillations of a Bose condensate. *Phys. Rev. Lett.*, 78:3589–3593, May 1997.

[50] S. Choi, S. Morgan, and K. Burnett. Phenomenological damping in trapped atomic Bose-Einstein condensates. *Phys. Rev. A*, 57(5):4057–4060, May 1998.

[51] S. A. Morgan, S. Choi, K. Burnett, and M. Edwards. Nonlinear mixing of quasiparticles in an inhomogeneous Bose condensate. *Phys. Rev. A*, 57:3818–3829, May 1998.

[52] N Proukakis, S Gardiner, M Davis, and M Szymanska. *Quantum Gases: Finite Temperatures and Non-equilibrium Dynamics*. Cold atoms. Imperial College Press, 2013.

[53] J. J. Chang, P. Engels, and M. A. Hoefer. Formation of dispersive shock waves by merging and splitting Bose-Einstein condensates. *Phys. Rev. Lett.*, 101:170404, Oct 2008.

[54] R. Meppelink, S. B. Koller, J. M. Vogels, P. van der Straten, E. D. van Ooijen, N. R. Heckenberg, H. Rubinsztein-Dunlop, S. A. Haine, and M. J. Davis. Observation of shock waves in a large Bose-Einstein condensate. *Phys. Rev. A*, 80:043606, Oct 2009.

[55] M. R. Andrews, C. G. Townsend, H.-J. Miesner, D. S. Durfree, D. M. Kurn, and W. Ketterle. Observation of interference between two Bose condensates. *Science*, 275(5300):637, January 1997.

[56] P. G. Kevrekidis, D. J. Frantzeskakis, and R. Carretero-Gonzalez. *The defocusing nonlinear Schrödinger equation : from dark solitons to vortices and vortex rings*. Society for Industrial and Applied Mathematics, 2015.

[57] H. Wiedemann. *Particle Accelerator Physics (Graduate Texts in Physics) 4th ed.* Springer, 2015.

[58] S. Eckel, F. Jendrzejewski, A. Kumar, C. J. Lobb, and G. K. Campbell. Interferometric Measurement of the Current-Phase Relationship of a Superfluid Weak Link. *Phys. Rev. X*, 4(3):031052, September 2014.

[59] Jeffrey G. Lee and W. T. Hill. Spatial shaping for generating arbitrary optical dipole traps for ultracold degenerate gases. *Rev. Sci. Instrum.*, 85(10):–, 2014.

[60] Anand Ramanathan, Sérgio R Muniz, Kevin C Wright, Russell P Anderson, William D Phillips, Kristian Helmerson, and Gretchen K Campbell. Partial-transfer absorption imaging: a versatile technique for optimal imaging of ultracold gases. *Rev. Sci. Instrum.*, 83(8):083119, August 2012.

[61] S. Stringari and L. Pitaevskii. *Bose-Einstein condensation*. Oxford University Press, 2003.

[62] E. Zaremba. Sound propagation in a cylindrical Bose-condensed gas. *Phys. Rev. A*, 57:518–521, Jan 1998.

[63] R. Dubessy, T. Liennard, P. Pedri, and H. Perrin. Critical rotation of an annular superfluid Bose-Einstein condensate. *Phys. Rev. A*, 86:011602, Jul 2012.

[64] C. W. Clark. The calculation of non-adiabatic transition probabilities. *Physics Letters A*, 70:295–296, March 1979.

[65] P. Muruganandam and S.K. Adhikari. Fortran programs for the time-dependent grosspitaevskii equation in a fully anisotropic trap. *Comput. Phys. Commun.*, 180(10):1888 – 1912, 2009.

[66] Stephen Eckel, Jeffrey G. Lee, Fred Jendrzejewski, Noel Murray, Charles W. Clark, Christopher J. Lobb, William D. Phillips, Mark Edwards, and Gretchen K. Campbell. Hysteresis in a quantized superfluid atomtronic circuit. *Nature*, 506(7487):200–203, February 2014.

[67] R. Kosloff and D. Kosloff. Absorbing boundaries for wave propagation problems. *J. Comput. Phys.*, 63(2):363 – 376, 1986.

[68] M. Zak and I. Kulikov. Supersonic effects and shock waves in a Bose-Einstein condensate. *Phys. Lett. A*, 307:99–106, January 2003.

[69] Igor Kulikov and Michail Zak. Shock waves in a bose-einstein condensate. *Phys. Rev. A*, 67:063605, Jun 2003.

[70] Bogdan Damski. Formation of shock waves in a Bose-Einstein condensate. *Phys. Rev. A*, 69:043610, Apr 2004.

[71] Yu. G. Gladush, G. A. El, A. Gammal, and A. M. Kamchatnov. Radiation of linear waves in the stationary flow of a Bose-Einstein condensate past an obstacle. *Phys. Rev. A*, 75:033619, Mar 2007.

[72] A. M. Kamchatnov and L. P. Pitaevskii. Stabilization of solitons generated by a supersonic flow of Bose-Einstein condensate past an obstacle. *Phys. Rev. Lett.*, 100:160402, Apr 2008.

[73] Fabrice Béthuel, Philippe Gravejat, and Jean-Claude Saut. Travelling Waves for the Gross-Pitaevskii Equation II. *Commun. Math. Phys.*, 285(2):567–651, January 2009.

[74] D. J. Frantzeskakis. Dark solitons in atomic BoseEinstein condensates: from theory to experiments. *J. Phys. A Math. Theor.*, 43(21):213001, May 2010.

[75] A. M. Kamchatnov and N. Pavloff. Generation of dispersive shock waves by the flow of a Bose-Einstein condensate past a narrow obstacle. *Phys. Rev. A*, 85:033603, Mar 2012.

[76] Charles J. M. Mathy, Mikhail B. Zvonarev, and Eugene Demler. Quantum flutter of supersonic particles in one-dimensional quantum liquids. *Nat. Phys.*, 8(12):881–886, October 2012.

[77] I. Zapata, M. Albert, R. Parentani, and F. Sols. Resonant Hawking radiation in BoseEinstein condensates. *New J. Phys.*, 13(6):063048, June 2011.

[78] Florent Michel and Renaud Parentani. Nonlinear effects in time-dependent transonic flows: An analysis of analog black hole stability. *Phys. Rev. A*, 91:053603, May 2015.

[79] S. Burger, K. Bongs, S. Dettmer, W. Ertmer, K. Sengstock, A. Sanpera, G. V. Shlyapnikov, and M. Lewenstein. Dark solitons in Bose-Einstein condensates. *Phys. Rev. Lett.*, 83:5198–5201, Dec 1999.

[80] J. Denschlag, J. E. Simsarian, D. L. Feder, C. W. Clark, L. A. Collins, J. Cubizolles, L. Deng, E. W. Hagley, K. Helmerson, W. P. Reinhardt, S. L. Rolston, B. I. Schneider, and W. D. Phillips. Generating solitons by phase engineering of a Bose-Einstein condensate. *Science*, 287:97–101, January 2000.

[81] Z Dutton, M Budde, C Slowe, and L V Hau. Observation of quantum shock waves created with ultra- compressed slow light pulses in a Bose-Einstein condensate. *Science*, 293(5530):663–8, July 2001.

[82] Yi-Hsieh Wang, Brandon M. Anderson, and Charles W. Clark. Spinor Bose-Einstein condensates of positronium. *Phys. Rev. A*, 89:043624, Apr 2014.

[83] M. Charlton and J. W. Humberston. *Positron Physics*, volume 1. Cambridge, second edition, 2000.

[84] D. B. Cassidy, S. H. M. Deng, R. G. Greaves, T. Maruo, N. Nishiyama, J. B. Snyder, H. K. M. Tanaka, and A. P. Mills. Experiments with a high-density positronium gas. *Phys. Rev. Lett.*, 95:195006, Nov 2005.

[85] B.R. Judd. *Angular momentum theory for diatomic molecules*. Academic Press, 1975.

[86] D. M. Schrader. Symmetry of dipositronium Ps_2. *Phys. Rev. Lett.*, 92:043401, Jan 2004.

[87] I. A. Ivanov, J. Mitroy, and K. Varga. Elastic positronium-atom scattering using the stochastic variational method. *Phys. Rev. Lett.*, 87:063201, Jul 2001.

[88] I. A. Ivanov, J. Mitroy, and K. Varga. Positronium-positronium scattering using the stochastic variational method. *Phys. Rev. A*, 65:022704, Jan 2002.

[89] Tin-Lun Ho. Spinor Bose condensates in optical traps. *Phys. Rev. Lett.*, 81:742–745, Jul 1998.

[90] Tetsuo Ohmi and Kazushige Machida. Bose-Einstein condensation with internal degrees of freedom in alkali atom gases. *J. Phys. Soc. Jpn.*, 67:1822–1825, 1998.

[91] Dan M. Stamper-Kurn and Masahito Ueda. Spinor Bose gases: Symmetries, magnetism, and quantum dynamics. *Rev. Mod. Phys.*, 85:1191–1244, Jul 2013.

[92] Yuki Kawaguchi and Masahito Ueda. Spinor Bose–Einstein condensates. *Physics Reports*, 520(5):253 – 381, 2012.

[93] H. Pu, C. K. Law, S. Raghavan, J. H. Eberly, and N. P. Bigelow. Spin-mixing dynamics of a spinor Bose-Einstein condensate. *Phys. Rev. A*, 60:1463–1470, Aug 1999.

[94] S. Raghavan, A. Smerzi, S. Fantoni, and S. R. Shenoy. Coherent oscillations between two weakly coupled Bose-Einstein condensates: Josephson effects, π oscillations, and macroscopic quantum self-trapping. *Phys. Rev. A*, 59:620–633, Jan 1999.

[95] Wenxian Zhang, D. L. Zhou, M.-S. Chang, M. S. Chapman, and L. You. Coherent spin mixing dynamics in a spin-1 atomic condensate. *Phys. Rev. A*, 72:013602, Jul 2005.

[96] Harris Hancock. *Elliptic Integrals*, volume 1. Dover, first edition, 1958.

[97] NIST Digital Library of Mathematical Functions. http://dlmf.nist.gov/, Release 1.0.6 of 2013-05-06. Online companion to [98].

[98] F. W. J. Olver, D. W. Lozier, R. F. Boisvert, and C. W. Clark, editors. *NIST Handbook of Mathematical Functions*. Cambridge University Press, New York, NY, 2010. Print companion to [97].

[99] D. J. Heinzen, Roahn Wynar, P. D. Drummond, and K. V. Kheruntsyan. Superchemistry: dynamics of coupled atomic and molecular Bose-Einstein condensates. *Phys. Rev. Lett.*, 84:5029–5033, May 2000.

[100] Edison P. Liang and Charles D. Dermer. Laser cooling of positronium. *Optics Communications*, 65(6):419 – 424, 1988.

[101] Peter J. Mohr, Barry N. Taylor, and David B. Newell. Codata recommended values of the fundamental physical constants: 2010. *Rev. Mod. Phys.*, 84:1527–1605, Nov 2012.

[102] L. Salasnich, A. Parola, and L. Reatto. Effective wave equations for the dynamics of cigar-shaped and disk-shaped Bose condensates. *Phys. Rev. A*, 65:043614, Apr 2002.

[103] P. Muruganandam and S.K. Adhikari. Fortran programs for the time-dependent grosspitaevskii equation in a fully anisotropic trap. *Computer Physics Communications*, 180(10):1888 – 1912, 2009.